

Measurement of $W^\pm Z$ Production in Proton-Proton Collisions
at $\sqrt{s} = 7$ TeV with the ATLAS Detector

Kohei Kessoku

A dissertation submitted to the Department of Physics
for the degree of Doctor of Philosophy

The University of Tokyo

December 2012

Abstract

The ATLAS (A Toroidal Lhc ApparatuS) experiment at the Large Hadron Collider (LHC) explores the frontiers of particle physics. The experiment needs to control huge backgrounds to perform the entire physics programs. The muon trigger system of ATLAS filters events containing high transverse momentum (p_T) muons and is one of the key components to conduct the challenging task. This study utilizes the full performance of the muon trigger system.

The $W^\pm Z$ process is one of interesting Standard Model processes because the process has not been tested at sufficient level at the past experiments. Furthermore anomalous Triple Gauge Couplings beyond the Standard Model could be observed in the production. The $W^\pm Z \rightarrow \ell \nu \ell' \ell'$ channel can be identified with less backgrounds compared to the other processes because of the three high p_T leptons coming from W and Z bosons. However, there are still significant backgrounds in the LHC environment. The event and object selections to reduce those backgrounds have been optimized. The isolation requirement for leptons is expected to largely reduce the backgrounds and the effect of this requirement on the analysis has been investigated. Finally the $W^\pm Z$ production cross section at $\sqrt{s} = 7$ TeV is measured to be $19.0^{+1.4}_{-1.3}$ (stat.) ± 0.9 (syst.) ± 0.4 (lumi.) pb with 4.6 fb^{-1} data. This result is consistent with the Standard Model prediction within the uncertainties. The limit on anomalous Triple Gauge Coupling is also determined.

Both results are consistent with the Standard Model prediction. The dominant uncertainty is statistics. Therefore further test with data with higher statistics is desirable. This study has confirmed that a precise measurement of anomalous TGC in the WZ process is a good probe to the search for physics beyond the Standard Model.

Contents

1	Introduction	2
1.1	The Unification of Electroweak Interaction	4
1.1.1	$U(1)$ Gauge Symmetry (The Quantum Electrodynamics)	4
1.1.2	The Grashow-Weinberg-Salam (GWS) Theory	5
1.1.3	Decay of the Weak Bosons	10
1.1.4	Self-coupling of Bosons in the Electroweak Interaction	12
1.1.5	Anomalous Triple Gauge Coupling (aTGC)	15
1.1.6	Expected Cross-section of the $W^\pm Z$ Production in Proton-Proton Collisions at 7 TeV	16
1.2	The Motivation and Significance of This Study	18
1.3	Major Contributions	19
2	Experimental Conditions	20
2.1	The Large Hadron Collider	20
2.2	The ATLAS Experiment	24
2.3	The ATLAS Detector	24
2.3.1	Coordinate System of the ATLAS	24
2.3.2	Overview of the ATLAS Detector	24
2.3.3	Inner Detector	26
2.3.4	Calorimeter	29
2.3.5	Muon Spectrometer	37
2.3.6	Magnets	43
2.4	Trigger and Data Acquisition	46
2.4.1	Trigger	48
2.4.2	DAQ	54
2.5	Reconstruction Scheme	55
2.5.1	Vertex Reconstruction	56
2.5.2	Muons	56
2.5.3	Electrons	59
2.5.4	Missing Energy	60
3	The Datasets and Event Selection	65
3.1	Datasets	65
3.1.1	Luminosity Measurement for the ATLAS	65

3.1.2	Data	67
3.1.3	Monte Carlo Simulation	70
3.2	Event Selection	72
3.2.1	Event Selection Criteria	72
3.2.2	Object Selection Optimization	83
3.3	Background Estimation	96
3.3.1	ZZ	96
3.3.2	$Z+\gamma$	96
3.3.3	$t\bar{t}$	96
3.3.4	Z +jets	98
3.4	Systematic Uncertainty	101
3.5	Summary	105
3.5.1	Comparison of Final Numbers of Observed and Expected Events	113
4	Cross Section Measurement	115
4.1	Cross Section Extraction	115
5	Triple Gauge Coupling Measurement	118
5.1	Extraction Procedure	118
5.1.1	Reweighting the aTGC Parameters	119
5.2	Observable Selection	120
5.3	Binning Selection	122
5.4	Result	125
6	Discussion	126
6.1	Comparison of the Cross Section Measurement with Other Experiments	126
6.2	Comparison of the Limit on the anomalous TGC with Other Experiments	126
7	Conclusion	128

List of Figures

1.1	Quarks, leptons and force carriers in the SM.	3
1.2	Tree level Feynmann diagram of the $W \rightarrow f\bar{f}'$ vertex.	11
1.3	Tree level Feynmann diagram of the $Z \rightarrow f\bar{f}$ vertex.	11
1.4	Diagrams of the process $e^+e^- \rightarrow W^+W^-$ at tree level.	13
1.5	WWV vertex. $V = Z, \gamma$	14
1.6	Production cross-section of W^+W^- in e^+e^- collisions measured at LEP is shown as a function of the center of mass energy, $E_{\text{cm}} = \sqrt{s}$ [1].	15
1.7	Diagrams of WZ production in hadron collisions.	15
1.8	Parton distribution functions of CT10 [2].	17
1.9	Limits on aTGC by the CDF and D0 experiments [3], [4].	18
2.1	The overview of the Large Hadron Collier [5]. Protons for the beams are obtained from hydrogen atoms. They are injected from the linear accelerator (LINAC2) into the PS Booster, then the Proton Synchrotron (PS), followed by the Super Proton Synchrotron (SPS), and finally the beams reach the LHC ring.	21
2.2	Cross section of the LHC two-in-one dipole magnet [6].	22
2.3	Coordinate System. The beam direction defines the z-axis and the x-y plane is transverse to the beam direction. The positive x-axis is defined as pointing from the interaction point to the center of the LHC ring and the positive y-axis is defined as pointing upwards. The detector can be distinguished into two sides, as the plane where z is zero is the boarder plane. The side of positive z is defined as the side-A and the one of negative z is defined as the side-C.	25
2.4	Cut-away view of the ATLAS detector [7].	25
2.5	A cut-away view of the Inner detector (ID) [7].	26
2.6	A detailed configuration of the ATLAS Inner Detectors [8].	27
2.7	Material distribution in the inner detector as a function of $ \eta $ [8].	28
2.8	A cutaway view of the ATLAS Calorimeters [7].	29
2.9	The layout of the calorimeters in the endcap and forward region. All the calorimeters are housed in the same cryostat [9].	30
2.10	Sketch of a barrel LAr Calorimeter module [9].	31
2.11	A schematic view of a scintillator tile calorimeter module [9].	32

2.12	Cumulative amounts of material in units of X_0 (radiation length) and as a function of $ \eta $ in front of and in the EM calorimeters. (a) The total amount of material in front of the presampler layer and in front of the first layer of the EM calorimeters over the full η range. (b) The thickness of each layer as well as the material in front of the first layer in the barrel. (c) The thickness of each layer as well as the material in front of the first layer in the endcap [9].	34
2.13	Cumulative amount of material in units of λ (interaction length) as a function of $ \eta $ in front of and in the EM calorimeters, in each hadronic layer, the total amount at the end of the active calorimetry and the total amount of material in front of the first active layer of the muon spectrometer [9].	35
2.14	A schematic R-z view of the ATLAS muon spectrometer [10].	38
2.15	A schematic R- ϕ view of the ATLAS muon spectrometer [11].	38
2.16	η - ϕ map of the coverage of the ten detector regions [12].	39
2.17	A drift tube of the MDT [13].	39
2.18	A schematic view of a barrel MDT chamber [13].	40
2.19	A schematic view of an end-cap MDT chamber with the optical alignment system [11].	41
2.20	A calculated typical momentum resolution for muons reconstructed in the muon spectrometer. The alignment curve is for an uncertainty of $30\ \mu\text{m}$ in the chamber positions. (a) is for $ \eta < 1.5$ and (b) is for $ \eta > 1.5$ [11].	41
2.21	(a) The CSCs mounted on a rigid wheel inclined by 11.59° [11]. (b) A cutout view of a CSC chamber [13].	42
2.22	The cross section of an RPC chamber [11].	43
2.23	(a) A schematic illustration of a TGC chamber. (b) TGC structure showing anode wires, graphite cathodes, G-10 layers, and a read-out strip orthogonal to the wire [11].	44
2.24	A cutaway view of the ATLAS superconducting magnetic system. The eight barrel toroid coils with the end-cap coils interleaved are visible. The solenoid winding lies inside the calorimeter volume. The tile calorimeter is modeled by four layers with different magnetic properties plus an outside return yoke [14].	45
2.25	Magnetic field for the solenoid and bending power for the toroid magnet [14]. .	46
2.26	Schematic views of the ATLAS TDAQ system [15].	47
2.27	Block diagram of the L1 trigger [15].	49
2.28	Schematic of the muon trigger system. The second station of the RPC (RPC2) and the outermost station of the TGC (TGC3) are the reference planes for barrel and end-cap, respectively [11].	50
2.29	Tag-and-Probe method. The method uses two reconstructed muons whose invariant mass is close to the Z or J/ψ mass (In the Z boson case, it is $ M_{\text{inv}} - M_{\text{PDG}} < 10\text{GeV}$). After requiring the mass selection, one of the two muons has to be matched with a trigger object that triggered the event. This treatment removes a trigger bias for the efficiency measurement. The muon track matched with the trigger object is called "Tag" and the other track is called "Probe" [16].	51

2.30	Muon single trigger efficiency used in the study. While the RPC covers the barrel region ($ \eta < 1.05$) as a muon trigger detector, the TGC covers the end-cap region ($1.05 < \eta < 2.4$). The Level 1 trigger threshold in the barrel region which is the seed for the 18GeV trigger was changed in order to keep within the allocated bandwidth for the Level 1 muon trigger, from L1_MU10 to L1_MU11 (a). The L1_MU10 consists of two station coincidence trigger in the barrel region, while the L1_MU11 is composed of coincidence of hits from three stations. Due to the smaller geometric coverage of the additional chambers required to form three-station coincidence triggers and hit efficiencies of the additional chambers, the L1_MU11 shows the efficiency drop of about 6 %. Following the change, the EF trigger efficiency in the barrel region also changed (c) [17].	52
2.31	The concept for the electron/photon trigger algorithm [15].	53
2.32	Electron trigger efficiency [18]. Integrated luminosities 1.8 fb^{-1} , 0.6 fb^{-1} and 2.5 fb^{-1} were recorded by ATLAS when lowest unprescaled triggers were e20_medium, e22_medium and e22vh_medium1 , respectively.	55
2.33	Combined muon reconstruction efficiency with respect to the inner tracking efficiency as a function of the η (a) and p_T (b) of the muon for $p_T > 15\text{GeV}$ [19]. Chain 1 in the legend indicates the STACO algorithm and μ is the number of average interactions per bunch crossing. The name of calo muons shown in the legend of (a) indicates another reconstruction algorithm which is not used in the study.	58
2.34	Invariant mass of $Z \rightarrow \mu\mu$	59
2.35	Identification efficiency in terms of the number of reconstructed vertices. The p_T range of the electrons is between 20GeV and 50GeV. The suffix ”++” attached to the name of each criteria means they are refined ones dedicated to 2011 data. The identification efficiency is found to drop. This loss is mainly due to an enhanced hadronic activity overlaid to the electron calorimetric shower [20].	60
2.36	Invariant mass of $Z \rightarrow e^+e^-$	61
2.37	Distribution of E_T^{miss} as measured in a data sample of $Z \rightarrow \mu\mu$ (a) and $W \rightarrow e\nu$ (b) events. The expectation from Monte Carlo simulation (PYTHIA 6) is superimposed and normalized to data, after each MC sample is weighted with its corresponding cross-section. The lower part of figures show the ratio of data over MC [21].	63
2.38	E_x^{miss} and E_y^{miss} resolution as a function of the total transverse energy in the event calculated by summing the p_T of muons and the total transverse energy in the calorimeter in data at $\sqrt{s} = 7\text{TeV}$ (a) and MC (b) [21].The resolution of the two E_T^{miss} components is fitted with a function $\sigma = k \sqrt{\Sigma E_T}$ and the fitted values of the parameter k , expressed in $\text{GeV}^{1/2}$, are in the figure.	64
3.1	Beam Condition Monitor [22]	67
3.2	Integrated Luminosity in 2011.	69
3.3	The average number of interactions per bunch crossing for the different periods.	71

3.4	Invariant mass of two leptons which are the closest to the Z mass in the event. These distributions are the ones before the Z mass requirement. (a) is the one of muon pairs and (b) is the one of electrons.	74
3.5	Distributions of the E_T^{miss} before the cut.	75
3.6	Distributions of the transverse mass of the W boson before the cut.	76
3.7	Scale Factor of the muon reconstruction efficiency. They are measured in ten regions for each side as described in Section 2.3.5.	77
3.8	Scale Factor of the reconstruction and identification efficiency for electrons. . .	78
3.9	Scale Factor of the isolation efficiency.	78
3.10	Trigger efficiency of EF_mu18_inside-out for the Scale Factor. (a) to (d) are the ones with respect to the Combined or Segment-Tagged muon, while (e) to (h) are the ones with respect to the Combined muon.	79
3.11	Trigger efficiency of EF_mu18_inside-out_medium for the Scale Factor. (a) to (d) are the ones with respect to the Combined or Segment-Tagged muon, while (e) to (h) are the ones with respect to the Combined muon.	80
3.12	Trigger efficiency of EF_e20_medium for the Scale Factor. (a) and (b) are the one with respect to the Loose electron, while (c) and (d) are the ones with respect to the Tight electron.	81
3.13	Trigger efficiency of EF_e22_medium for the Scale Factor. (a) and (b) are the one with respect to the Loose electron, while (c) and (d) are the ones with respect to the Tight electron.	81
3.14	Trigger efficiency of EF_e22vh_medium1 for the Scale Factor. (a) and (b) are the one with respect to the Loose electron, while (c) and (d) are the ones with respect to the Tight electron.	82
3.15	Isolation cone. While only the charged tracks (orange arrows) in the same vertex are mainly used in the tracking isolation, tracks coming from other vertices or neutral particles (blue arrows) also contribute to the calorimetric isolation. .	83
3.16	Isolation efficiency (x-axis) versus rejection efficiency (y-axis) of four types of isolation variables for electrons with three different cone sizes.	85
3.17	Comparison between relative isolations. The magenta triangle is the adopted point used for the electron selection.	86
3.18	The illustration of the d_0 and z_0 . While the d_0 is defined as the transverse impact parameter, the z_0 is longitudinal one. In this thesis, they are defined with respect to the interaction point unless otherwise mentioned [23].	87
3.19	Distributions of the variables used for the muon selection before the cut on the variables displayed.	88
3.20	Distribution of muon quantities in the $Z \rightarrow \mu\mu$ sample after the selections for muons (1).	89
3.21	Distribution of muon quantities in the $Z \rightarrow \mu\mu$ sample after the selections for muons (2). (a) and (b) are the distribution of CB + ST. The presence of the detector support structure ($\phi \sim -1.5$), magnet support (every $\pi/8$ at $ \eta \simeq 0.4$ and 0.75), services for the calorimeters ($ \eta \simeq 0$) can be seen in η - ϕ plane (a). $ \eta \simeq 1.2$ is the transition region of the magnetic field. Muons around the region are recovered by the Segment-Tagged algorithm (e).	90

3.22	Distributions of the variables used for the electron selection before the cut on the variables displayed.	92
3.23	Distribution of electron quantities in the $Z \rightarrow ee$ sample after the selections for electrons. (a) E_T (p_T) distributions measured at the calorimeter ("cluster" in the figure), the ID ("track" in the figure) and truth information. The cluster energy is employed for E_T of electrons in this analysis. (c) ΔR distributions between the truth information and the position measured at the calorimeter or the ID. The positions of the ID are employed for the ones of electrons in this analysis. .	93
3.24	The expected number of MC events after each cut and correction. The number of events in data after each cut are also shown.	94
3.25	Missing leptons in ZZ. p_T of each truth lepton is greater than 15GeV.	97
3.26	(a) Invariant mass distribution for the lepton pair closet to the Z boson mass after all selection cuts except the Z mass cut in $t\bar{t}$ simulation sample. (b) E_T^{miss} distribution after all selection cuts except the Z mass cut in $t\bar{t}$ simulation sample.	98
3.27	E_T^{miss} distribution after all selection cuts with a pair of same charge having a mass closest to the Z mass in $\mu\mu e$ channel (a) and $ee\mu$ channel (b).	99
3.28	Matrix for the data-driven on Z +jets	100
3.29	p_T of additional electrons in low E_T^{miss} region	100
3.30	p_T of additional muons in low E_T^{miss} region	100
3.31	Fake lepton factor in bins of p_T^Z	101
3.32	Distributions after all selection cuts 1.	106
3.33	Distributions after all selection cuts 2.	107
3.34	Distributions after all selection cuts 3. The missing E_Z and the invariant mass of WZ are estimated by assuming the W boson mass.	108
3.35	Distributions after all selection cuts 4.	109
3.36	Distributions after all selection cuts 5.	110
3.37	Distributions after all selection cuts 6.	111
3.38	An event display of the typical WZ candidate (Run number: 191425, Event: 4424703). The upper left window shows the X-Y plane of the detector. Two bold red lines are muons of the Z candidate, while the bold green line is the electron derived from the W candidate. The red arrow in the figure indicates the direction of E_T^{miss} . The upper right window shows the η - ϕ plane. The bottom window shows the z-R plane around the interaction point. Vertices are shown on the window.	112
5.1	The aTGC parameter dependence on the cross section at 7 TeV.	120
5.2	The impact of aTGCs on the truth distributions.	121
5.3	The p_T distribution of Z bosons.	122
5.4	Limits of the aTGC parameters.	125

- 6.1** Comparison of the cross-section with other experiments results. The cross-section measured by the CDF is $3.9_{-0.5}^{+0.6}(\text{stat.})_{-0.5}^{+0.6}(\text{syst.})$ pb [3] and the one of the D0 is $3.9_{-0.9}^{+1.1}$ pb [4]. The prediction of the cross-section at 1.96TeV is 3.5 ± 0.21 pb, which is quoted from [3]. The cross-section measured by the CMS is $17.0 \pm 2.4(\text{stat.}) \pm 1.1(\text{syst.}) \pm 1.0(\text{lumi.})$ pb [24]. The prediction of the cross-section at 7TeV is $17.6_{-1.0}^{+1.1}$ pb. 127

List of Tables

1.1	Coupling constants between a Z boson and fermions	9
1.2	Branching ratio of W boson [25].	11
1.3	Branching ratio of Z boson [25].	12
1.4	Observed 95 % C.I. on the aTGC by the CDF and D0 experiments.	19
2.1	The design parameters of the LHC and the ones in 2011 [26] [27].	23
2.2	Designed Performance	26
2.3	Granularity of the calorimeter	36
2.4	magnetic-field-related performance specification	48
3.1	Total recorded events and integrated luminosity in 2011. The integrated luminosity selected by a GRL, which is used in the study, is also shown.	68
3.2	Run numbers and integrated luminosity in each period.	68
3.3	Electron and muon triggers that are used in the analysis. The convention of the naming for triggers is explained in Section 2.4.1.	73
3.4	A matrix for determination of the isolation variables and their values. Events with Z boson candidate are selected. The Z boson candidate is identified when two leptons in the event has an invariant mass $ M_{ll} - M_{Z,PDG} < 10\text{GeV}$. Remaining leptons are identified as the ones of non Z boson.	84
3.5	The expected number of signal events after each cut for $W^\pm Z \rightarrow \ell\nu\ell'\ell'$ for $\mathcal{L} = 4.64\text{fb}^{-1}$. The ℓ and ℓ' are muon or electron. The event in which τ lepton(s) decay into muon(s) or electron(s) is also included.	95
3.6	Relative acceptance of signal events after each cut for $W^\pm Z \rightarrow \ell\nu\ell'\ell'$ events. . .	95
3.7	Summary of all relative acceptance uncertainties (%) for each channel which is used in the cross-section calculation.	104
3.8	Summary of observed events and expected signal and background contributions in the four tri-lepton channels and combined. The first error is statistical while the second is systematic.	114
4.1	Measured total cross-sections for each channel and combined. The systematic uncertainty includes all sources except luminosity.	116
4.2	Relative systematic uncertainties (%) on the total cross-section for each channel and the combined result.	117

5.1	The number of observed events and expected signal and background contributions in different $p_T(Z)$ ranges used for anomalous Triple Gauge Coupling limit setting. The first error is statistical while the second is systematic.	123
5.2	Summary of all relative acceptance uncertainties (%) in bins of p_T^Z which is used in the calculation of the aTGC limit.	124
5.3	Observed and expected 95 % C.I. on the aTGC	125

Chapter 1

Introduction

The Standard Model of particle physics (SM) which was established in 1970's has tremendous success. Large Hadron Collider (LHC) was built at CERN to get a clearer picture of the SM, to explore the TeV energy region where new phenomena are expected to be observed, and to make it clear whether the Higgs boson really exists, or not. The ATLAS (A Toroidal Lhc ApparatuS) experiment was designed to catch extensive range of signals which indicate interesting physics. The experiment is expected to bring fruitful new knowledges concerning the elementary particle physics, and they could change our world view.

The SM can explain almost all phenomena of the elementary particles which have been observed until today. It is composed of the following two presuppositions.

- Minimum composition elements of materials are quarks and leptons. They are fermions and six types are known for both quarks and leptons.

Quarks Protons and neutrons, which compose all materials, consist of the up quark having electric charge of $+\frac{2}{3}e$ and the down quark having the charge of $-\frac{1}{3}e$. They are bound together by the strong force. And they are also involved in the weak interaction as a pair. In addition to the up and down quarks, charm, strange, bottom and top quarks exist. While the charm and top quarks have the charge of $+\frac{2}{3}e$, the strange and bottom have the charge of $-\frac{1}{3}e$. The charm quark makes an isospin doublet with the strange quark and the top quark makes a pair with the bottom quark.

Leptons In the elementary particles composing material, the ones which are not involved in the strong interaction are called leptons. The leptons are further divided into two types, one is charged leptons which are electron (e), muon (μ), tau (τ) and the other is neutral leptons which are electron neutrino (ν_e), muon neutrino (ν_μ), tau neutrino (ν_τ). The neutral leptons are also called neutrinos. Each neutrino makes a pair with each charged lepton and compose an isospin doublet, which is involved in the weak interaction.

- The force between the particles is mediated by gauge bosons and the mechanism is explained in a frame of a gauge theory. The forces which the SM treats are the electromagnetic force mediated by photons (γ), the weak force mediated by W^\pm and Z bosons, and the strong force mediated by gluons. The source of the electromagnetic force is the electric charge, the one for weak force is the weak charge which all quarks and leptons have.

The source of the strong interaction is three types of color charges and the interaction has $SU(3)$ symmetry. And the electromagnetic force and the weak force are unified as the electroweak interaction, which has $SU(2) \times U(1)$ symmetry.

Figure 1.1 shows the relation of quarks, leptons and forces.

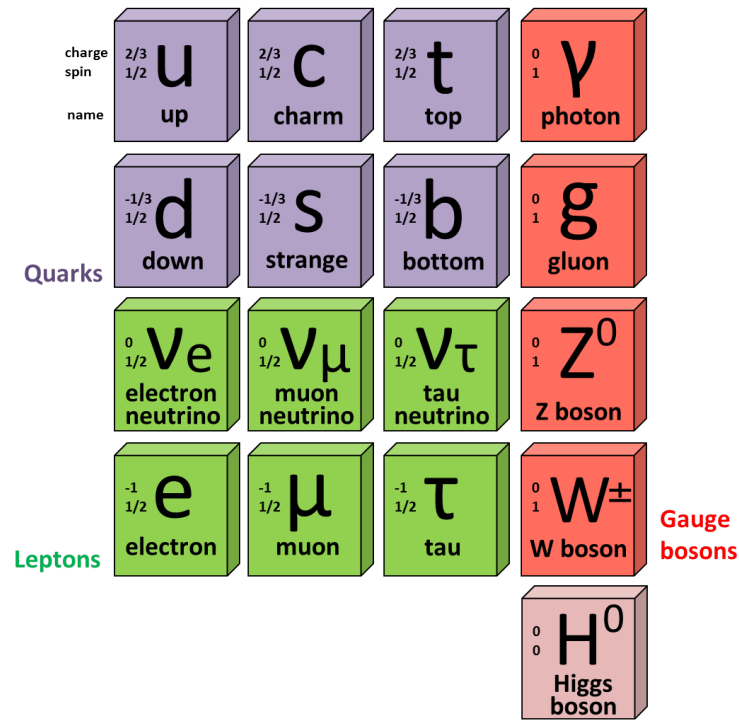


Figure 1.1: Quarks, leptons and force carriers in the SM.

The unification of the electroweak interaction is a key ingredient for the Standard Model. In the following sections, we see how the electromagnetic and weak forces are unified with the gauge theory and what the unified theory predicts.

1.1 The Unification of Electroweak Interaction

In nature, several types of fundamental interaction or fields act between particles, and many physicists tried to understand the interrelation between the different fundamental fields.

In the late 1960's Weinberg, Salam, and Glashow described how it might be possible to treat electromagnetic and weak interactions as different aspects of a single electroweak interaction, with the same coupling. In this section, firstly we see how the gauge theory introduces electromagnetic and weak interactions naturally, and then the idea of unification of the electroweak interaction is presented.

1.1.1 $U(1)$ Gauge Symmetry (The Quantum Electrodynamics)

The Dirac Lagrangian for a free fermion with mass of m can be written as

$$\mathcal{L} = i\bar{\psi}\gamma^\mu\partial_\mu\psi - m\bar{\psi}\psi, \quad (1.1)$$

where ψ is the Dirac spinor. Here consider a local phase transformation for the ψ as

$$\psi \rightarrow e^{i\theta(x^\nu)}\psi, \quad (1.2)$$

where $\theta(x^\nu)$ depends on space and time in a completely arbitrary way. An infinite set of phase transformations forms a unitary group called $U(1)$. Since $\theta(x^\nu)$ is a scalar quantity, the $U(1)$ group is said to be Abelian. The Lagrangian, however, is not invariant for the transformations. In order to make the Lagrangian gauge invariant under such the local phase transformations, the derivative ∂_μ needs to be modified to the covariant derivative D_μ as

$$D_\mu \equiv \partial_\mu - ieA_\mu,$$

where e corresponds to the electric charge and A_μ is a vector field, or called the gauge field, which transforms with the local gauge transformation as

$$A_\mu \rightarrow A_\mu - \frac{1}{e}\partial_\mu\theta(x^\nu). \quad (1.3)$$

Under the simultaneous transformation on $\partial_\mu\psi$ and A_μ we get

$$\mathcal{L} = i\bar{\psi}\gamma^\mu D_\mu\psi - m\bar{\psi}\psi = \{i\bar{\psi}\gamma^\mu\partial_\mu\psi - m\bar{\psi}\psi\} + e\bar{\psi}\gamma^\mu\psi A_\mu. \quad (1.4)$$

By demanding a local gauge invariance, we are forced to introduce the gauge field A_μ . The field couples to the Dirac particle with strength $-e$, thus which can be regarded as the photon field.

To get the complete Lagrangian of the Quantum Electrodynamics (QED), a term corresponding to the kinetic energy of the photon field has to be added to the above Lagrangian. The term, also, must be invariant under the transformation (1.3). Since the photon field is a vector field of spin 1, it can be expressed by the Proca Lagrangian, which is

$$\mathcal{L} = -\frac{1}{4}F^{\mu\nu}F_{\mu\nu} + \frac{1}{2}m^2 A^\nu A_\nu. \quad (1.5)$$

The second term showing the mass of the boson, however, is not invariant. It means that if the local gauge symmetry is required the photon has to be massless. Finally, the Lagrangian of the Quantum Electrodynamics (QED) can be expressed with the Lagrangian of (1.4) and the first term of the Proca Lagrangian as

$$\mathcal{L} = \{i\bar{\psi}\gamma^\mu\partial_\mu\psi - m\bar{\psi}\psi\} + e\bar{\psi}\gamma^\mu\psi A_\mu - \frac{1}{4}F_{\mu\nu}F^{\mu\nu}. \quad (1.6)$$

1.1.2 The Grashow-Weinberg-Salam (GWS) Theory

$SU(2)$ gauge symmetry

While a simple local phase transition as seen in the $U(1)$ belongs to the Abelian group, more complex phase transformations specified by non-commuting operators belong to the non-Abelian groups. Such gauge transformations were proposed by Yang and Mills in 1954 [28], and involved fields containing both charged and neutral massless bosons. Specifically, they chose the group $SU(2)$ of isospin, which involves the non-commuting Pauli matrices.

In the weak interaction, a left handed fermion in the same generation can change into the partner of the doublet. This means the weak interaction is a symmetric interaction for left-handed fermions. In an analogous fashion to QED, here a local gauge symmetry is required on the weak interaction. At first, consider a two fermion field which can be treated as doublet.

$$\begin{aligned} \psi &\equiv \begin{pmatrix} \psi_1 \\ \psi_2 \end{pmatrix} \\ \bar{\psi} &= (\bar{\psi}_1, \bar{\psi}_2) \end{aligned} \quad (1.7)$$

where ψ_1 and ψ_2 are the Dirac spinors. The Lagrangian of two fermions without interaction between them can be express as

$$\mathcal{L} = i\bar{\psi}\gamma^\mu\partial_\mu\psi - \bar{\psi}M\psi, \quad (1.8)$$

where M is a matrix of

$$M = \begin{pmatrix} m & 0 \\ 0 & m. \end{pmatrix} \quad (1.9)$$

m is the masses of the two fermions. Consider a local phase transformation for the ψ of the form

$$\psi \rightarrow U\psi, \quad (1.10)$$

where the U is a unitary matrix described as

$$U = \exp(i\theta) \exp(i\lambda(x^\nu) \cdot \boldsymbol{\tau}), \quad (1.11)$$

where $\lambda(x^\nu)$ is an vector whose components are real numbers chosen arbitrarily at different space-time points x , $\boldsymbol{\tau}$ is a vector of Pauli matrices τ_1, τ_2, τ_3 . Since the Lagrangian is not invariant under the transformation, the derivative ∂_μ needs to be modified to the covariant D_μ to make it gauge invariant as

$$D_\mu \equiv \partial_\mu + ig\mathbf{W}_\mu \cdot \boldsymbol{\tau}, \quad (1.12)$$

where \mathbf{W}_μ is a vector of three vector fields $\mathbf{W}_\mu \equiv (W_{1\mu}, W_{2\mu}, W_{3\mu})$, g is a real number which represents a strength of the interaction between fermions and vector fields \mathbf{W}_μ . The \mathbf{W}_μ transforms with the local gauge transformation as

$$\mathbf{W}_\mu \cdot \boldsymbol{\tau} \rightarrow U \mathbf{W}_\mu \cdot \boldsymbol{\tau} U^\dagger + i \frac{1}{g} (\partial_\mu U) U^\dagger. \quad (1.13)$$

Under the simultaneous transformation on $\partial_\mu \psi$ and \mathbf{W}_μ we get

$$\mathcal{L} = i\bar{\psi}\gamma^\mu D_\mu \psi - \bar{\psi} M \psi = \{i\bar{\psi}\gamma^\mu \partial_\mu \psi - \bar{\psi} M \psi\} - g\bar{\psi}\gamma^\mu (\mathbf{W}_\mu \cdot \boldsymbol{\tau}) \psi. \quad (1.14)$$

The third term of the Lagrangian represents the interaction between the field of fermion pair and the gauge field with a strength $-g$. Like the case of QED, a term corresponding to the kinetic energy of the gauge field has to be added to the above Lagrangian to get the complete one. Since $SU(2)$ is a non-Abelian group unlike $U(1)$, the $F^{\mu\nu}$ tensor is modified to be gauge invariant under the local gauge transformation of $SU(2)$.

$$F^{\mu\nu} \equiv \partial^\mu \mathbf{W}^\nu - \partial^\nu \mathbf{W}^\mu - 2g (\mathbf{W}^\mu \times \mathbf{W}^\nu). \quad (1.15)$$

Finally, the Lagrangian can be expressed with the Lagrangian of (1.14) and the first term of the Proca Lagrangian with modified $F^{\mu\nu}$ tensor as

$$\mathcal{L} = \{i\bar{\psi}\gamma^\mu \partial_\mu \psi - \bar{\psi} M \psi\} - g\bar{\psi}\gamma^\mu (\mathbf{W}_\mu \cdot \boldsymbol{\tau}) \psi - \frac{1}{4} F_{\mu\nu} F^{\mu\nu}. \quad (1.16)$$

The masses of gauge bosons are prohibited as in the case of QED.

The Weinberg-Salam $SU(2) \times SU(1)$ model

In 1967-1968 Weinberg and Salam proposed a gauge theory unifying weak and electromagnetic interactions based on an $SU(2)$ group of weak isospin T and a $U(1)$ group of weak hypercharge Y [29] [30]. Consider a left-handed massless fermion pair forming isospin doublets ψ_1 and two right-handed massless fermions, which are isosinglets ψ_2 and ψ_3 . In a case of an electron and its neutrino, they are

$$\psi_1 = \begin{pmatrix} \nu_{eL} \\ e_L \end{pmatrix}, \psi_2 = \nu_{eR}, \psi_3 = e_R. \quad (1.17)$$

For the case of up and down quarks, they are

$$\psi_1 = \begin{pmatrix} u_L \\ d_L \end{pmatrix}, \psi_2 = u_R, \psi_3 = d_R. \quad (1.18)$$

The Lagrangian without interactions is

$$\mathcal{L}_0 = \sum_{j=1}^3 i\bar{\psi}_j \gamma^\mu \partial_\mu \psi_j. \quad (1.19)$$

The local $SU(2) \times U(1)$ transformation G which is for the left and right-handed components is

$$\begin{aligned}\psi_1 &\xrightarrow{G} \psi'_1 \equiv \exp(i\lambda(x^\nu) \cdot \boldsymbol{\tau}) \exp(iY_1\Lambda(x^\nu)) \psi_1, \\ \psi_2 &\xrightarrow{G} \psi'_2 \equiv \exp(iY_2\Lambda(x^\nu)) \psi_2, \\ \psi_3 &\xrightarrow{G} \psi'_3 \equiv \exp(iY_3\Lambda(x^\nu)) \psi_3,\end{aligned}\tag{1.20}$$

where Y_j is a weak hypercharge defined as

$$Q \equiv T_3 + \frac{Y}{2},\tag{1.21}$$

where Q is the electric charge and T_3 is the third component of the weak isospin which can have $\pm\frac{1}{2}$. Invariance of the \mathcal{L}_0 under the transformation is obtained by introducing a covariant derivative of the form

$$D_\mu \equiv \partial_\mu + ig\mathbf{W}_\mu \cdot \boldsymbol{\tau} + ig' \frac{Y_j}{2} B_\mu.\tag{1.22}$$

With the transformation and the local gauge transformation described in Equation (1.3) and (1.13) we get,

$$\begin{aligned}\mathcal{L} &= \sum_{j=1}^3 i\bar{\psi}_j \gamma^\mu D_\mu \psi_j \\ &= \sum_{j=1}^3 i\bar{\psi}_j \gamma^\mu \partial_\mu \psi_j \\ &\quad + i\bar{\psi}_1 \gamma^\mu \left\{ ig \left(W_{1\mu} \frac{\tau_1}{2} + W_{2\mu} \frac{\tau_2}{2} \right) \right\} \psi_1 \\ &\quad + i\bar{\psi}_1 \gamma^\mu \left(ig W_{3\mu} \frac{\tau_3}{2} \right) \psi_1 + \sum_{j=1}^3 i\bar{\psi}_j \gamma^\mu \left(ig' \frac{Y_j}{2} B_\mu \right) \psi_j.\end{aligned}\tag{1.23}$$

The second term which is named \mathcal{L}_{int}^{CC} (CC: Charged Current) here shows the interaction between fermions and gauge bosons W^+ and W^- . The W^+ and W^- are defined as below.

$$W_\mu^\pm \equiv \frac{1}{\sqrt{2}} (W_{1\mu} \mp iW_{2\mu}).\tag{1.24}$$

With W^+ and W^- , \mathcal{L}_{int}^{CC} can be also expressed as

$$\begin{aligned}\mathcal{L}_{int}^{CC} &= i\bar{\psi}_1 \gamma^\mu \left\{ ig \left(W_{1\mu} \frac{\tau_1}{2} + W_{2\mu} \frac{\tau_2}{2} \right) \right\} \psi_1 \\ &= i\bar{\psi}_1 \gamma^\mu \left\{ i\frac{g}{2} \begin{pmatrix} 0 & W_{1\mu} - iW_{2\mu} \\ W_{1\mu} + iW_{2\mu} & 0 \end{pmatrix} \right\} \psi_1 \\ &= -\frac{g}{\sqrt{2}} \bar{\psi}_1 \gamma^\mu \begin{pmatrix} 0 & W_\mu^+ \\ W_\mu^- & 0 \end{pmatrix} \psi_1.\end{aligned}\tag{1.25}$$

It shows that regardless of leptons or quarks, W^\pm bosons couple to fermions with the strength $-g$. For $W_{3\mu}$ and B_μ in Equation (1.23), any state mixing these two fields is possible.

$$\begin{pmatrix} A_\mu \\ Z_\mu \end{pmatrix} \equiv \begin{pmatrix} \cos \theta_W & \sin \theta_W \\ -\sin \theta_W & \cos \theta_W \end{pmatrix} \begin{pmatrix} B_\mu \\ W_{3\mu} \end{pmatrix}, \quad (1.26)$$

where A_μ and Z_μ are the electromagnetic field and the weak neutral field, respectively, θ_W is the Weinberg angle which is determined by experiments and it is

$$\sin^2 \theta_W \simeq 0.23. \quad (1.27)$$

With A_μ and Z_μ , the third term in the Equation (1.23) which is named \mathcal{L}_{int}^{NC} (NC: Neutral Current) here can be expressed as

$$\begin{aligned} \mathcal{L}_{int}^{NC} = & - \sum_{j=1}^3 \bar{\psi}_j \gamma^\mu \left[A_\mu \left(g \sin \theta_W T_3 + g' \cos \theta_W \frac{Y_j}{2} \right) \right. \\ & \left. - Z_\mu \left(g \cos \theta_W T_3 - g' \sin \theta_W \frac{Y_j}{2} \right) \right] \psi_j. \end{aligned} \quad (1.28)$$

Considering the fact that the electromagnetic field does not couple directly neutrinos and the coupling of the electromagnetic field has the strength required in QED as seen in the Section 1.1.1 we get,

$$g \sin \theta_W = g' \cos \theta_W = e. \quad (1.29)$$

The \mathcal{L}_{int}^{NC} can be finally written with the above Equation and (1.21),

$$\mathcal{L}_{int}^{NC} = \sum_{j=1}^3 e \bar{\psi}_j \gamma^\mu Q \psi_j A_\mu + \sum_{j=1}^3 \frac{e}{\sin \theta_W \cos \theta_W} \bar{\psi}_j \gamma^\mu (T_3 - Q \sin^2 \theta_W) \psi_j Z_\mu. \quad (1.30)$$

This term shows us that the A_μ couples to fermions with the charge of Qe and the neutral weak boson Z_μ couples to fermions with the strength of $\frac{e}{\sin \theta_W \cos \theta_W} (T_3 - Q \sin^2 \theta_W)$. Table 1.1 shows the coupling constants between the Z boson and each fermion.

Now we see that the electromagnetic and weak interactions are successfully led from a common gauge transformation of $SU(2)_L \times U(1)_Y$.

The term of the kinetic energy for four gauge bosons \mathcal{L}_{gauge} also needs to be added and which is expressed as

$$\mathcal{L}_{gauge} = -\frac{1}{4} B^{\mu\nu} B_{\mu\nu} - \frac{1}{4} W^{\mu\nu} W_{\mu\nu}, \quad (1.31)$$

where $B^{\mu\nu}$ and $W^{\mu\nu}$ are defined as

$$\begin{aligned} B^{\mu\nu} & \equiv \partial^\mu B^\nu - \partial^\nu B^\mu, \\ W^{\mu\nu} & \equiv \partial^\mu W^\nu - \partial^\nu W^\mu - 2g(W^\mu \times W^\nu). \end{aligned} \quad (1.32)$$

The masses of gauge bosons are also prohibited by the requirement of the local gauge symmetry for $SU(2) \times U(1)$.

fermion	T_3	Q	$T_3 - Q \sin^2 \theta_W$
$\nu_{eL} \nu_{\mu L} \nu_{\tau L}$	$+\frac{1}{2}$	0	$+\frac{1}{2}$
$e_L \mu_L \tau_L$	$-\frac{1}{2}$	-1	$-\frac{1}{2} + \sin^2 \theta_W$
$\nu_{eR} \nu_{\mu R} \nu_{\tau R}$	0	0	0
$e_R \mu_R \tau_R$	0	-1	$\sin^2 \theta_W$
$u_L c_L t_L$	$+\frac{1}{2}$	$+\frac{2}{3}$	$+\frac{1}{2} - \frac{2}{3} \sin^2 \theta_W$
$d_L s_L b_L$	$-\frac{1}{2}$	$-\frac{1}{3}$	$-\frac{1}{2} + \frac{1}{3} \sin^2 \theta_W$
$u_R c_R t_R$	0	$+\frac{2}{3}$	$-\frac{2}{3} \sin^2 \theta_W$
$d_R s_R b_R$	0	$-\frac{1}{3}$	$+\frac{1}{3} \sin^2 \theta_W$

Table 1.1: Coupling constants between a Z boson and fermions

The Higgs mechanism As described above, mass terms of gauge bosons are prohibited by the gauge symmetry. However, the actual W and Z bosons have mass [25] of

$$m_W = 80.399 \pm 0.023 \text{ GeV}, \quad (1.33)$$

$$m_Z = 91.1876 \pm 0.0021 \text{ GeV}. \quad (1.34)$$

To get W^\pm and Z bosons massive without breaking the local gauge symmetry, four real scalar fields ϕ_i are introduced. A Lagrangian \mathcal{L}_{scalar} which is $SU(2) \times U(1)$ gauge invariant for the scalar fields is

$$\mathcal{L}_{scalar} = (D_\mu \phi)^\dagger D_\mu \phi - V(\phi^\dagger \phi), \quad (1.35)$$

where D_μ is a covariant derivative which has the same structure of Equation (1.22). The ϕ_i must also belong to $SU(2) \times U(1)$ multiplets. The most economical choice for the ϕ is to arrange four fields in an isospin doublet with weak hypercharge $Y = 1$.

$$\phi = \begin{pmatrix} \phi^+ \\ \phi^0 \end{pmatrix} \quad (1.36)$$

$$\phi^+ \equiv (\phi_1 + i\phi_2) / \sqrt{2},$$

$$\phi^0 \equiv (\phi_3 + i\phi_4) / \sqrt{2},$$

where +, 0 represent the electric charge of each complex component. As the potential $V(\phi^\dagger \phi)$ in Equation (1.35),

$$V(\phi^\dagger \phi) = \mu^2 \phi^\dagger \phi + \lambda (\phi^\dagger \phi)^2 \quad (1.37)$$

is chosen. In the case of $\mu^2 < 0$ and $\lambda > 0$, the potential has its minimum at a finite value where

$$\phi^\dagger \phi = -\frac{\mu^2}{2\lambda}. \quad (1.38)$$

Since the \mathcal{L}_{scalar} is local gauge invariant under $SU(2)$ transformations, we can choose a vacuum expectation value of ϕ as below by performing the transformation for the $\phi(x^\nu)$.

$$\phi_{\text{vacuum}} = \sqrt{\frac{1}{2}} \begin{pmatrix} 0 \\ v \end{pmatrix}, \quad (1.39)$$

$$v = \frac{\mu}{\lambda}.$$

A choice of the actual vacuum state among them violates $SU(2) \times U(1)$ symmetry. This mechanism is called spontaneous symmetry breaking. Although ϕ_{vacuum} breaks $SU(2) \times U(1)$ symmetry, $U(1)$ symmetry remains unbroken since ϕ_{vacuum} is neutral. As a result, the photon remains massless by the spontaneous symmetry breaking. If a field of real function $h(x^\nu)$ is introduced in the ϕ_{vacuum} ,

$$\phi_{\text{vacuum}} = \sqrt{\frac{1}{2}} \begin{pmatrix} 0 \\ v + h(x^\nu) \end{pmatrix}. \quad (1.40)$$

With the Equation (1.26), the gauge boson masses are identified by substituting the above vacuum expectation value into the Lagrangian $\mathcal{L}_{\text{scalar}}$.

$$\begin{aligned} \mathcal{L}_{\text{scalar}} &= \frac{1}{2} \partial_\mu h \partial^\mu h + \mu^2 h^2 + \\ &\quad \frac{g^2 v^2}{4} W^+ W^- + \frac{\sqrt{g^2 + g'^2}}{8} v^2 Z_\mu Z^\mu + \\ &\quad \frac{g^2 v h}{4} W^+ W^- + \frac{\sqrt{g^2 + g'^2}}{8} v h Z_\mu Z^\mu + O(h^2). \end{aligned} \quad (1.41)$$

The first term is the kinetic term of the SM Higgs boson, the term from second to fourth are the mass terms of Higgs (m_H), W (m_W) and Z (m_Z) bosons, respectively,

$$m_H = \sqrt{-2\mu^2}, \quad (1.42)$$

$$m_W = gv/2, \quad (1.43)$$

$$m_Z = \sqrt{g^2 + g'^2} v/2. \quad (1.44)$$

The vacuum expectation value is calculated as $v = (\sqrt{2}G_F)^{1/2} \sim 246$ GeV. The fifth and sixth terms in Equation (1.41) are the interaction between Higgs and W, Z bosons.

Fermion masses are also explained by the Higgs mechanism and by introducing Yukawa Lagrangian $\mathcal{L}_{\text{Yukawa}}$. To summarize the section here, the Lagrangian in the Weinberg-Salam model is expressed as

$$\mathcal{L}_{\text{weinberg-salam}} = \mathcal{L}_0 + \mathcal{L}_{\text{int}}^{\text{CC}} + \mathcal{L}_{\text{int}}^{\text{NC}} + \mathcal{L}_{\text{gauge}} + \mathcal{L}_{\text{scalar}} + \mathcal{L}_{\text{Yukawa}}. \quad (1.45)$$

1.1.3 Decay of the Weak Bosons

W boson W bosons are generated and decay only through the interaction with two fermions which make up a left-hand isospin doublet. The tree level Feynman diagram of the $W \rightarrow f \bar{f}'$ (f : fermion) vertex is depicted in Figure 1.2. Decays to quark states which contain quarks in different generations like (u, s) is realized through an off-diagonal element of the CKM Matrix.

The decay width of the W boson to leptons is written with an assumption that the lepton mass is negligible

$$\begin{aligned} \Gamma(W^\pm \rightarrow l^\pm \nu) &= \frac{g^2 m_W}{48\pi} \\ &= \frac{G_F m_W^3}{6\sqrt{2}\pi}. \end{aligned} \quad (1.46)$$

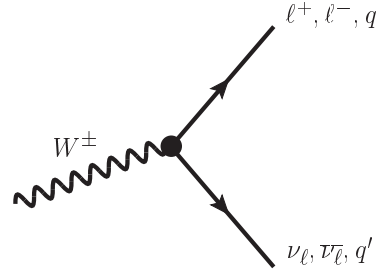


Figure 1.2: Tree level Feynmann diagram of the $W \rightarrow f\bar{f}'$ vertex.

Also the decay width to quarks can be written as

$$\begin{aligned}\Gamma(W^\pm \rightarrow q_i\bar{q}_j) &= N_c|V_{ij}|^2\Gamma_l \\ &= C\frac{G_F m_W^3}{2\sqrt{2}\pi}|V_{ij}|^2,\end{aligned}\quad (1.47)$$

where N_c ($=3$) is the color factor and V_{ij} is the corresponding CKM-Matrix element. C is a correction for QCD effect. Actual possible pairs to which the W bosons can decay are listed in Table 1.2 [25].

Decay mode	Branching ratio [%]
$e\bar{\nu}_e$	10.75 ± 0.13
$\mu\bar{\nu}_\mu$	10.57 ± 0.15
$\tau\bar{\nu}_\tau$	11.25 ± 0.20
hadrons	67.60 ± 0.27

Table 1.2: Branching ratio of W boson [25].

Z boson The Z boson can couple to both left-handed and right-handed fermions. The tree level Feynman diagram of the $Z \rightarrow f\bar{f}$ vertex is depicted in Figure 1.3.

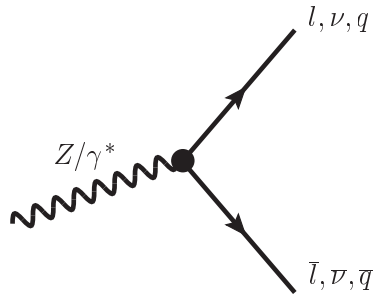


Figure 1.3: Tree level Feynmann diagram of the $Z \rightarrow f\bar{f}$ vertex.

The decay width of $Z \rightarrow f\bar{f}$ channel is written as

$$\begin{aligned}\Gamma(Z \rightarrow \bar{f}f) &= \frac{N_{cf}g_z^2m_z}{48\pi}(1-4x)^{\frac{1}{2}}[v_f^2(1+2x)+a_f^2(1-4x)] \\ &= \frac{N_{cf}G_Nm_z^3}{6\sqrt{2}\pi}(1-4x)^{\frac{1}{2}}[v_f^2(1+2x)+a_f^2(1-4x)].\end{aligned}\quad (1.48)$$

where $x = m^2/m_Z^2$ (m is fermion mass). N_{cf} accounts for the QCD corrections as well as QED corrections [25].

Here, ignoring mass of quarks and leptons, one obtains

$$\begin{aligned}\Gamma(Z \rightarrow \bar{f}f) &= 2(v_f^2 + a_f^2)N_{cf}\Gamma_\nu, \\ \Gamma_\nu &= \frac{G_Nm_Z^3}{12\sqrt{2}\pi}.\end{aligned}\quad (1.49)$$

Γ_ν is a decay width for a certain type of a neutrino pair.

Actual possible pairs to which Z bosons can decay are listed in Table 1.3,

Decay mode	Branching ratio [%]
e^+e^-	3.363 ± 0.004
$\mu^+\mu^-$	3.366 ± 0.007
$\tau^+\tau^-$	3.367 ± 0.008
invisible	20.0 ± 0.06
hadrons	69.91 ± 0.06

Table 1.3: Branching ratio of Z boson [25].

1.1.4 Self-coupling of Bosons in the Electroweak Interaction

The $\mathcal{L}_{\text{gauge}}$ in Equation (1.45) can be also rewritten with the photon A_μ and three weak bosons W_μ^+ , W_μ^- , Z_μ instead of B_μ and W_μ [31]. In that case this Lagrangian can be divided into two groups, one is for Triple Gauge Couplings (TGC) and the other is for Quartic Gauge Couplings (QGC),

$$\mathcal{L}_{\text{gauge}} = \mathcal{L}_{\text{TGC}} + \mathcal{L}_{\text{QGC}}$$

More specifically each term is expressed as

$$\begin{aligned}\mathcal{L}_{\text{TGC}} &= -ie \cot \theta_W [(\partial^\mu W^{-\nu} - \partial^\nu W^{-\mu}) W_\mu^+ Z_\nu \\ &\quad - (\partial^\mu W^{+\nu} - \partial^\nu W^{+\mu}) W_\mu^- Z_\nu + W_\mu^- W_\nu^+ (\partial^\mu Z^\nu - \partial^\nu Z^\mu)] \\ &\quad - ie [(\partial^\mu W^{-\nu} - \partial^\nu W^{-\mu}) W_\mu^+ A_\nu \\ &\quad - (\partial^\mu W^{+\nu} - \partial^\nu W^{+\mu}) W_\mu^- A_\nu + W_\mu^- W_\nu^+ (\partial^\mu A^\nu - \partial^\nu A^\mu)],\end{aligned}\quad (1.50)$$

$$\begin{aligned}
\mathcal{L}_{\text{QGC}} = & -\frac{e^2}{2 \sin^2 \theta_W} [(W_\mu^+ W^{-\mu})^2 - W_\mu^+ W^{+\mu} W_\nu^- W^{-\nu}] \\
& -e^2 \cot^2 \theta_W (W_\mu^+ W^{-\mu} Z_\nu Z^\nu - W_\mu^+ Z^\mu W_\nu^- Z^\nu) \\
& -e^2 \cot \theta_W (2W_\mu^+ W^{-\mu} Z_\nu A^\nu - W_\mu^+ Z^\mu W_\nu^- A^\nu - W_\mu^+ A^\mu W_\nu^- Z^\nu) \\
& -e^2 (W_\mu^+ W^{-\mu} A_\nu A^\nu - W_\mu^+ A^\mu W_\nu^- A^\nu).
\end{aligned} \tag{1.51}$$

These self-coupling terms are a result of the fact that $SU(2) \times U(1)$ is a non-Abelian group. This prediction by the GWS theory is important since diagrams containing the self-coupling can cancel the divergence of other diagrams and make the theory well-behaved.

Here consider $e^-e^+ \rightarrow W^+W^-$ process as an example [32]. Figure 1.4 shows the diagrams at the lowest order and Figure 1.5 shows the WWV vertex, where V is γ or Z .

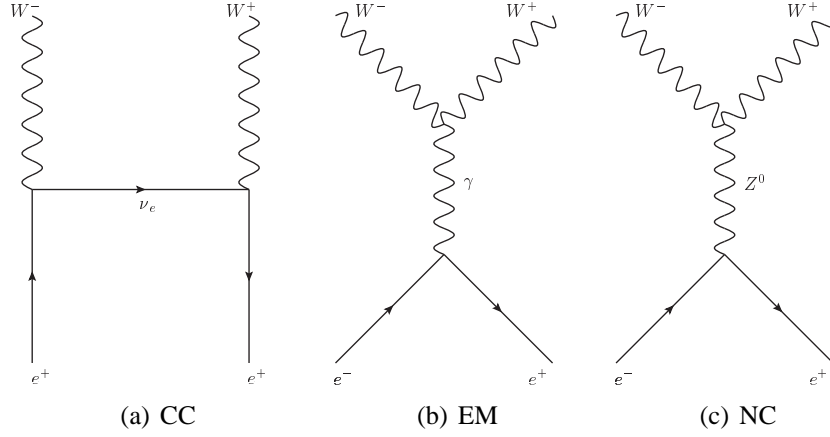


Figure 1.4: Diagrams of the process $e^+e^- \rightarrow W^+W^-$ at tree level.

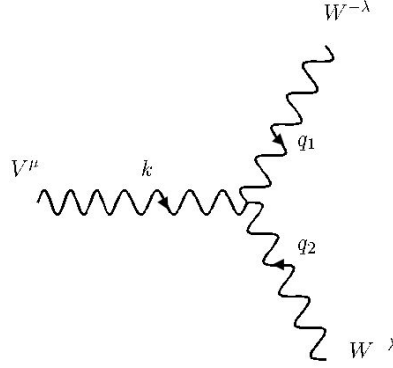


Figure 1.5: WWV vertex. $V = Z, \gamma$.

The vertex can be expressed as

$$\begin{aligned} i\Gamma_V^{\mu\nu\lambda} &= -i\gamma_V \left[(q_1 - q_2)^\mu g^{\nu\lambda} + (q_2 - k)^\nu g^{\lambda\mu} + (k - q_1)^\lambda g^{\mu\nu} \right], \\ \gamma_Z &= e \cot \theta_W, \\ \gamma_\gamma &= e, \end{aligned} \quad (1.52)$$

where $g^{\mu\nu}$ is the metric tensor of Lorentz transformation and k, q_1, q_2 are kinetic variables as shown in Figure 1.5. By the conservation of momentum,

$$k + q_1 + q_2 = 0. \quad (1.53)$$

The cross-section of $e^-e^+ \rightarrow W^+W^-$ is calculated by those relational expressions.

$$\begin{aligned} \sigma(e^+e^- \rightarrow W^+W^-) &= \frac{\pi\alpha^2\beta}{2sx_W^2} \left\{ \left[(1 + \lambda + 2\lambda^2) \frac{1}{\beta} \ln \left(\frac{1 + \beta}{1 - \beta} - \frac{5}{4} \right) \right] \right. \\ &\quad + \frac{m_Z^2(1 - 2x_W)}{(s - m_Z^2)} \left[2(2\lambda + \lambda^2) \frac{1}{\beta} \ln \left(\frac{1 + \beta}{1 - \beta} \right) - \frac{1}{12\lambda} - \frac{5}{3} - \lambda \right] \\ &\quad \left. + \frac{m_Z^4(1 - 4x_W + 8x_W^2)}{(s - m_Z^2)} \left[\beta^2 \left(\frac{1}{\lambda^2} + \frac{20}{\lambda} + 12 \right) \right] \right\}, \end{aligned} \quad (1.54)$$

$$\beta = \sqrt{1 - 4\lambda},$$

$$\lambda = \frac{m_W^2}{s},$$

$$x_W = \sin^2 \theta_W.$$

At $s \rightarrow \infty$, the first term becomes dominant,

$$\sigma(s \gg m_W^2) \rightarrow \left(\frac{\pi\alpha^2}{2x_W^2} \right) \frac{1}{s} \ln \frac{s}{m_W^2}. \quad (1.55)$$

Figure 1.6 shows the cross-section of $e^+e^- \rightarrow W^+W^-$ as a function of E_{cm} which denotes center of mass energy, which was measured by LEP. While each diagram in Figure 1.4 diverges at high s , they behaves properly as a total because each contributions are canceled suitably by each other. Thus the existence of self-couplings is important for the theory to be renormalizable.

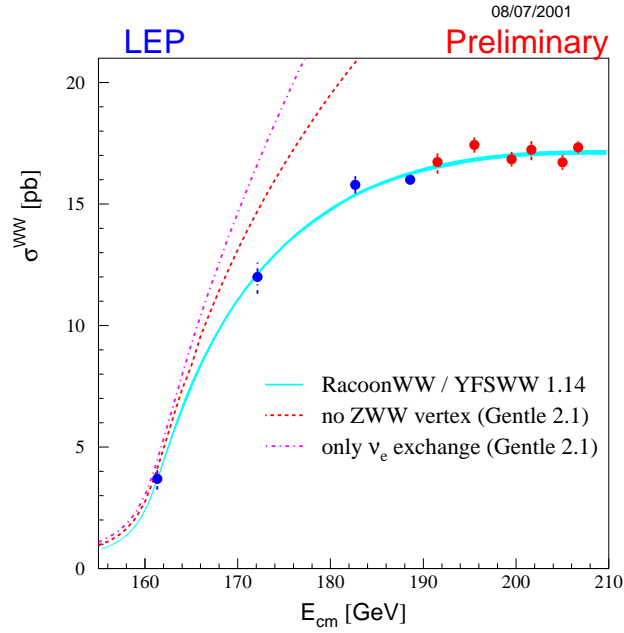


Figure 1.6: Production cross-section of W^+W^- in e^+e^- collisions measured at LEP is shown as a function of the center of mass energy, $E_{\text{cm}} = \sqrt{s}$ [1].

1.1.5 Anomalous Triple Gauge Coupling (aTGC)

As seen in the previous section, the vertex is completely determined by the electroweak gauge structure in the SM, therefore a precise measurement of the vertex is a good test for the structure of $SU(2) \times U(1)$. A di-boson process is a good probe for such test. Figure 1.7 shows $W^\pm Z$ production at the tree level, which is of particular interest in the study among the di-boson processes.

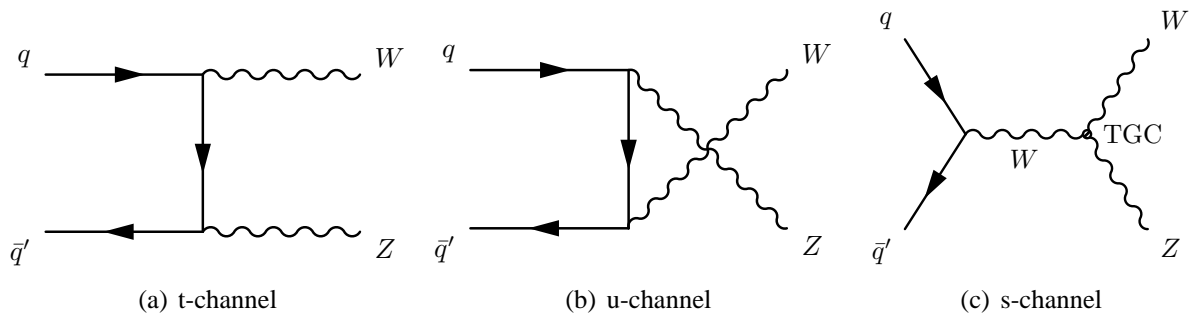


Figure 1.7: Diagrams of WZ production in hadron collisions.

To test the structure of self-coupling of bosons, it is useful to extend the SM to a more general WWZ vertex. In this way, additional coupling constants are introduced which describe possible manifestations of new physics beyond the Standard Model, and both the SM

and anomalous couplings can be measured or constrained by data. The WWZ vertex is generally parameterized in a phenomenological effective Lagrangian [33]. If only the terms which conserve charge C and parity P separately are considered, the general effective Lagrangian reduces to

$$\frac{\mathcal{L}_{WWZ}}{g_{WWZ}} = i \left[g_1^Z (W_{\mu\nu}^+ W^{-\mu} Z^\nu - W_{\mu\nu}^- W^{+\mu} Z^\nu) + \kappa^Z W_\mu^+ W_\nu^- Z^{\mu\nu} + \frac{\lambda^Z}{m_W^2} W_{\rho\mu}^+ W_\nu^{-\mu} Z^{\nu\rho} \right], \quad (1.56)$$

where $g_{WWZ} = -e \cot\theta_W$, θ_W is the weak mixing angle. $X_{\mu\nu} = \partial_\mu X_\nu - \partial_\nu X_\mu$ and g_1^Z, κ^Z , and λ^Z are the anomalous coupling parameters that will be constrained in the analysis. When $g_1^Z = 1, \kappa^Z = 1, \lambda^Z = 0$, this Lagrangian boils down to the one of SM as shown in the Equation (1.50). In the $W^\pm Z$ production g_1^Z and λ^Z are proportional to \hat{s} , whereas κ^Z is proportional to $\sqrt{\hat{s}}$, the four-momentum squared of the $W^\pm Z$ system.

Unitarity violation arises when radiative correction from this new effective Lagrangian is larger than the tree level contributions. To avoid tree level unitarity violation, the anomalous couplings must vanish as $\sqrt{\hat{s}} \rightarrow \infty$. To achieve this an arbitrary cut-off or form factor has traditionally been introduced according to

$$\alpha(\hat{s}) = \frac{\alpha_0}{\left(1 + \frac{\hat{s}}{\Lambda^2}\right)^2}, \quad (1.57)$$

where α stands for $\Delta g_1^Z, \Delta \kappa^Z$, or λ^Z , the deviations of the anomalous couplings from the SM value, and α_0 is the value of the anomalous coupling at low energy. A dipole form factor was used and Λ , the "scale of new physics", was typically chosen to be 2 TeV at the Tevatron [3] [4] and one is chosen to be infinity at the LHC.

1.1.6 Expected Cross-section of the $W^\pm Z$ Production in Proton-Proton Collisions at 7 TeV

In proton-proton high energy collisions, the scattering proceeds via partons in the protons. The cross-section $\sigma(pp \rightarrow VV')$ with $V, V' = W^\pm$ or Z or γ is schematically given by [34]

$$d\sigma = \sum_{ij} \int \int dx_1 dx_2 \times \{f_i(x_1, \mu_F) f_j(x_2, \mu_F) + f_j(x_1, \mu_F) f_i(x_2, \mu_F)\} d\hat{\sigma}_{ij}, \quad (1.58)$$

where the $f_i(j)$ is a momentum distribution functions of the partons, which are called Parton Distribution Functions (PDFs), for the i -th (j -th) parton with momentum fraction of $x_{i(j)}$ and a factorization-scale parameter μ_F , $\hat{\sigma}$ is the cross-section for the sub-process leading to the desired VV' final state. As shown in Equation (1.58), a set of PDFs is needed to predict the rates of the various processes in hadron collisions. For the $W^\pm Z$ study in the ATLAS, the CT10 [2], which is one of the PDFs sets, is employed to estimate $W^\pm Z$ events in the simulation. The PDFs of CT10 when $\mu_F = 85$ GeV are shown in Figure 1.8.

In order to calculate the Standard Model cross-section of $W^\pm Z$, the window of invariant mass of two leptons coming from the Z boson is needed to be defined since there exists the Z - γ interference. The window for the total WZ cross section σ_{WZ} in this thesis is defined as

$$66 < m_{ll} < 116 \text{ GeV} \quad (1.59)$$

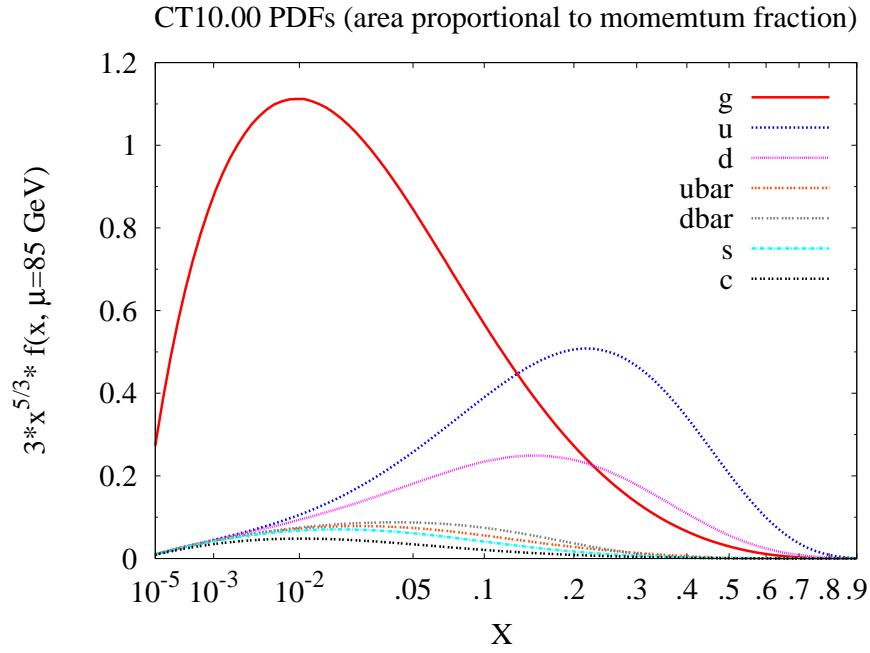


Figure 1.8: Parton distribution functions of CT10 [2].

to be consistent with the earlier ATLAS study such as the measurement of inclusive Z boson cross section [35]. Finally the cross-section in proton-proton collision at 7 TeV is calculated with the CT10 and MCFM [36], which is

$$\sigma_{W \neq Z} = 17.6_{-1.0}^{+1.1} \text{ pb.} \quad (1.60)$$

The uncertainty comes from the renormalization and factorization scales, and the PDF parametrizations.

1.2 The Motivation and Significance of This Study

Many results by the past experiments have supported the idea of the GWS theory. However, self-coupling of gauge bosons including triple gauge couplings (TGCs), which are predicted by the theory, has not yet been determined with a sufficient precision.

Di-boson processes are a good probe for the test. Anomalous TGCs are proportional to the center-of-mass-energy \hat{s} , that is why the Large Hadron Collider experiment is the most suitable one for the measurement since its \hat{s} is higher than any other past experiments. Among the di-boson processes, the $W^\pm Z$ events can be produced only by Tevatron and LHC colliders since the events can not be generated at LEP, and hence its measurement is less precise than the other processes. The $W^\pm Z \rightarrow \ell \nu \ell' \ell'$ (ℓ and ℓ' : lepton, ν : neutrino) has three high p_T leptons, therefore even in the early days of the operation and the severe environment of the hadron colliders, the events can be observed relatively efficiently in spite of the small branching ratio of leptonic decays. The CDF experiment has observed 63 candidate events of the process so far. Figure 1.9 and Table 1.4 show the limit on aTGC by the CDF and D0 experiments. At the LHC, a order of a hundred events are expected to be observed in the $\ell \nu \ell' \ell'$ channels even at the early days of the operation.

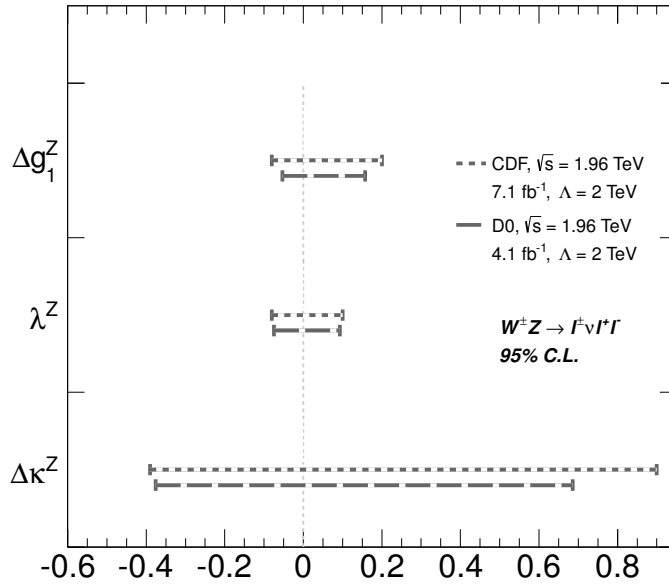


Figure 1.9: Limits on aTGC by the CDF and D0 experiments [3], [4].

Besides that, this process is a significant background to the Higgs boson [37] and charged objects coming from potential new physics such as W' boson [38] [39]. Therefore it is also important to know this process well in order to search those physics.

With the above motivations, this thesis is aiming to determine the production cross-section

	Observed 95 % Confidence Interval (C.I.) ($\Lambda = 2$ TeV)	
	CDF	D0
Δg_1^Z	[-0.08, 0.20]	[-0.056, 0.154]
$\Delta \kappa^Z$	[-0.39, 0.90]	[-0.400, 0.675]
λ^Z	[-0.08, 0.010]	[-0.077, 0.093]

Table 1.4: Observed 95 % C.I. on the aTGC by the CDF and D0 experiments.

of $W^\pm Z$ events in proton-proton collisions at 7 TeV which is the highest center-of-mass-energy ever and measure the anomalous Triple Gauge Couplings.

In this thesis, firstly some physics backgrounds for the study are presented in Chapter 1. In Chapter 2 we will see the systems of the Large Hadron Collider and the ATLAS experiment. After describing the event and object selections for the $W^\pm Z$ study in Chapter 3, how to measure the cross-section and anomalous TGCs and their results will be shown in Chapter 4 and 5. Following some discussion in Chapter 6, Chapter 7 concludes this study.

1.3 Major Contributions

The author contributed on following items.

- Made a test bench for electronics modules of the muon end-cap trigger system, which are used to keep readout information until arriving a signal that decides whether the event should be recorded or not, and tested those modules before the installation.
- Installed modules and performed commissioning with a test pulse and the cosmic rays for the muon trigger system.
- Researched and developed a new hardware logic on a new readout module which will be used at the upgraded LHC which is planned in the future.
- Contributed to establish the procedure of measurement for the muon trigger and reconstruction efficiency and evaluated the efficiency with collision data for the first time.
- Contributed to measure the $W^\pm Z$ production in proton-proton collisions at $\sqrt{s} = 7$ TeV, which is the main theme of this thesis [40].

Chapter 2

Experimental Conditions

2.1 The Large Hadron Collider

The Large Hadron Collider (LHC) was built by CERN to reveal the physics beyond the Standard Model with center-of-mass collision energies of up to 14 TeV [41]. It lies in a tunnel 27 km in circumference in the underground of the France-Swiss border near Geneva, Switzerland. The tunnel has eight straight sections and lies between 45 m and 170 m below the surface on a plane inclined at 1.4% sloping towards the lake Lemman in Geneva. Figure 2.1 shows the overview of the Large Hadron Collider [5]. The LHC is a proton-proton collider. Protons for the beams are obtained from hydrogen atoms. They are injected from the linear accelerator (LINAC2) into the PS Booster, then the Proton Synchrotron (PS), followed by the Super Proton Synchrotron (SPS), and finally the beams reach the LHC ring.

Basic concept of the LHC

The number of events per second generated in the collisions is given by

$$N_{\text{event}} = L\sigma_{\text{event}}, \quad (2.1)$$

where σ_{event} is the cross section for the event under study and L the machine luminosity. The machine luminosity depends only on the beam parameters and can be written for a Gaussian beam distribution as

$$L = \frac{N_b^2 n_b f_{\text{rev}} \gamma_r}{4\pi \varepsilon_n \beta^*} F, \quad (2.2)$$

where N_b is the number of particles per bunch, n_b the number of bunches per beam, f_{rev} the revolution frequency, γ_r the relativistic gamma factor, ε_n the normalized transverse beam emittance, β^* the beta function at the collision point, and F the geometric luminosity reduction factor due to the crossing angle at the interaction point (IP), which is given by

$$F = \left(1 + \left(\frac{\theta_c \sigma_z}{2\sigma^*}\right)^2\right)^{-1/2}, \quad (2.3)$$

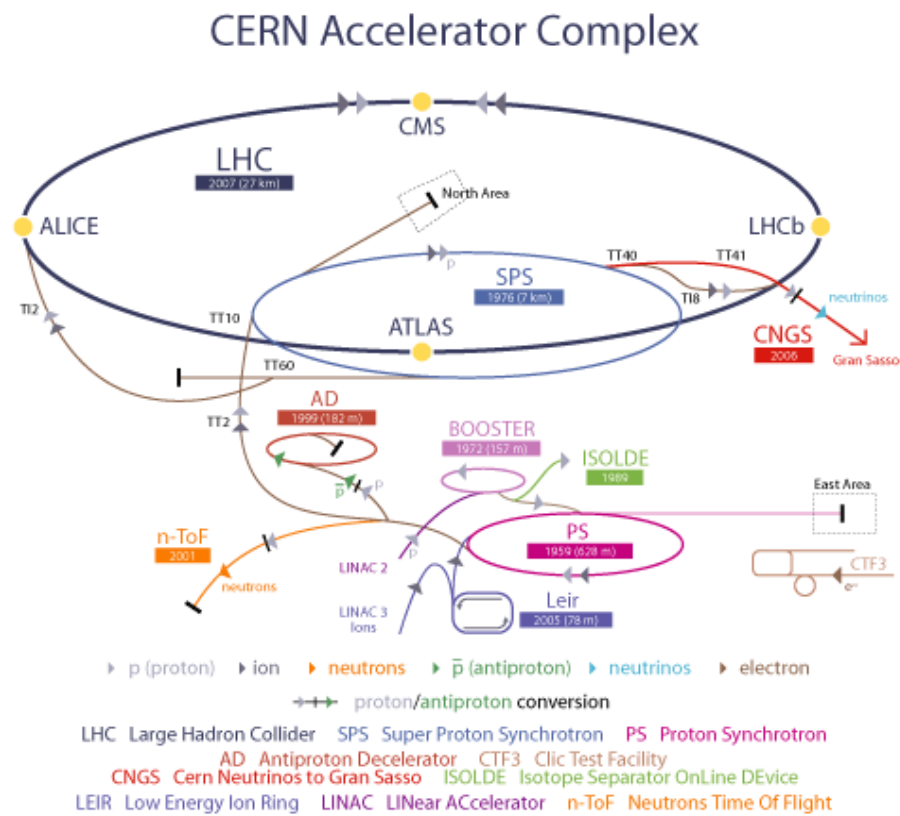


Figure 2.1: The overview of the Large Hadron Collider [5]. Protons for the beams are obtained from hydrogen atoms. They are injected from the linear accelerator (LINAC2) into the PS Booster, then the Proton Synchrotron (PS), followed by the Super Proton Synchrotron (SPS), and finally the beams reach the LHC ring.

θ_c is the full crossing angle at the IP, σ_z the RMS bunch length, and σ^* the transverse RMS beam size at the IP. The above expression assumes round beams, with $\sigma_z \ll \beta$, and with equal beam parameters for both beams.

The LHC has two high luminosity experiments, ATLAS and CMS, which are aiming at a peak luminosity of $10^{34} \text{ cm}^{-2}\text{s}^{-1}$. In order to achieve the luminosity, the LHC employed proton-proton beams instead of anti-proton-proton beams. Therefore the collider needs to have two beam channels and opposite magnetic dipole fields for counter-rotating. Considering the requirement and the restricted space in the tunnel, the LHC chose to use twin bore magnets that consist of two sets of coils and beam channels within the same mechanical structure and cryostat. The cross section of the LHC beam pipe is shown in Figure 2.2.

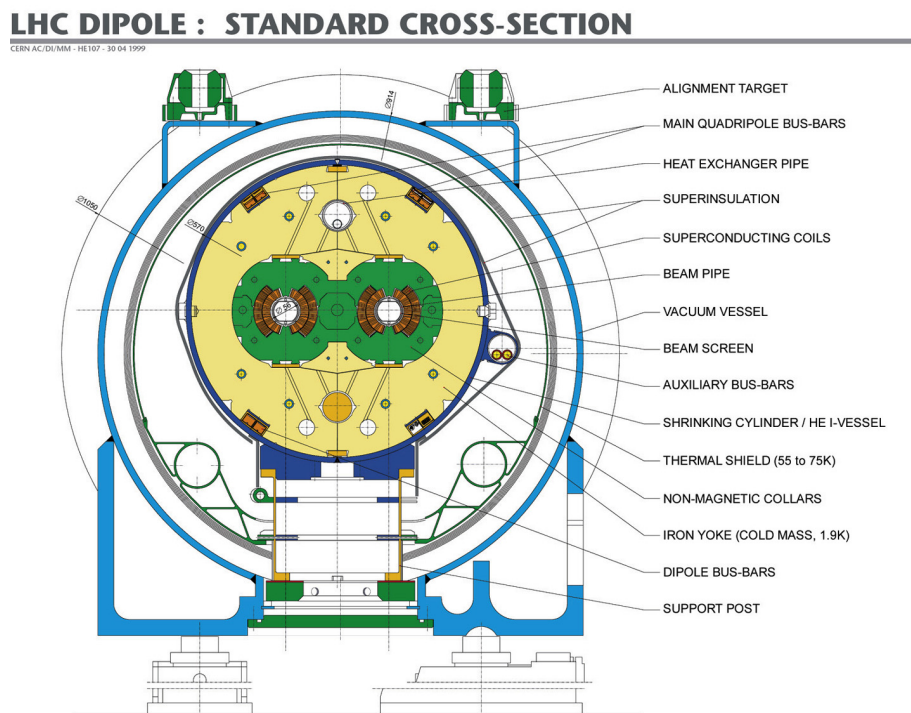


Figure 2.2: Cross section of the LHC two-in-one dipole magnet [6].

Performance goals and the one in 2011

The LHC started the operation at the end of 2009, and since then its performance has been improving towards the aiming performance. The design parameters and the ones achieved in 2011 are shown in Table 2.1.

LHC parameter	Design	2011
Proton energy [TeV]	7.0	3.5
Center-of-mass energy [TeV]	14.0	7.0
Protons per bunch N_b	1.15×10^{11}	1.2×10^{11}
Bunch spacing [ns]	25	75 (until March), 50
Maximum number of bunches per beam n_b	2808	1331
Optimal β -function β^* [m]	0.55	1.5 (until August), 1.0
Mean number of interactions per crossing	~ 20	6.3 ($\beta^* = 1.5$ m), 11.6 ($\beta^* = 1.0$ m)
Peak luminosity [$\text{cm}^{-1}\text{s}^{-1}$]	1.0×10^{34}	3.6×10^{33}

Table 2.1: The design parameters of the LHC and the ones in 2011 [26] [27].

2.2 The ATLAS Experiment

This section describes the ATLAS experiment system. In order to achieve the physics goals in the severe experiment environment of the LHC, below items are required for the LHC detectors.

- The electronics and sensors of the detectors must be fast and radiation-hard.
- The detector granularity has to be high to handle the high particle fluxes and to reduce the influence of overlapping events.
- Acceptance in pseudorapidity and azimuthal angle coverage should be as large as possible.
- In order to be an acceptable trigger rate, efficient triggering system is required even for the low transverse-momentum.

Following sections clear up how the ATLAS detector achieves these requirements.

2.3 The ATLAS Detector

2.3.1 Coordinate System of the ATLAS

The coordinate system and nomenclature used to describe the ATLAS detector are mentioned here. Figure 2.3 shows them. The nominal interaction point is defined as the origin of the coordinate system. The beam direction defines the z-axis and the x-y plane is transverse to the beam direction. While the positive x-axis is defined as pointing from the interaction point to the center of the LHC ring, the positive y-axis is defined as pointing upwards. The detector can be distinguished into two sides, as the plane where z is zero is the boarder plane. The side of positive z is defined as the side-A (Mt. Jura side) and the one of negative z is defined as the side-C (Geneva side). The polar angle θ is the angle from the beam axis. The pseudorapidity is defined as $\eta = -\ln \tan(\theta/2)$. The transverse momentum p_T , the transverse energy E_T , and the missing transverse energy E_T^{miss} are defined in the x-y plane. The distance ΔR in the pseudorapidity-azimuthal angle space is defined as $\Delta R = \sqrt{\Delta\eta^2 + \Delta\phi^2}$.

2.3.2 Overview of the ATLAS Detector

The overall ATLAS detector layout is shown in Figure 2.4 and its designed performance are listed in Table 2.2.

The ATLAS detector is nominally forward-backward symmetric with respect to the interaction point. The innermost part of the detector is a precision tracking system covering the pseudorapidity range $|\eta| < 2.5$. It consists of silicon pixels, silicon strips, and straw-tube chambers operating in a 2 T axial magnetic field supplied by a superconducting solenoid. Outside the solenoid are highly segmented electromagnetic and hadronic calorimeters covering $|\eta| < 4.9$. The outermost subsystem is a large muon spectrometer covering $|\eta| < 2.7$, which reconstructs muon tracks and measures their momenta using the azimuthal magnetic field produced by three sets of air-core superconducting toroids.

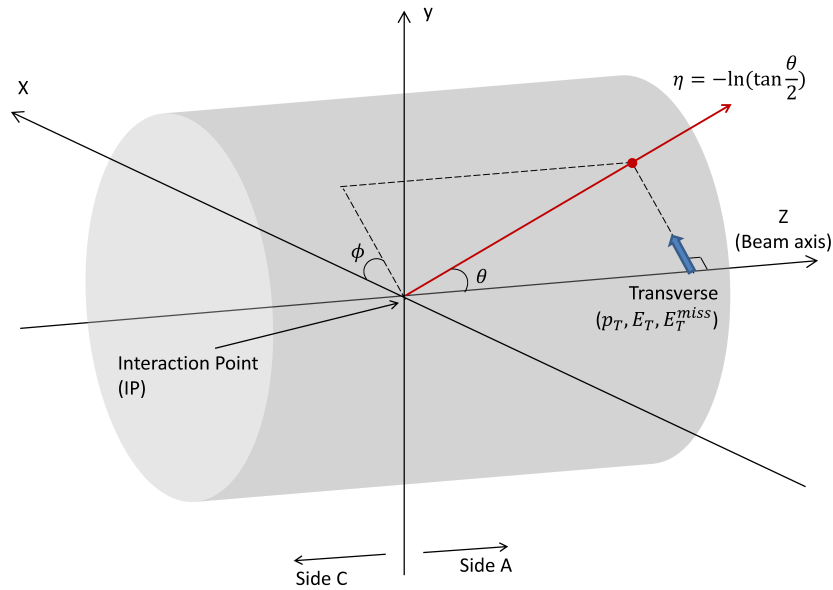


Figure 2.3: Coordinate System. The beam direction defines the z -axis and the x - y plane is transverse to the beam direction. The positive x -axis is defined as pointing from the interaction point to the center of the LHC ring and the positive y -axis is defined as pointing upwards. The detector can be distinguished into two sides, as the plane where z is zero is the boarder plane. The side of positive z is defined as the side-A and the one of negative z is defined as the side-C.

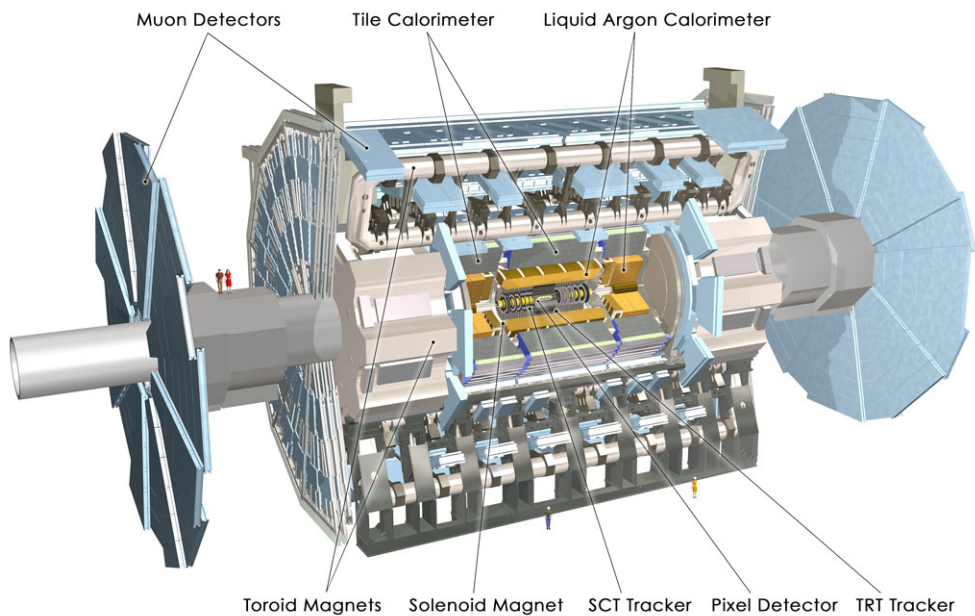


Figure 2.4: Cut-away view of the ATLAS detector [7].

This analysis primarily uses the inner detector and the electromagnetic calorimeter to reconstruct electrons, the inner detector and the muon spectrometer to reconstruct muons, and the electromagnetic and hadronic calorimeters to reconstruct the missing momentum transverse to the beam line, E_T^{miss} .

Detector component	Required resolution	η coverage	
		Measurement	Trigger
Tracking	$\sigma_{p_T}/p_T = 0.05\% \ p_T \oplus 1\%$	± 2.5	
EM calorimetry	$\sigma_E/E = 10\% \ \sqrt{E} \oplus 0.7\%$	± 3.2	± 2.5
Hadronic calorimetry (jets)	$\sigma_E/E = 50\% \ \sqrt{E} \oplus 3\%$	± 3.2	± 3.2
	$\sigma_E/E = 100\% \ \sqrt{E} \oplus 10\%$	$3.1 < \eta < 4.9$	$3.1 < \eta < 4.9$
Muon spectrometer	$\sigma_{p_T}/p_T = 10\%$ at $p_T = 1 \text{ TeV}$	± 2.7	± 2.4

Table 2.2: Designed Performance

2.3.3 Inner Detector

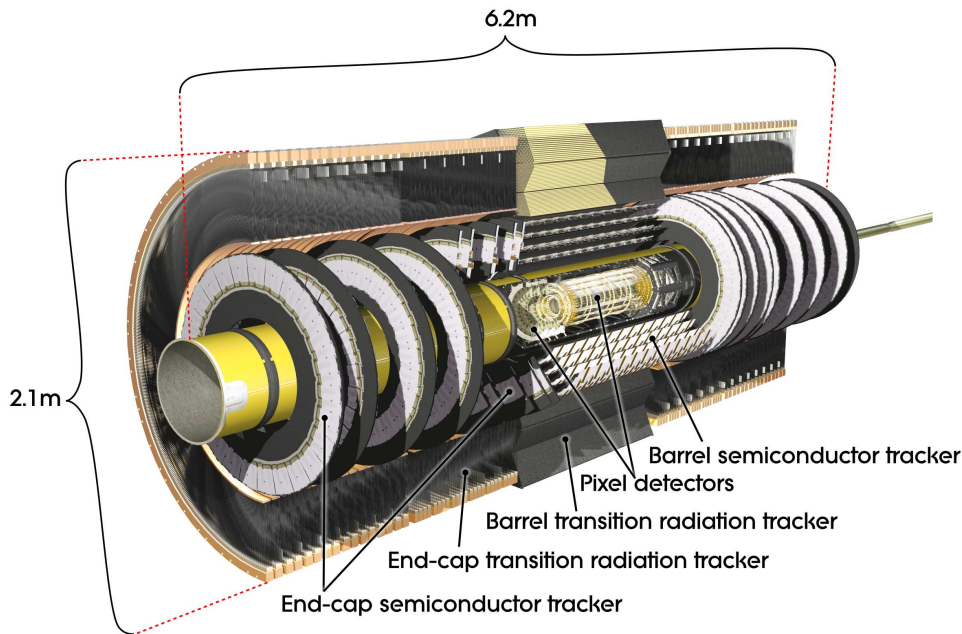


Figure 2.5: A cut-away view of the Inner detector (ID) [7].

The ATLAS Inner Detector (ID) is designed to provide robust pattern recognition, excellent momentum resolution and vertex measurements for charged tracks within the pseudorapidity range $|\eta| < 2.5$. It also provides electron identification over $|\eta| < 2.0$ within a wide range of

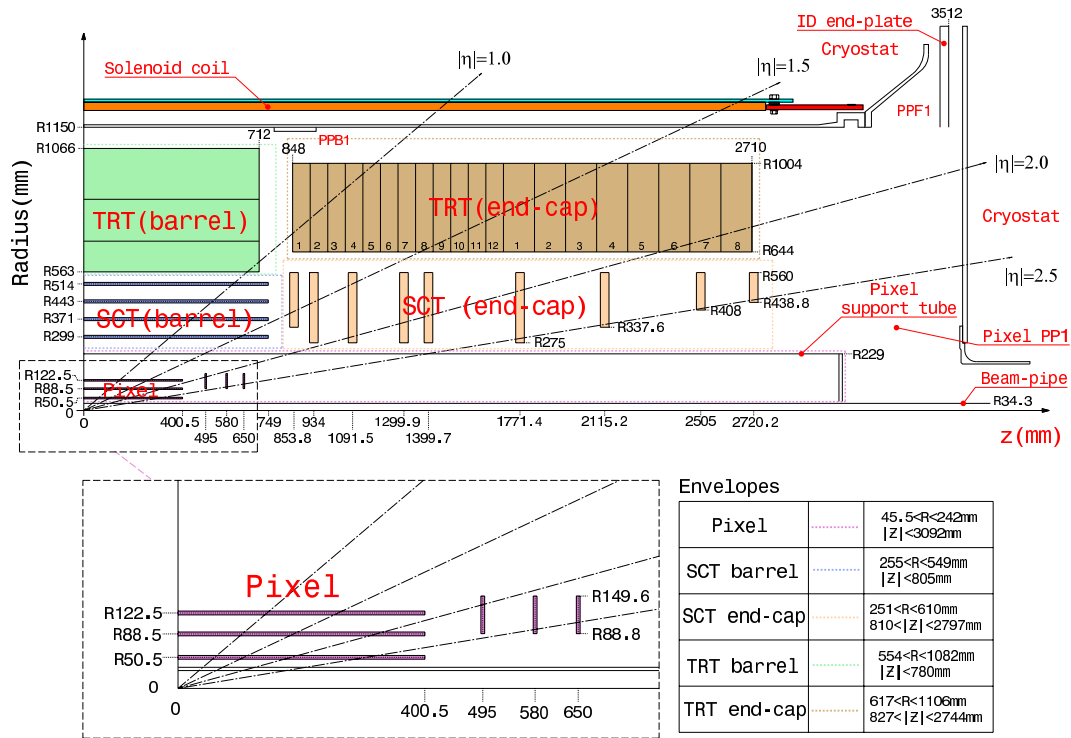


Figure 2.6: A detailed configuration of the ATLAS Inner Detectors [8].

energies between 0.5 GeV and 150 GeV. The overview of ID is shown in Figure 2.5 and the cross-section in the R-z plane is shown in Figure 2.6.

The ID is contained within a cylindrical envelope of length ± 3512 mm and of radius 1150 mm. It is installed in a solenoidal magnetic field of 2 T and consists of three independent but complementary sub-detectors, which are the Pixel detector, the Semi-Conductor Tracker (SCT) detector and the Transition Radiation Tracker (TRT).

Pixel and SCT Detectors (Silicon Detector)

The Pixel detector is located at the innermost part of the ID and the SCT is installed outside the Pixel. The Pixel and SCT are collectively called the Silicon detector. While they are arranged on cylinders around the beam pipe in the barrel region, they are located on disks perpendicular to the pipe in the end-cap region.

The Pixel has three layers in both barrel and end-cap region. The innermost layer in the barrel is called b-layer, which is located at the radius of 51 mm from the beam line. The thickness of modules is $250 \mu\text{m}$. All pixel modules are identical and minimum pixel size on a sensor is $50 \times 400 \mu\text{m}^2$. They are operated at 150 V and which can be up to 600 V depending on the sensor position and the integrated luminosity for good charge collection efficiency after ten years operation. The Pixel achieves high-resolution pattern recognition capabilities by using discrete space-points. While barrel modules measure the ϕ and z positions of tracks, end-cap modules measure the ϕ and R positions. The intrinsic spacial resolution in the end-cap is $10 \mu\text{m}$

for ϕ and $115 \mu\text{m}$ for z , the one in the barrel is $10 \mu\text{m}$ for ϕ and $115 \mu\text{m}$ for R .

The SCT consists of stereo pairs of silicon microstrip layers. In the barrel region, the SCT has four cylindrical layers and uses small angle of 40 mrad stereo strips with a pitch of $80 \mu\text{m}$ to measure not only R - ϕ position but also z position. In the end-cap region, there are nine disks at each side, and a set of stereo strips runs at angle of 40 mrad in addition to a set of strips running radially from the beam axis. As with the barrel, the mean pitch of the strips are also $80 \mu\text{m}$. While the intrinsic accuracies per module in the barrel are $17 \mu\text{m}$ for R - ϕ and $580 \mu\text{m}$ for z , the ones in the end-cap are $17 \mu\text{m}$ for R - ϕ and $580 \mu\text{m}$ for R .

TRT Straw Tubes

The TRT is located at the outermost part, which comprises many layers of gaseous straw tube elements interleaved with radiators consisting of polypropylene foils or fibers. The straw tubes of 4 mm diameter are 144 cm long in the barrel region whereas the one in the end-cap region is 37 cm . They are arranged in parallel to the beam axis in the barrel region and are arranged radially in wheels in the end-cap region. For both the barrel and end-cap straws, the anodes are $31 \mu\text{m}$ diameter tungsten (99.95%) wires plated with 0.5 - $0.7 \mu\text{m}$ gold, the cathodes are operated typically at $.1530 \text{ V}$ to give a gain of 2.5×10^4 for the chosen gas mixture of $70\% \text{ Xe}$, $27\% \text{ CO}_2$ and $3\% \text{ O}_2$ with 5 - 10 mbar over-pressure. The TRT provides continuous tracking with those tubes and improves the momentum resolution over $|\eta| < 2.0$. In addition to the tracking capabilities, the TRT provides electron identification by detecting the transition radiation photons emitted in the fiber or foils interleaved between the straws. While only the R - ϕ information is provided in the barrel only the R - z information is provided in the end-cap. The intrinsic accuracy per straw is $130 \mu\text{m}$.

The harsh environment and the pile-up from multiple interactions per bunch crossing require a high detector granularity. The overall weight and material budget of the ID (in terms of radiation length X_0 and interaction length λ) are therefore large. Figure 2.7 shows the integrated radiation length, X_0 , and interaction length λ , traversed by a straight track as a function of $|\eta|$ at the exit of the ID envelope.

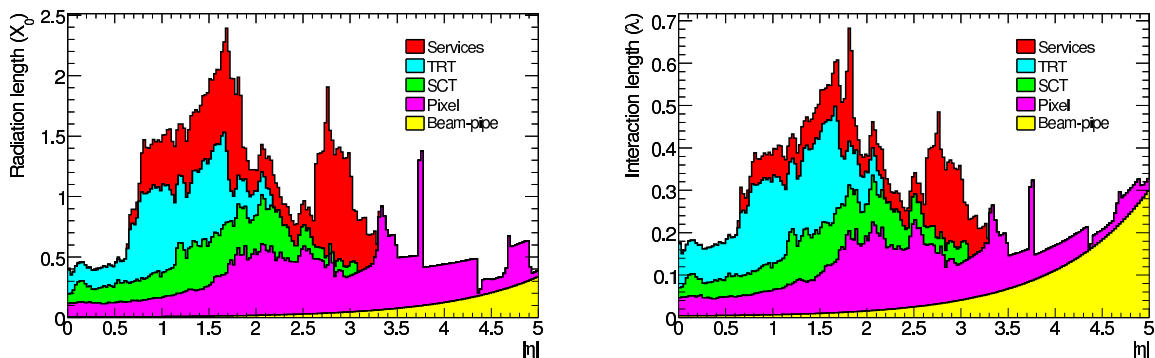


Figure 2.7: Material distribution in the inner detector as a function of $|\eta|$ [8].

As a result of the large material distribution, below issues arise [42]:

- Many electrons lose energy through bremsstrahlung before reaching the electromagnetic calorimeter.
- Considerable photons convert into an electron-positron pair before reaching the cryostat of the liquid Argon (LAr) and the electromagnetic calorimeter.
- A significant fraction of charged pions undergoes an inelastic hadronic interaction inside the inner detector volume.

To reduce these effects, energy information of particles measured by the calorimeter is used and cuts on impact parameters are applied in the analysis. More details are in the Section 2.5.3 and 3.2.2.

2.3.4 Calorimeter

The ATLAS calorimeters consist of a number of sampling detectors with full ϕ -symmetry and coverage around the beam axis and cover the range $|\eta| < 4.9$. Figure 2.8 shows a cut-away view of the calorimeters and the pseudorapidity coverage and granularity are summarized in Table 2.3.

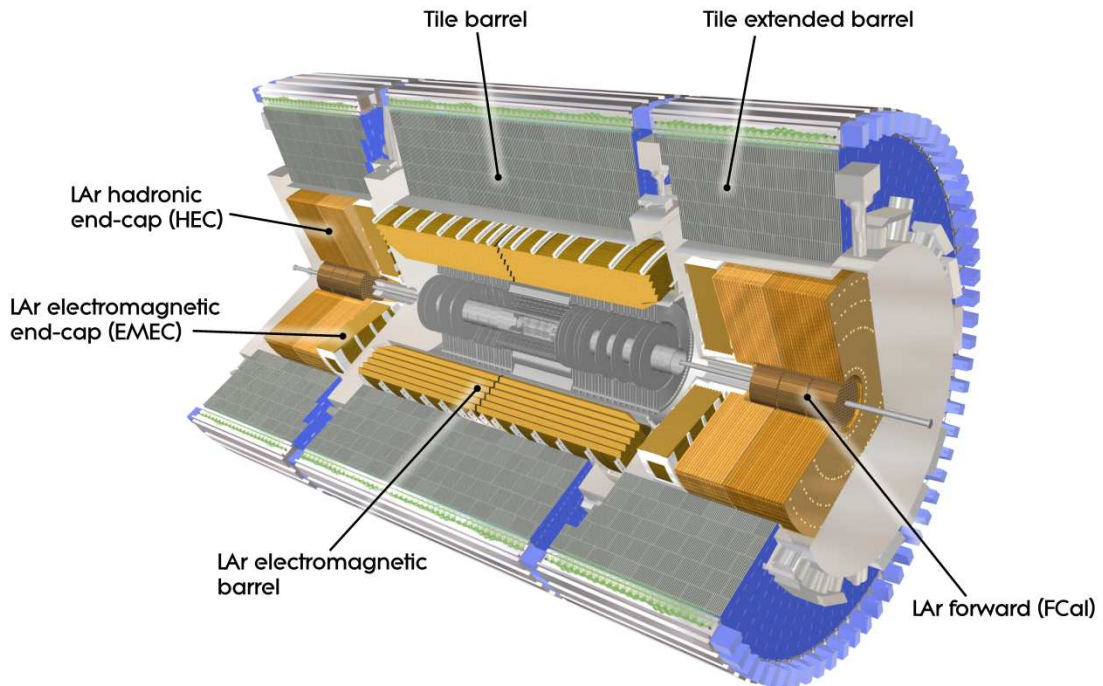


Figure 2.8: A cutaway view of the ATLAS Calorimeters [7].

The calorimeters closest to the beam-line are housed in three cryostats, one barrel and two end-caps. While the barrel cryostat contains the electromagnetic barrel calorimeter, the

end-cap cryostat contains an electromagnetic end-cap calorimeter (EMEC), a hadronic end-cap calorimeter (HEC) located behind the EMEC and forward calorimeter (FCal) to cover the region closest to the beam. The FCal is further split into one electromagnetic module (FCal1) and two hadronic modules (FCal2 and FCal3) as shown in Figure 2.9. All these calorimeters use liquid argon as the active detector medium. The liquid argon has been chosen for its intrinsic linear behavior, its stability of response over the time and its intrinsic radiation-hardness.

For the outer hadronic calorimeter, the sampling medium consists of scintillator tiles and the absorber medium is steel. The tile calorimeter is composed of three parts, one central barrel and two extended barrels. The choice of this technology provides maximum radial depth for the least cost for ATLAS.

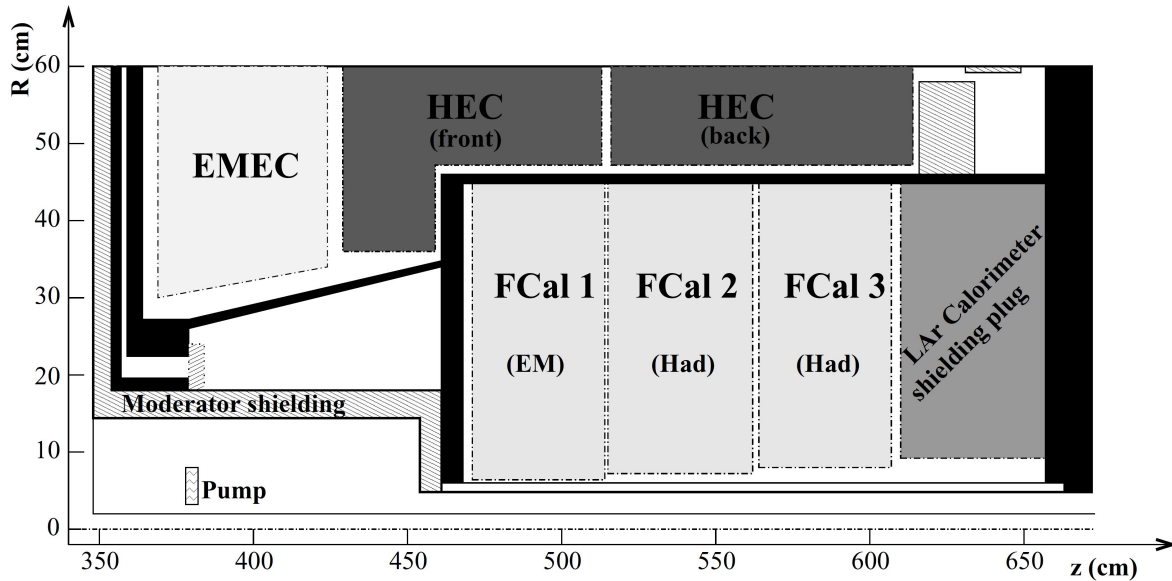


Figure 2.9: The layout of the calorimeters in the endcap and forward region. All the calorimeters are housed in the same cryostat [9].

Electromagnetic Calorimeter

The precision electromagnetic calorimeters are lead-liquid argon detectors with accordion-shape absorbers and electrodes. The geometry provides naturally a full coverage in ϕ without any cracks, and a fast extraction of the signal at the rear or at the front of the electrodes. The electromagnetic barrel calorimeter covers the region at $0 < |\eta| < 1.475$ and the EMEC covers $1.375 < |\eta| < 3.2$. In the barrel, the accordion waves are axial and run in ϕ , and the folding angles of the waves vary with radius to keep the liquid-argon gap constant. A module in the barrel is shown in Figure 2.10. It has three layers. The readout granularity of the different layers is shown in Table 2.3. In the end-caps, the waves are parallel to the radial direction and run axially. The absorbers are made of lead plates and the thickness is 1.53 mm for $|\eta| < 0.8$ and 1.13 mm for $|\eta| > 0.8$. The change in lead thickness at $|\eta| = 0.8$ limits the decrease of the sampling fraction as $|\eta|$ increases.

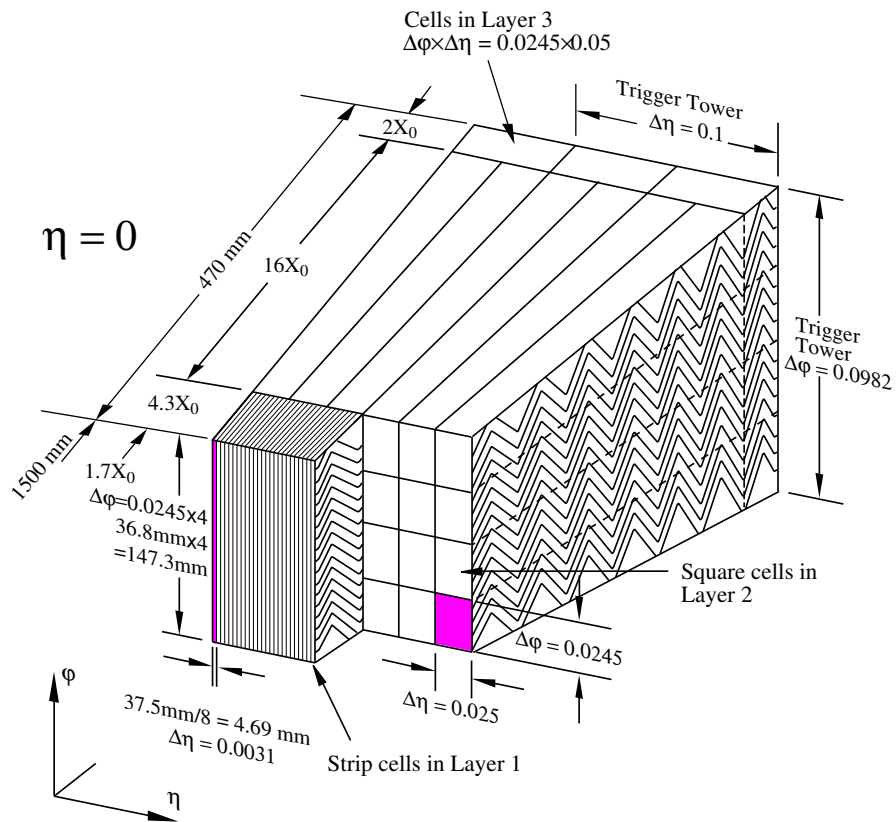


Figure 2.10: Sketch of a barrel LAr Calorimeter module [9].

The EM calorimeter has a fine segmentation in both the lateral ($\eta \times \phi$ space) and longitudinal directions of the shower. At high energy, most of the shower energy is collected in the second layer which has a lateral granularity of 0.025×0.025 in $\eta \times \phi$ space. The first layer consists of finer-grained strips in the η direction (with a coarser granularity in ϕ), which offer excellent γ - π^0 discrimination. These two layers are complemented by a presampler layer placed in front in the region ($0 < |\eta| < 1.8$) with coarse granularity to correct for energy lost in the material before the calorimeter, and by a third EM layer, which enables a correction to be made for the tail for very highly energetic EM showers.

The calorimeter system also has electromagnetic coverage at higher η ($3.1 < |\eta| < 4.9$) provided by the FCal1. To optimize the resolution and the heat removal, copper was chosen as the absorber for FCal1.

Hadronic calorimeter

The hadronic calorimetry is covered by the tile calorimeter in the range $0 < |\eta| < 1.7$, the HEC in the range $1.5 < |\eta| < 3.2$ and the FCal in the range $3.1 < |\eta| < 4.9$.

The tile calorimeter located behind the liquid argon electromagnetic calorimeter is subdivided into a central barrel and two extended barrels. The central barrel is 5.8 m and two extended barrels are 2.6 m in length and each has an inner radius of 2.28 m and an outer radius of 4.25 m. The tile calorimeter is a sampling calorimeter using steel as the absorber and scintillator as the active medium. The structure is sketched in Figure 2.11.

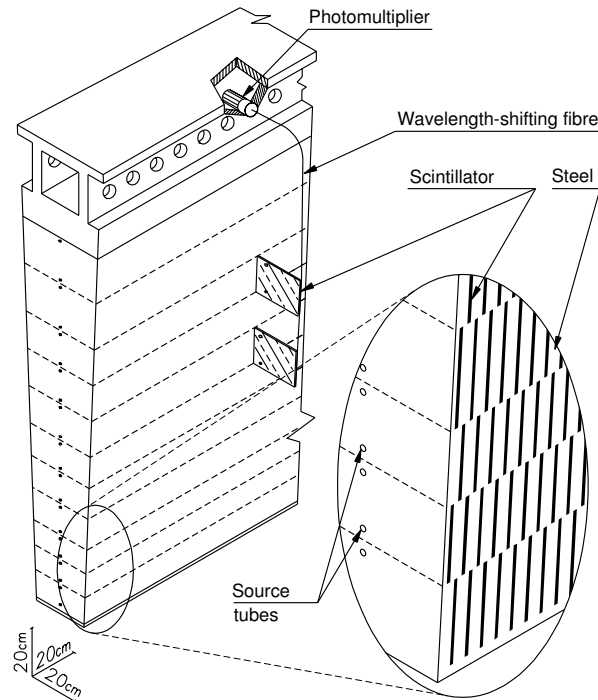


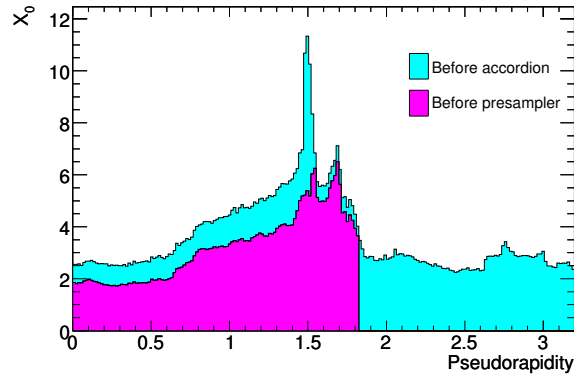
Figure 2.11: A schematic view of a scintillator tile calorimeter module [9].

The HEC is a copper/liquid-argon sampling calorimeter with a flat-plate design, which cov-

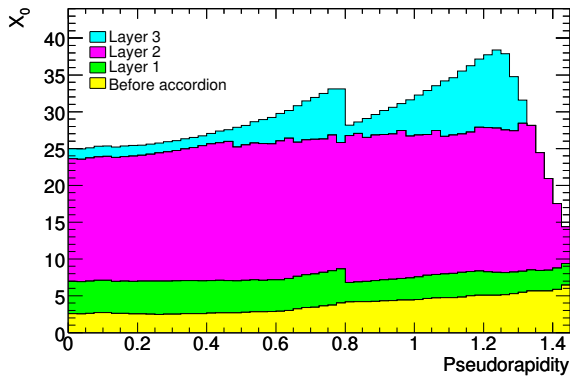
ers the range $1.5 < |\eta| < 3.2$ and shares each of the two liquid-argon end-cap cryostats with the EMEC and FCal. The HEC consists of two wheels in each end-cap cryostat, a front wheel is called HEC1 and a rear wheel is called HEC2. The wheels are cylindrical with an outer radius of 2030 mm. The size of readout cells is $\Delta\eta \times \Delta\phi = 0.1 \times 0.1$ in the region $1.5 < |\eta| < 2.5$ and 0.2×0.2 in the region $1.5 < |\eta| < 3.2$.

The FCal is located in the same cryostats as the end-cap calorimeters and covers $3.1 < |\eta| < 4.9$. In order to minimize energy losses in cracks between the calorimeter systems and also limit the backgrounds which reach the muon system, the structure is quite hermetic. As the FCal modules are located at high η at a distance of approximately 4.7 m from the interaction point, they are exposed to high particle fluxes. This requires its design to have small liquid-argon gaps. To provide containment and minimize the lateral spread of hadronic showers, tungsten was used as the absorber in FCal2 and FCal3.

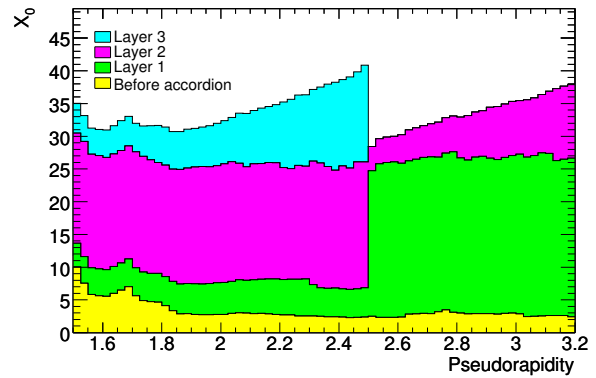
Calorimeters must detect electromagnetic and hadronic showers with little leakage to provide a good resolution, and must also limit punch-through into the muon system. Therefore the depth of the calorimeter is important. The total thickness of the EM calorimeter is greater than 22 in radiation lengths (X_0) in the barrel region, whereas the one in the end-caps is greater than 24 X_0 . For the interaction lengths (λ), it is approximate 9.7 λ of active calorimeter in the barrel and 10 λ in the end-caps. The numbers of radiation and interaction length in front of and in the electromagnetic and hadronic calorimeters are shown in Figure 2.12 and 2.13.



(a)



(b)



(c)

Figure 2.12: Cumulative amounts of material in units of X_0 (radiation length) and as a function of $|\eta|$ in front of and in the EM calorimeters. (a) The total amount of material in front of the presampler layer and in front of the first layer of the EM calorimeters over the full η range. (b) The thickness of each layer as well as the material in front of the first layer in the barrel. (c) The thickness of each layer as well as the material in front of the first layer in the endcap [9].

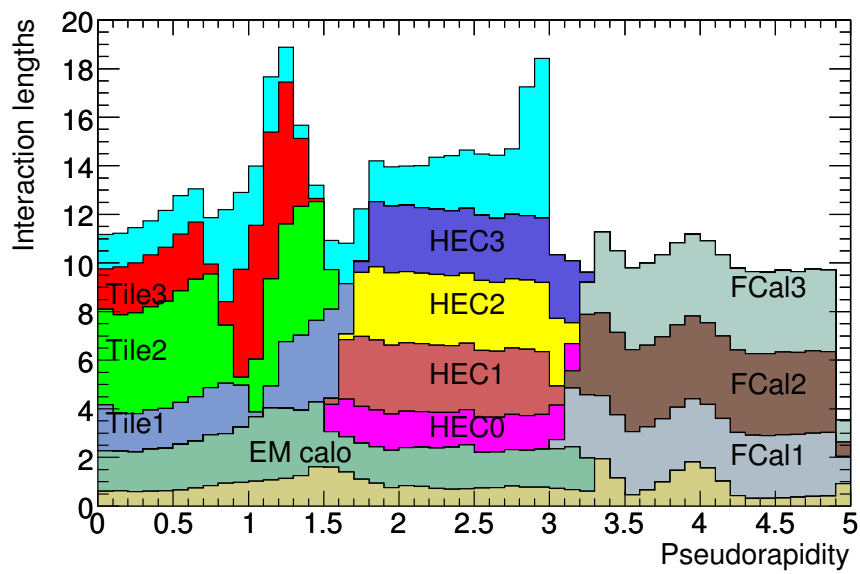


Figure 2.13: Cumulative amount of material in units of λ (interaction length) as a function of $|\eta|$ in front of and in the EM calorimeters, in each hadronic layer, the total amount at the end of the active calorimetry and the total amount of material in front of the first active layer of the muon spectrometer [9].

	Barrel	End-cap
EM calorimeter		
Granularity $\Delta\eta \times \Delta\phi$ versus $ \eta $		
Presampler	0.025×0.1 ($ \eta < 1.52$)	0.025×0.1 ($1.5 < \eta < 1.8$)
Calorimeter 1st layer	$0.025/8 \times 0.1$ ($ \eta < 1.40$)	0.050×0.1 ($1.375 < \eta < 1.425$)
	0.025×0.025 ($1.40 < \eta < 1.475$)	0.025×0.1 ($1.425 < \eta < 1.5$)
		$0.025/8 \times 0.1$ ($1.5 < \eta < 1.8$)
		$0.025/6 \times 0.1$ ($1.8 < \eta < 2.0$)
		$0.025/4 \times 0.1$ ($2.0 < \eta < 2.4$)
		0.025×0.1 ($2.4 < \eta < 2.5$)
Calorimeter 2nd layer	0.025×0.025 ($ \eta < 1.40$)	0.050×0.025 ($1.375 < \eta < 1.425$)
	0.025×0.025 ($1.40 < \eta < 1.475$)	0.025×0.025 ($1.425 < \eta < 2.5$)
		0.1×0.1 ($2.5 < \eta < 3.2$)
Calorimeter 3rd layer	0.050×0.050 ($ \eta < 1.35$)	0.050×0.025 ($1.5 < \eta < 2.5$)
LAr hadronic end-cap		
Granularity $\Delta\eta \times \Delta\phi$ versus $ \eta $		
HEC		0.1×0.1 ($1.5 < \eta < 2.5$)
		0.2×0.2 ($2.5 < \eta < 3.2$)
LAr forward calorimeter		
Granularity $\Delta\eta \times \Delta\phi$ versus $ \eta $		
FCal1 (EM)		3.0×2.6 ($3.15 < \eta < 4.30$) ~ four times finer ($3.10 < \eta < 3.15$), ($4.30 < \eta < 4.83$)
		3.3×4.2 ($3.24 < \eta < 4.50$) ~ four times finer ($3.20 < \eta < 3.24$), ($4.50 < \eta < 4.81$)
FCal2 (Hadronic)		5.4×4.7 ($3.32 < \eta < 4.60$) ~ four times finer ($3.29 < \eta < 3.32$), ($4.60 < \eta < 4.75$)
FCal3 (Hadronic)		
Scintillator tile calorimeter		
Granularity $\Delta\eta \times \Delta\phi$ versus $ \eta $		
Tile	0.1×0.1 ($ \eta < 1.0$)	0.1×0.1 ($0.8 < \eta < 1.7$)

Table 2.3: Granularity of the calorimeter

2.3.5 Muon Spectrometer

The muon spectrometer is located at the outer part of the ATLAS detector. It is designed to detect charged particles exiting the calorimeters and to measure their momentum in the pseudorapidity range $|\eta| < 2.7$. It is also designed to trigger on these particles in the region $|\eta| < 2.4$. The precision momentum measurement is performed by the Monitored Drift Tube chambers (MDTs) and Cathode-Strip Chambers (CSC). The MDT covers the range $|\eta| < 2.7$ except the innermost end-cap layer over the range $|\eta| > 2.0$ where CSC covers instead. The performance goal is a stand-alone transverse momentum resolution of approximately 10 % for 1 TeV tracks, which translates into a sagitta of about $500 \mu\text{m}$ needs to be measured with a resolution of $\leq 50 \mu\text{m}$.

The MDT and CSC are complemented by a system of fast trigger chambers. As the trigger chambers, Resistive Plate Chambers (RPC) covers the barrel region $|\eta| < 1.05$, Thin Gap Chambers (TGC) covers the end-cap region ($1.05 < |\eta| < 2.4$). The cross-section of the muon system is shown in Figure 2.14 and 2.15.

Both in the end-cap and barrel, there are three MDT stations. In the end-cap, the first TGC layer is located in front of the innermost MDT layer at $z \simeq 7$ m, the other three TGC layers stand in front and behind the second MDT wheel at $z \simeq 13$ m. In the barrel, the second MDT station is located between the first and second RPC layers and the third MDT layer stands in front of the third RPC layer.

Figure 2.16 shows their locations in η - ϕ space. In each of these the muon will traverse a particular set of detector layers. The ten regions are labelled and described below:

- barrel large: large barrel stations;
- barrel small: small barrel stations;
- barrel overlap: overlap between small and large barrel stations;
- feet: region of the feet supporting the detector; some chambers are missing in this region which makes the muon reconstruction more difficult;
- transition: transition region between the barrel part and the endcap wheels;
- endcap small: small endcap sectors, MDT chambers;
- endcap large: large endcap sectors, MDT chambers;
- BEE: sectors containing barrel extended endcap chambers;
- CSC small: small endcap sectors, CSC chambers, outside TRT acceptance;
- CSC large: large endcap sectors, CSC chambers, outside TRT acceptance.

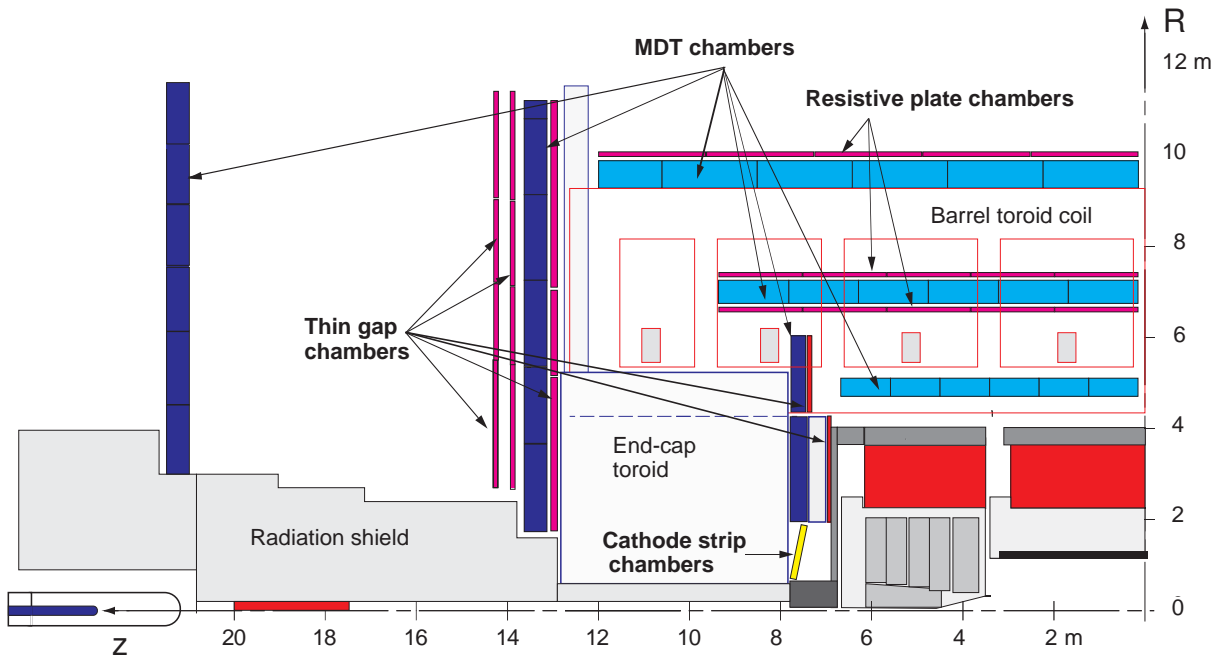


Figure 2.14: A schematic R-z view of the ATLAS muon spectrometer [10].

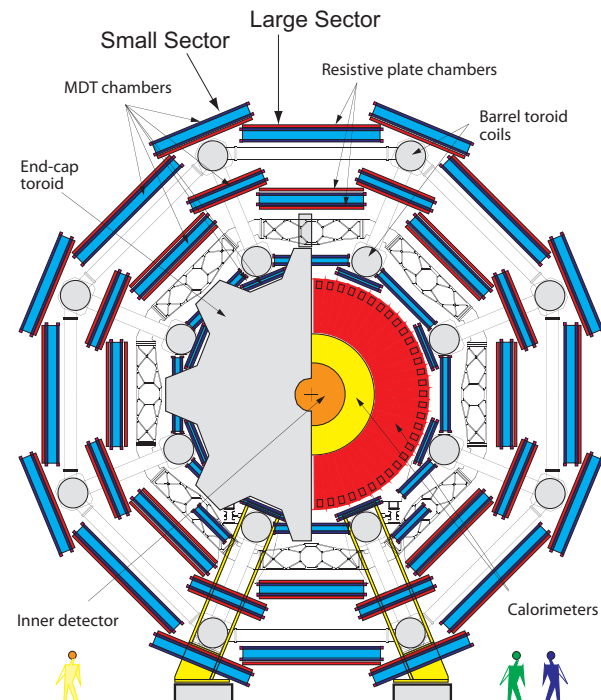


Figure 2.15: A schematic R- ϕ view of the ATLAS muon spectrometer [11].

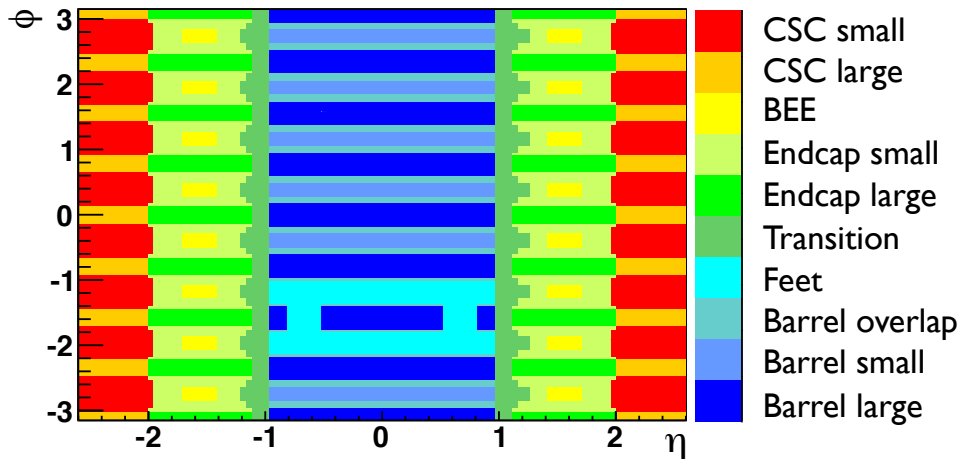


Figure 2.16: η - ϕ map of the coverage of the ten detector regions [12].

MDT

The basic element of MDT chambers is a pressurized drift tube with a diameter of 29.970 mm, which is generated with Ar/CO₂ gas (ratio: 93% / 7%) at 3 bar. The electrons which are generated by ionization are collected at the central tungsten-rhenium wire with a diameter of 50 μ m at a potential of 3080 V. A schematic drift tube of the MDT is shown in Figure 2.17. The maximum drift time of the tube from the wall to the wire is about 700 ns. A track passing close to the wire thus generates a pulse train with a duration of this order. To prevent an inflation of the data volume by multiple track hits, an adjustable dead-time has been implemented in the front-end of the readout chain.

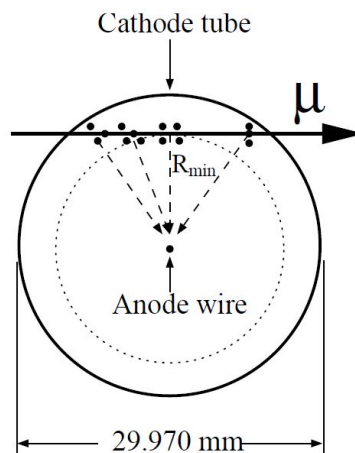


Figure 2.17: A drift tube of the MDT [13].

All regular MDT chambers consist of two groups of tube layers, called multi-layers, separated by a mechanical spacer. In the innermost layer of the muon detector, each multi-layer consists of four tube layers to enhance the pattern-recognition performance, while each multi-

layer consists of three tube layers in the middle and outer station of the muon spectrometer. Figure 2.18 and 2.19 show the structure of a barrel chamber and an end-cap chamber, respectively.

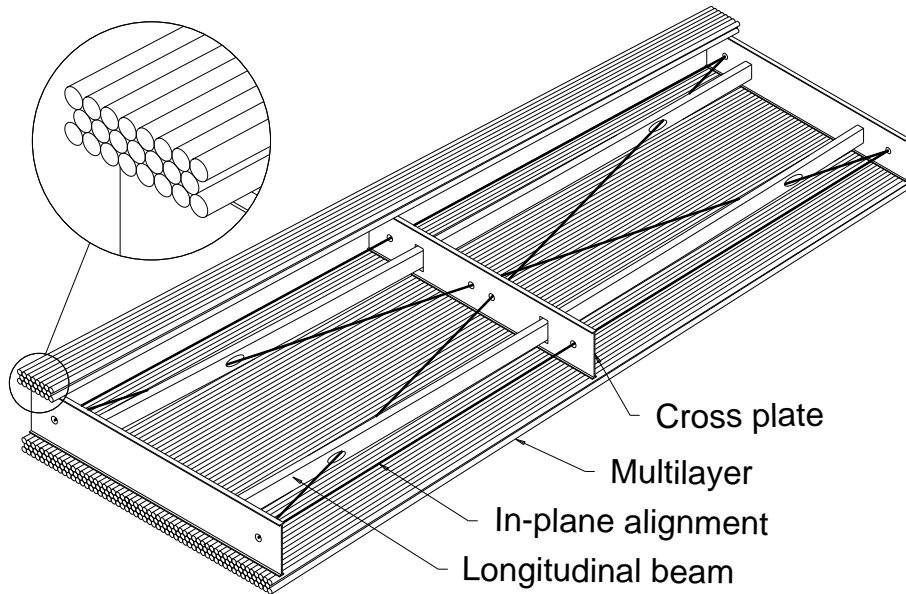


Figure 2.18: A schematic view of a barrel MDT chamber [13].

As shown in Figure 2.20, the chamber alignment of muon spectrometer is crucial for the momentum resolution at high p_T region where p_T is greater than a few hundreds GeV. In order to achieve the required momentum resolution at high p_T region, every tube was carefully constructed and was arranged in a frame with an adequate accuracy. In addition to that, an internal chamber alignment system was implemented, which continuously monitors potential deformations of the frame. The alignment system consists of a set of four optical alignment rays as shown in Figure 2.18 and Figure 2.19.

Due to the tight construction tolerances and to the continued monitoring of global chamber deformations, the relative positions of MDT wires are sufficiently well known for the accuracy of a track segment in the tube layers to be limited only by the single-tube resolution (about $80 \mu\text{m}$). Therefore, the resolution on the central point of a track segment in a 3- or 4-tube multilayer is $50 \mu\text{m}$ and $40 \mu\text{m}$, respectively, and combining the two multi-layers into a chamber yields an accuracy of $35 \mu\text{m}$ and $30 \mu\text{m}$, respectively.

CSC

The limit for safe operation of the MDTs is at counting rates of about 150 Hz/cm^2 , which will be exceeded in the region $|\eta| > 2$ in the first layer of the end-cap. The CSCs that are multiwire proportional chambers with the wires oriented in the radial direction as shown in Figure 2.21(b) are employed in the region instead. The detector combines high spatial, time and double track resolution with high-rate capability and low neutron sensitivity. It operates with Ar/CO₂ gas (ratio: 80% / 20%) at a potential of 1900 V. A schematic view of the whole

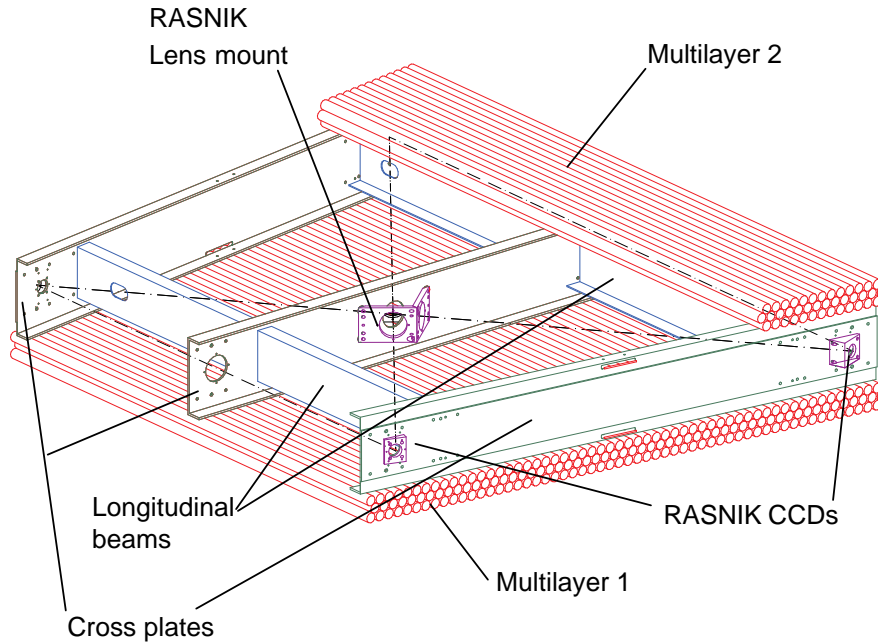


Figure 2.19: A schematic view of an end-cap MDT chamber with the optical alignment system [11].

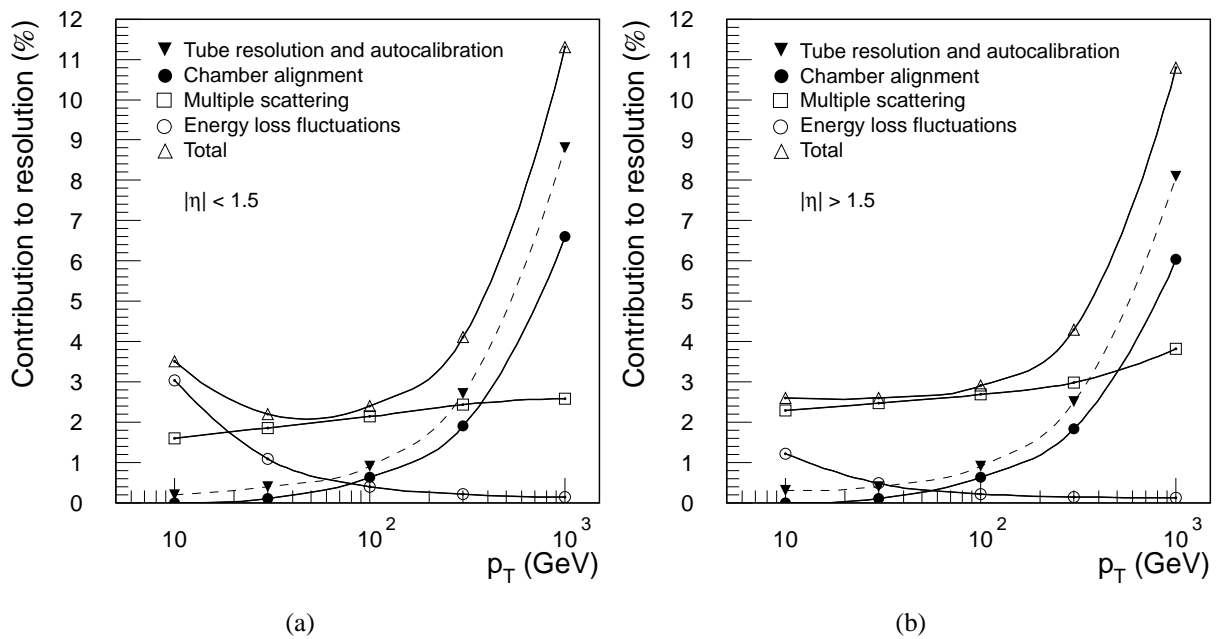


Figure 2.20: A calculated typical momentum resolution for muons reconstructed in the muon spectrometer. The alignment curve is for an uncertainty of $30 \mu\text{m}$ in the chamber positions. (a) is for $|\eta| < 1.5$ and (b) is for $|\eta| > 1.5$ [11].

CSC is shown in Figure 2.21(a). The CSC provides η and ϕ positions and each chamber contains four CSC planes, which results in four independent measurements in η and ϕ along each track. The structure of CSC is shown in Figure 2.21(b).

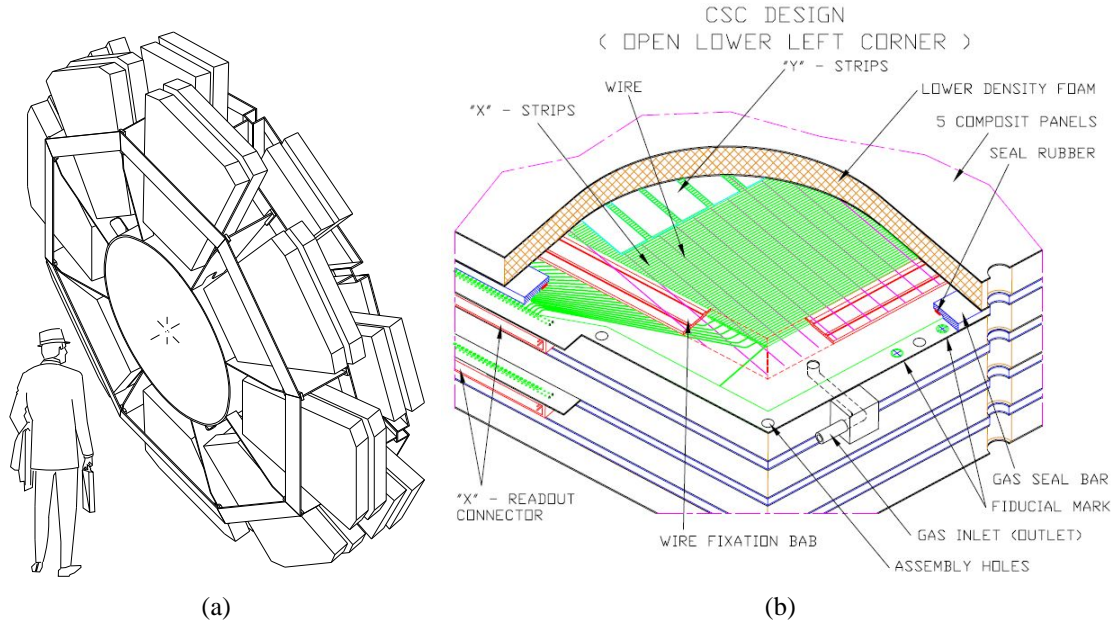


Figure 2.21: (a) The CSCs mounted on a rigid wheel inclined by 11.59° [11]. (b) A cutout view of a CSC chamber [13].

The resolution of the CSC reaches $60\ \mu\text{m}$ per CSC plane in the bending direction, and 5 mm in the non-bending direction.

RPC

The trigger detectors must provide acceptance in the range $|\eta| \leq 2.4$ and over the full ϕ -range. In the barrel, Resistive Plate Chambers (RPCs) are used to satisfy the requirement for spatial and time resolution. The cross-section through an RPC is shown in Figure 2.22. The RPC consists of three concentric cylindrical layers around the beam axis as shown in Figure 2.15. It is a gaseous parallel electrode-plate detector. Two resistive plates are kept parallel to each other at a distance of 2 mm by insulating spacers. The electric field between the plates is about 4.9 kV/mm and mixture of $\text{C}_2\text{H}_2\text{F}_4/\text{Iso-C}_4\text{H}_{10}/\text{SF}_6$ (94.7%/5%/0.3%) is used. The large lever arm between inner and outer RPCs permits the trigger to provide thresholds in the range 9-35 GeV for high momentum tracks, while the two inner chambers provides the low- p_T trigger in the range 6-9 GeV. Each station consists of two independent detector layers and measures η and ϕ . The resolution of an RPC chamber is 10 mm for both z and ϕ directions.

TGC

Thin Gap Chambers (TGCs) provide two functions in the end-cap muon spectrometer. One is the muon trigger capability and the other is provision of the η - ϕ coordinate. The second coor-

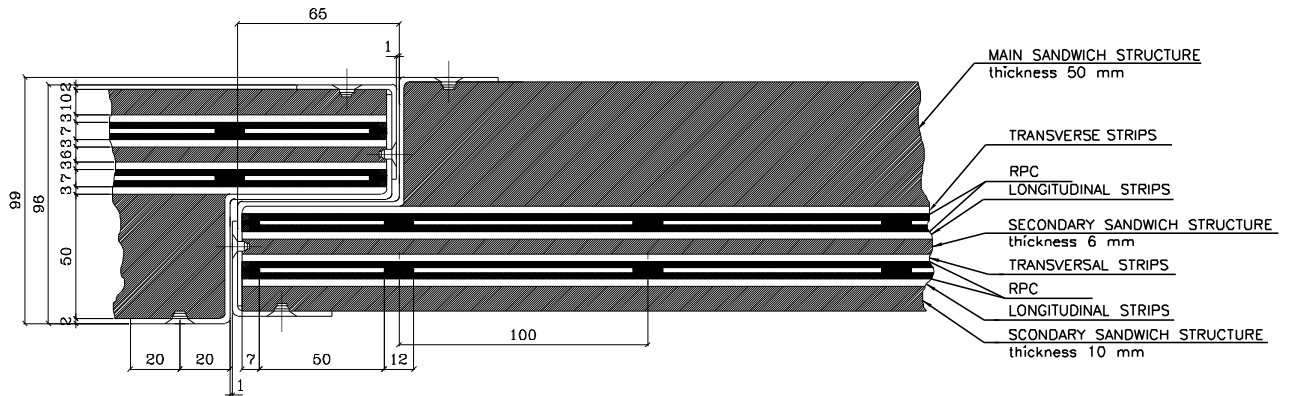


Figure 2.22: The cross section of an RPC chamber [11].

dinate, azimuthal angle ϕ is complementary information of the MDT measurement because the MDT measures only η direction. The middle layer of the MDTs in the end-cap is complemented by seven layers of TGCs, while the inner layer is complemented by two layers. The inner layer is segmented radially into two chambers; end-cap inner (EI) and forward inner (FI, also known as the small wheel). EI TGC's are mounted on support structures of the barrel toroid coils. TGCs are multi-wire proportional chambers with the characteristic that the wire-to-cathode distance of 1.4 mm is smaller than the wire-to-wire distance of 1.8 mm, as shown in Figure 2.3.5. The gas used is mixture of CO_2 and $\text{n-C}_5\text{H}_{12}$ (n-pentane). They are operated typically at 2800 V. The TGC provides η and ϕ position with the resolution of 2-6 mm for R, 3-7 mm for ϕ in a TGC chamber.

2.3.6 Magnets

Four superconducting magnets provide the magnetic field over a volume of approximately 12000 m^3 . The spatial arrangement of the coil windings is shown in Figure 2.24.

They consist of a solenoid, a barrel toroid and two end-cap toroids. The solenoid is aligned on the beam axis and provides a 2 T axial magnetic field for the inner detector, while minimizing the radiative thickness in front of the barrel electromagnetic calorimeter. The barrel toroid and two end-cap toroids produce toroidal magnetic fields of approximately 0.5 T and 1 T for the muon detectors in the central and end-cap regions, respectively.

Central solenoid

The solenoid is designed to provide a 2 T axial field. To achieve the desired calorimeter performance, the layout was optimized to keep the material thickness in front of the calorimeter as lower as possible. The radiation length is about $0.66 X_0$ at normal incidence. Inner and outer diameters of the solenoid are 2.46 m and 2.56 m and its axial length is 5.8 m. The flux is returned by the steel of the hadronic calorimeter and its girder structure.

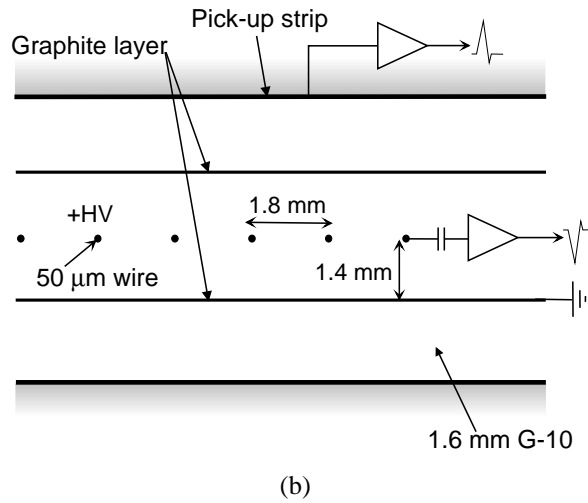
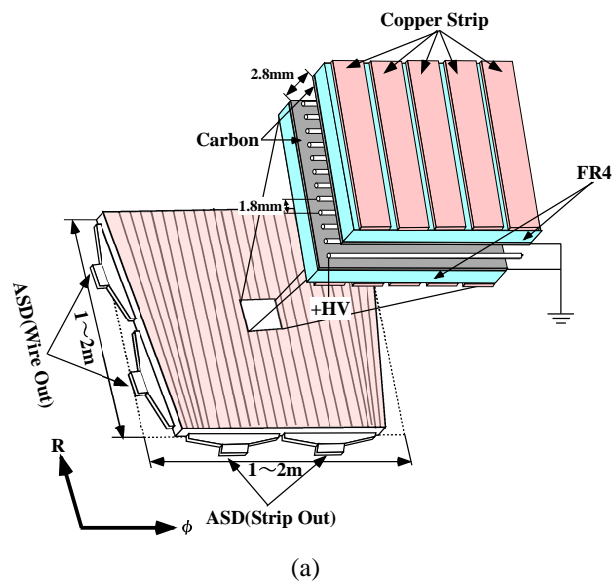


Figure 2.23: (a) A schematic illustration of a TGC chamber. (b) TGC structure showing anode wires, graphite cathodes, G-10 layers, and a read-out strip orthogonal to the wire [11].

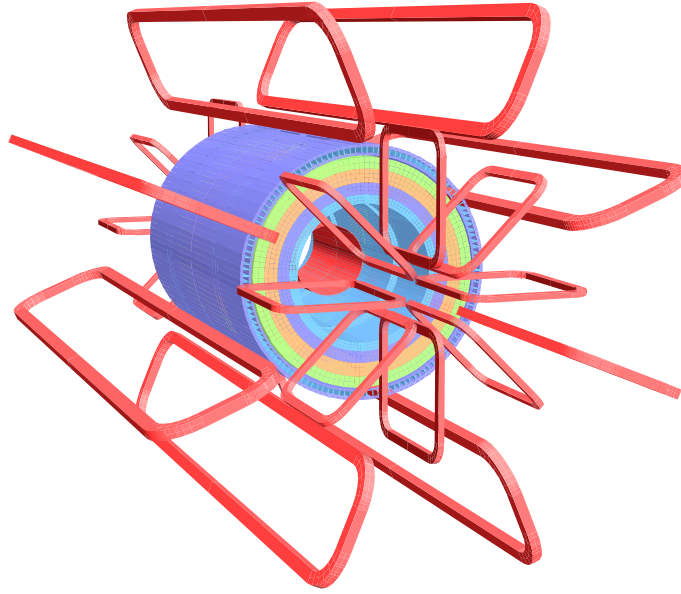


Figure 2.24: A cutaway view of the ATLAS superconducting magnetic system. The eight barrel toroid coils with the end-cap coils interleaved are visible. The solenoid winding lies inside the calorimeter volume. The tile calorimeter is modeled by four layers with different magnetic properties plus an outside return yoke [14].

Barrel toroid

The cylindrical volume surrounding the calorimeters and both end-cap toroids is filled by the magnetic field of the barrel toroid, which consists of eight coils. The overall size of the barrel toroid system is 25.3 m in length, with inner and outer diameters of 9.4 m and 20.1 m, respectively.

End-cap toroids

These toroids generate the magnetic field required for optimizing the bending power in the end-cap regions of the muon spectrometer system. Each end-cap toroid consists of a single cold mass built up from eight flat, square coil units and eight keystone wedges, bolted and glued together into a rigid structure to withstand the Lorentz forces.

The available bending power is shown in Figure 2.25 as a function of $|\eta|$.

The regions with low field integral between $|\eta| = 1.4$ and $|\eta| = 1.6$ correspond to trajectories in the plane of an end-cap coil or of a barrel coil, where the fringe field of one magnet largely cancels the bending power of the other.

The specification on the determination of the magnetic field are rather different in the inner detector and the muon spectrometer. In the inner detector, the systematic error affecting the momentum measurement of charged tracks is dominated by the relative alignment of detector components and by bending power uncertainties, the former being the more demanding. As one example, a lepton from W decay carries typically a transverse momentum of 40 GeV, resulting in a sagitta of approximately 1 mm as the lepton beyond the $1 \mu\text{m}$ level or 0.1% of the sagitta.

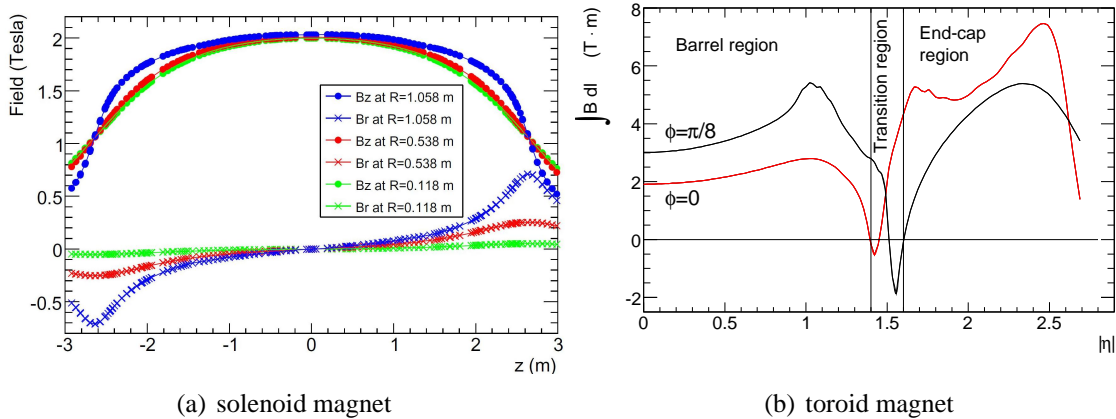


Figure 2.25: Magnetic field for the solenoid and bending power for the toroid magnet [14].

This suggests setting a target of about 5×10^{-4} for the fractional bending power uncertainty, so that it remains negligible in the determination of the absolute momentum scale.

In the muon spectrometer, the expected sagitta is approximately 0.5 mm for a muon with a momentum of 1 TeV. The extraction of the momentum from MDT chamber measurements requires a precise knowledge of the field integral between consecutive chambers along the muon trajectory. Because the field gradient can reach 1mT/mm, local bending power uncertainties translate into fluctuations of the momentum scale from one region in space to another, adding in quadrature to the overall momentum resolution.

For a given muon trajectory, three sources of uncertainty affect the measured curvature

1. field measurement errors
2. accuracy on the relative position of muon chambers and magnet coils
3. trajectory measurement errors, in particular along the direction of MDT wires.

For the purpose of setting specifications, it has been required that the combined effect of these sources degrade the momentum resolution by no more than 5% in relative term; each source should then contribute no more than about 3% of fractional resolution degradation, anywhere in the spectrometer volume. The corresponding functional requirements are summarised in Table 2.4

2.4 Trigger and Data Acquisition

Figure 2.26 shows the overview of the ATLAS Trigger and Data Acquisition (TDAQ) system. This section clarifies how the TDAQ system performs the event selection and records events which are selected by the trigger system.

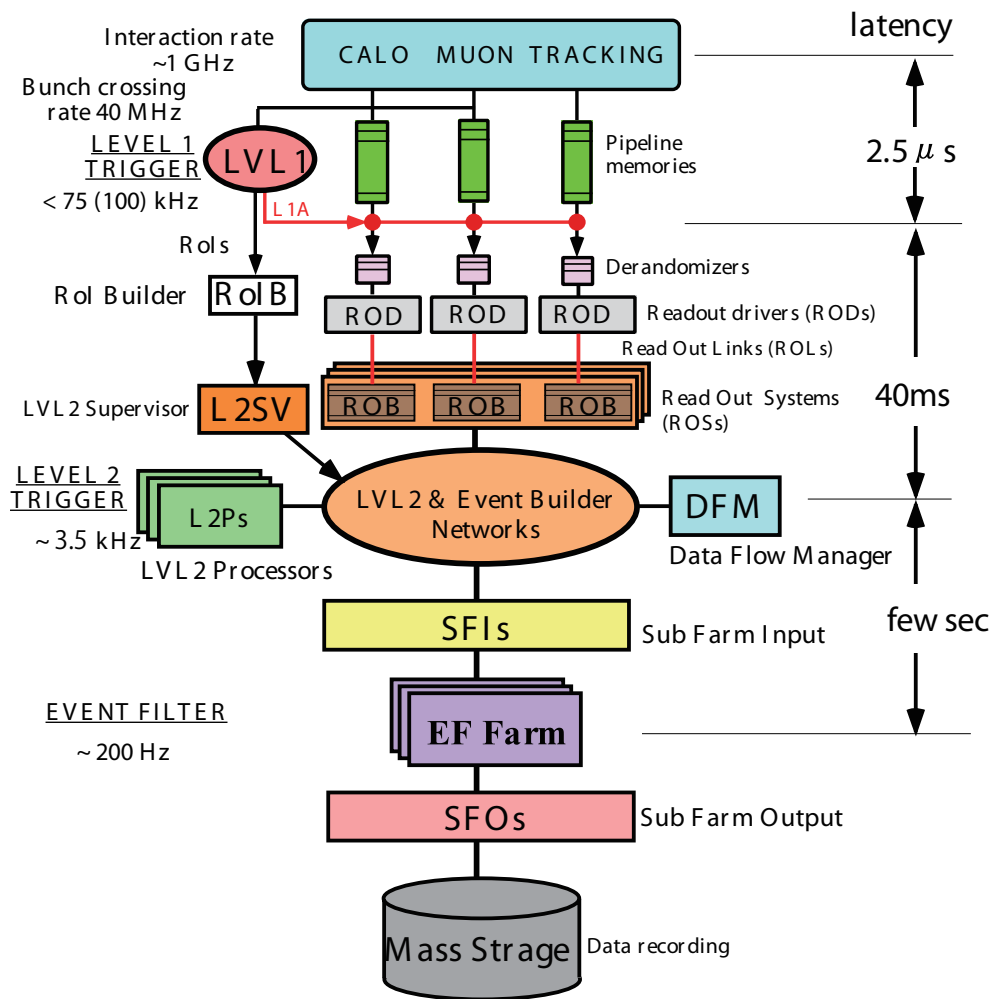


Figure 2.26: Schematic views of the ATLAS TDAQ system [15].

Criterion	Bending-power accuracy	MDT drift properties
Performance	$\Delta\sigma_{p_T}/\sigma_{p_T} < 5\%$ overall	Single-wire resolution degraded by $< 5\%$
Field measurement accuracy	$\Delta B_\phi/B_\phi < 2 - 5 \times 10^{-3}$	$\Delta B_{x,y,z} < 4$ mT (relative over chamber)
Reconstructed position of toroid conductors with respect to MDT tower	$\Delta R \sim 1 - 12$ mm , $R\Delta\phi \sim 1 - 6$ mm , $\Delta z \sim 2 - 30$ mm	–
Muon chamber 2nd-coordinate resolution	1.7 – 5.5 mm	6 – ~ 100 mm

Table 2.4: magnetic-field-related performance specification

2.4.1 Trigger

The ATLAS trigger system performs event selections in three steps. The first level trigger is called Level-1 (L1), the second level trigger is Level-2 (L2) and the final trigger is event filter (EF). The L2 and event filter are called together as High-Level Trigger (HLT). The L1 trigger is performed by hardware logic, while the HLT is done based on software.

Figure 2.27 shows the block diagram of the L1 trigger. The L1 trigger searches high p_T muons, electrons/photons, jets, and τ -leptons decaying into hadrons. It also selects events with large missing transverse energy (E_T^{miss}) and large total transverse energy. The L1 trigger uses information from the RPC and TGC for high- p_T muons, and all the calorimeter sub-system for electromagnetic clusters, jets, τ -leptons, E_T^{miss} , and large total transverse energy. The maximum L1 accept rate which the detector readout systems can handle is 75 kHz, and the L1 decision must reach the front-end electronics within $2.5 \mu\text{s}$ after the bunch-crossing.

The L2 trigger is seeded by Regions-of-Interest (RoIs). The RoI is the regions of the detector where the L1 trigger has found objects which passed the L1 selection criteria. The L2 trigger uses coordinates provided by the RoI, energy, and type of signatures. The L2 trigger reduces the event rate to below 3.5 kHz, with an average event processing time of approximately 40 ms.

The event filter uses offline analysis procedures on fully-built events to select events down to a rate which can be recorded for subsequent offline analysis. It reduces the event rate to approximately 200 Hz, with an average event processing time of order several seconds.

Muon Trigger

A L1 muon trigger identifies muons with six p_T thresholds and estimates the position of the detector region to be analyzed in the HLT. The geometric coverage of the L1 trigger in the end-cap regions is about 99% and is about 80% in the barrel region [17]. The limited geometric coverage in the barrel region is due to crack at around $\eta = 0$ to provide space for services of the ID and the calorimeters, the feet and rib support structures of the ATLAS detector and two small elevators in the bottom part of the spectrometer. The L1 trigger is based on dedicated detectors, the RPC and the TGC. While the RPC covers the barrel region ($|\eta| < 1.05$), the TGC covers the end-cap region ($1.05 < |\eta| < 2.4$). They provide a sufficient timing accuracy to provide unambiguous identification of the bunch-crossing. Both the RPC and the TGC have

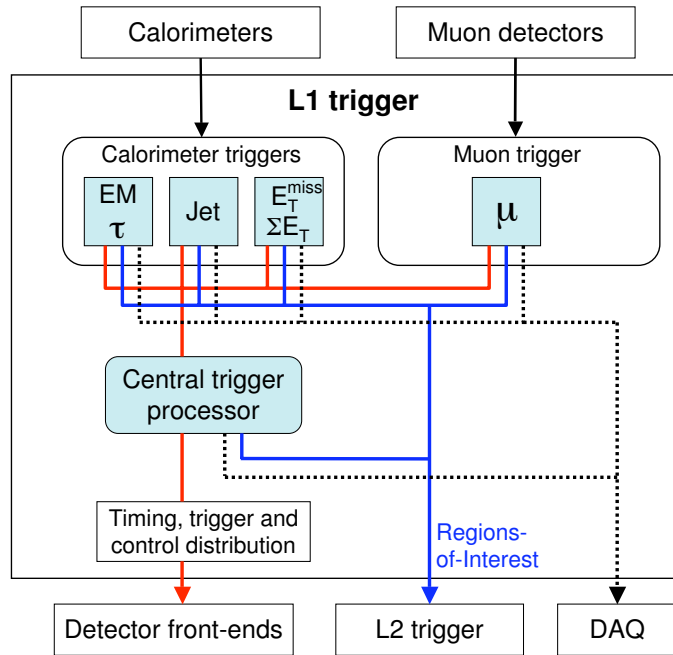


Figure 2.27: Block diagram of the L1 trigger [15].

three trigger stations each as shown in Figure 2.28. The basic principle of the algorithm is to require a coincidence of hits in the different trigger stations within a road, which tracks the path of a muon from the interaction point through the detector and the magnetic field. The width of the road is related to the p_T threshold to be applied. A system of programmable coincidence logic allows concurrent operation with a total of six thresholds. 2.28

The HLT selects events with fast L2 muon algorithms and EF muon algorithms that rely on offline muon reconstruction software. The result of the muon reconstruction at each step of the HLT is passed to trigger decision algorithms to determine whether a muon candidate will be processed further or discarded. At L2 the candidate from L1 is refined by using the precision data from MDTs. The L2 muon standalone algorithm constructs a track from the Muon Spectrometer data within the RoI defined by the L1 seed. The momentum and the track parameters of the muon candidate are improved by fast fitting algorithms and Look Up Tables. Firstly a pattern recognition algorithm selects hits from the MDT inside a region identified by the L1. Secondly a track fit is performed using the MDT drift times, and a p_T measurement is performed using Look Up Tables. Then reconstructed tracks in the ID are combined with the tracks found by the L2 muon Stand Alone by a fast track combination algorithm (CB) to refine the track parameter resolution.

At the EF stage, the full event data are accessible. The muon reconstruction starts from the RoI identified by L1 and L2, reconstructing segments and tracks using information from the trigger and precision chambers. The track is then extrapolated back to the beam line to determine the track parameters at the interaction point, thus forming a muon candidate using Muon Spectrometer information only, resulting in the EF standalone trigger. Similar to what is

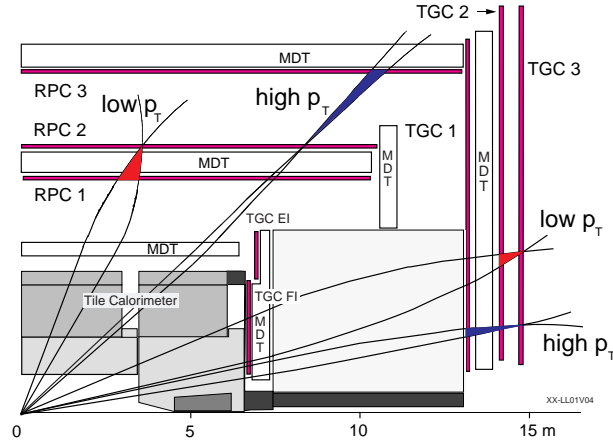


Figure 2.28: Schematic of the muon trigger system. The second station of the RPC (RPC2) and the outermost station of the TGC (TGC3) are the reference planes for barrel and end-cap, respectively [11].

performed in the L2 algorithms, the muon candidate is combined with an ID track to form an EF muon combined (CB) trigger. This strategy is called "outside-in". In addition to the "outside-in" algorithm, there is a complementary trigger which starts with ID tracks and extrapolates them to the muon detector to form EF triggers. This strategy is called "inside-out". These two algorithms have similar performance. In this study, the "inside-out" trigger is used.

Muon trigger efficiency measurement with data

Understanding the trigger performance is important for all physics analysis, and the $W^\pm Z$ analysis is also no exception.

The muon trigger efficiency in a single muon simulation sample can be defined as

$$\varepsilon_{MC} = \frac{\text{Probes matched with trigger object}}{\text{All probes (all truth muons)}}. \quad (2.4)$$

In order to measure the trigger efficiency in data, one needs to define the probe with least bias. However, most of the events having high p_T muon(s) are triggered by muon triggers and therefore measuring the trigger efficiency with such events by using the above equation and just defining the reconstructed muon as probe can have a trigger bias. In addition to that, there is a possibility that the reconstructed muon is not a prompt muon. That is why some treatments to remove such effects are needed for the accurate measurement.

As one of solutions, the Tag-and-Probe method is employed in the study. The Tag-and-Probe method requires a pair of a combined muon track, which is described in 2.5.2, and the invariant mass of the two tracks close to the Z boson mass or J/ψ mass. And either of the tracks must be matched with trigger object. The combined muon track matched with the trigger object is called "Tag" and the other track is called "Probe". The requirement of the invariant mass ensure the two muons are prompt ones and can increase the purity, while the matching a track with trigger object can remove the trigger bias. Figure 2.29 shows an example of the Tag muon

and Probe muon in the muon spectrometer. In the Tag-and-Probe method, the trigger efficiency

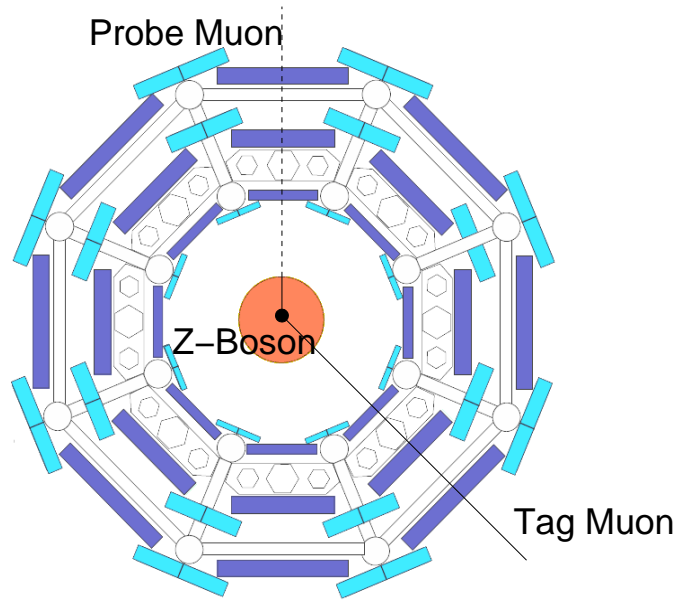


Figure 2.29: Tag-and-Probe method. The method uses two reconstructed muons whose invariant mass is close to the Z or J/ψ mass (In the Z boson case, it is $|M_{\text{inv}} - M_{\text{PDG}}| < 10 \text{ GeV}$). After requiring the mass selection, one of the two muons has to be matched with a trigger object that triggered the event. This treatment removes a trigger bias for the efficiency measurement. The muon track matched with the trigger object is called "Tag" and the other track is called "Probe" [16].

is defined as:

$$\varepsilon = \frac{\text{Z or } J/\psi \text{ candidates with Probes matched with trigger object}}{\text{All Z or } J/\psi \text{ candidates with Probes}}. \quad (2.5)$$

Due to the limitation of the bandwidth for triggers, the primary trigger has to be changed as the instantaneous luminosity of the LHC increases. During the 2011 data taking period, the p_T threshold of the lowest unprecaled single muon trigger was kept at 18 GeV. The convention used for the trigger signature naming describes the lowest trigger as "EF_mu18.inside-out", which indicates a single muon whose p_T is greater than 18 GeV with the "outside-in" algorithm at the Event Filter. Although the lowest single muon trigger was kept at 18 GeV during 2011, the Level 1 trigger threshold in the barrel region which is the seed for the 18 GeV trigger was changed in order to keep within the allocated bandwidth for the Level 1 muon trigger. The change was applied after period J, from which the instantaneous luminosity was above $1.9 \times 10^{33} \text{ cm}^{-2}\text{s}^{-1}$. Following the change, trigger name was also modified after the period, which was "EF_mu18.inside-out_medium". The "medium" represents the change.

Figure 2.30 shows the efficiency of muon trigger which is used in the analysis measured with the Tag-and-Probe method.

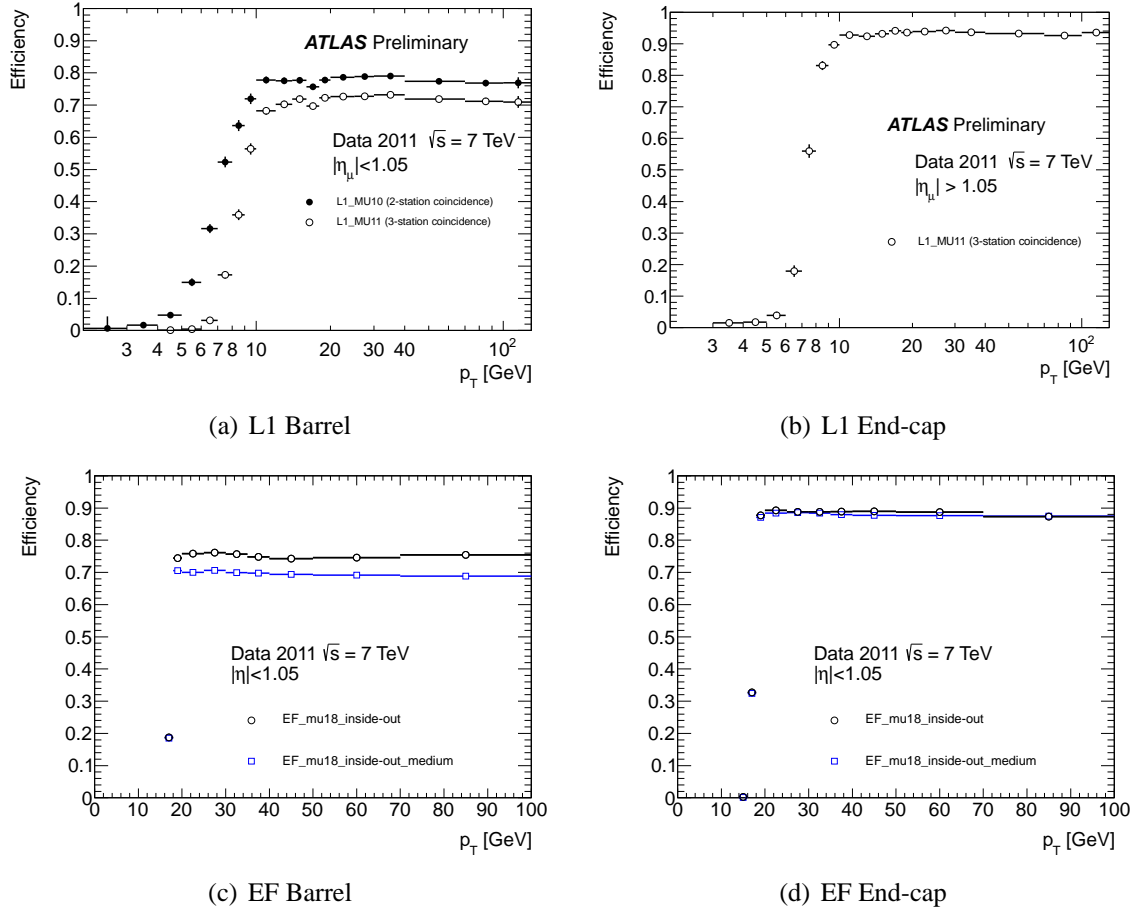


Figure 2.30: Muon single trigger efficiency used in the study. While the RPC covers the barrel region ($|\eta| < 1.05$) as a muon trigger detector, the TGC covers the end-cap region ($1.05 < |\eta| < 2.4$). The Level 1 trigger threshold in the barrel region which is the seed for the 18 GeV trigger was changed in order to keep within the allocated bandwidth for the Level 1 muon trigger, from L1_MU10 to L1_MU11 (a). The L1_MU10 consists of two station coincidence trigger in the barrel region, while the L1_MU11 is composed of coincidence of hits from three stations. Due to the smaller geometric coverage of the additional chambers required to form three-station coincidence triggers and hit efficiencies of the additional chambers, the L1_MU11 shows the efficiency drop of about 6 %. Following the change, the EF trigger efficiency in the barrel region also changed (c) [17].

Electron (photon) Trigger

Electrons and photons are reconstructed for the trigger in the range $|\eta| < 2.5$ [43]. The electron and photon trigger uses the information of the calorimeter and the inner detector.

At L1, electrons and photons are selected within $|\eta| < 2.5$ using calorimeter information with the reduced granularity of so-called trigger towers which have a dimension of $\Delta\eta \times \Delta\phi \approx 0.1 \times 0.1$. In each trigger tower, all the cells of the electromagnetic or hadron calorimeter are summed, with the exception of the fourth layer of the hadronic endcap and the barrel-endcap gap scintillators. L1 selection algorithm for electromagnetic clusters is based on a sliding 4×4 window of trigger towers which looks for local maxima as shown in Figure 2.31. A trigger is satisfied if the central 2×2 trigger towers in the 4×4 window has a local E_T maximum, and at least one pair of neighboring towers in the central 2×2 ones passes a trigger threshold. The region of central 2×2 towers is considered as the RoI.

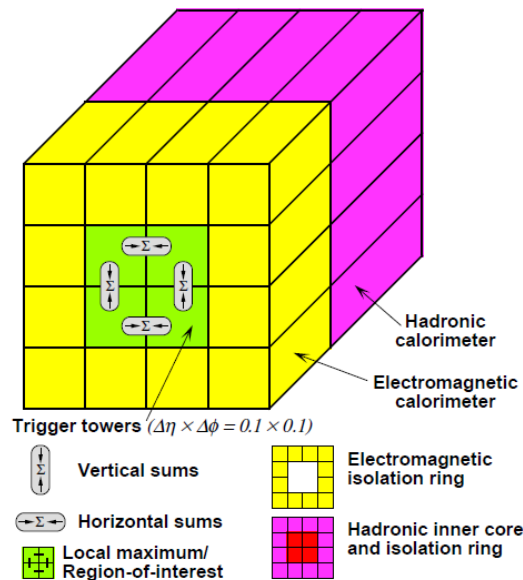


Figure 2.31: The concept for the electron/photon trigger algorithm [15].

Seeded by the RoI identified by the L1, the L2 photon and electron selection deploys a fast calorimeter algorithm. Due to latency constraints, the L2 algorithm uses only the second layer of the EM calorimeter to find the cell with the largest deposited transverse energy in the RoI close to the L1 position. This cell called the pre-seed. The final cluster position is obtained by calculating the energy weighted average cell positions on a 3×7 grid centered on the pre-seed. In order to accumulate the energy, two cluster sizes are used. When the cluster is in the barrel ($|\eta| < 1.4$), 3×7 cells grid is used whereas 5×5 cells is used in the end-cap region. In the case of electrons, a fast track reconstruction algorithm is also used in the RoI. This algorithm firstly processes determines the z-position of the primary interaction point along the beam axis and subsequently performs combinatorial tracking only inside group of space points with the same η and ϕ coordinates and matching the interaction point.

The EF uses the same reconstruction algorithms as offline as described in the Section 2.5.3.

The cluster reconstruction is done using a sliding window algorithm which acts on towers containing the energy. After this seed-finding step, fixed window clusters of size 3×7 are built starting from the second EM layer. New energy-weighted η and ϕ positions are calculated and subsequently cluster building is extended to the other layers of the EM calorimeter. Due to time constraints, bremsstrahlung recovery is not performed. A track reconstruction algorithm is also used in the EF level. .

Electron trigger performance

As in the case of the muon trigger, the lowest unprescaled electron trigger in 2011 also changed depending on the operation of LHC [18]. Until when the instantaneous luminosity reached $2.0 \times 10^{33} \text{ cm}^{-2}\text{s}^{-1}$, which corresponds to the period up to J, the primary trigger was the one requiring an electron whose E_T is greater than 20 GeV with medium identification criteria at the Event Filter, which denotes as "EF_e20_medium". The medium identification requires shower shapes and track qualities to reduce fake electrons while keeping high trigger efficiency.

When the instantaneous luminosity above $2.0 \times 10^{33} \text{ cm}^{-2}\text{s}^{-1}$, the lowest trigger was raised from 20 GeV to 22 GeV, which denotes "EF_e22_medium".

Above the instantaneous luminosity $2.3 \times 10^{33} \text{ cm}^{-2}\text{s}^{-1}$, an hadronic leakage requirement was applied at the Level 1 trigger to avoid raising the threshold further. The hadronic leakage requirement consisted of a veto on hadronic energy of more than or equal to 1 GeV deposited in the hadronic layers of the calorimeter, within a region of 0.2×0.2 in $\eta \times \phi$ behind the EM cluster. To represent the change, the letters "vh" was added to the trigger name. Besides that, re-optimized identification criteria named as "medium1" were also deployed. The re-optimized identification requires tighter cuts on shower shapes and additional track qualities compared to the medium identification. The lowest trigger name during the period is "EF_e22vh_medium1".

Their trigger efficiencies are shown in Figure 2.32.

2.4.2 DAQ

The ATLAS DAQ system is responsible for reading out event data from the detector subsystems and recoding them for further offline analysis. Since the ATLAS consists of a number of sub-detectors, some common architectures and requirements are needed to adjust timing and standardize data format among the sub-systems. Each sub-detector must have

- Front-end analogue or analogue-to-digital processing
- L1 buffer in which the information is retained for a time long enough to accommodate the L1 trigger latency ($2.5\mu\text{s}$)
- Derandomising buffer in which the data corresponding to a L1 trigger accept are stored before being sent to the following level
- Dedicated links or buses which are used to transmit the front-end data stream to the following DAQ systems

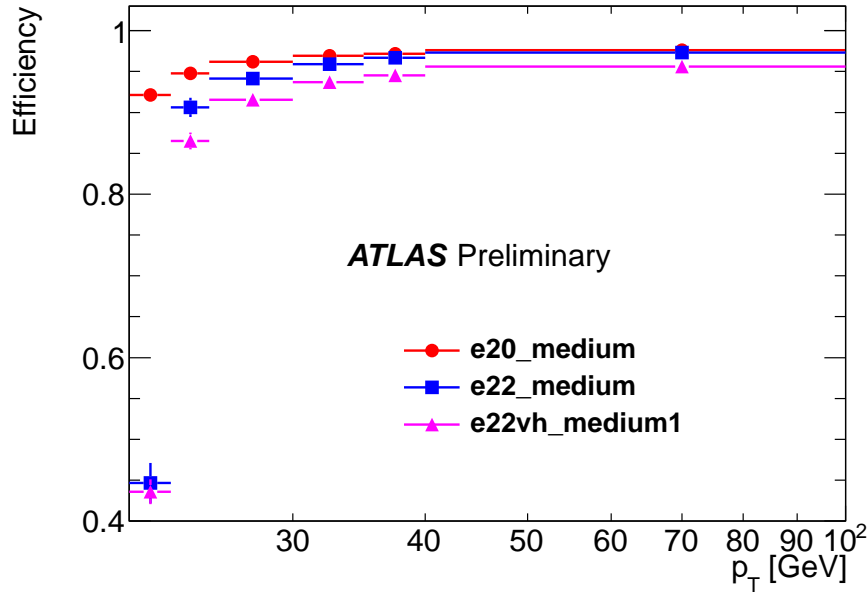


Figure 2.32: Electron trigger efficiency [18]. Integrated luminosities 1.8 fb^{-1} , 0.6 fb^{-1} and 2.5 fb^{-1} were recorded by ATLAS when lowest unprescaled triggers were e20_medium, e22_medium and e22vh_medium1, respectively.

As shown in Figure 2.26, the movement of events from the detector to storage proceeds with the L1 trigger selection. During the latency of the L1 trigger selection, the event data are buffered in memories located within the detector-specific front-end electronics. After an event is accepted by the L1 trigger, the data from the pipe-lines are transferred off the detector to the readout drivers (ROD's) which are the detector-specific functional elements of the front-end systems. The ROD's follow some general ATLAS rules, including the definition of the data format of the event, the error detection efficiency/recovery mechanisms to be implemented, and the physical interface for the data transmission to the following DAQ system.

The following DAQ system receives the data and the event fragments are received into the Readout Buffers (ROB's) which are contained in the Readout System (ROS) units where they are temporarily stored and provided. The ROSs each contain several ROBs. It is subsequently solicited by the L2 trigger for the event data associated to RoI's. Those events selected by the L2 trigger are then transferred to the event-building system, and subsequently to the event filter for final selection. Events selected by the event filter are moved to permanent storage at the CERN computer center. In addition to the movement of data, the DAQ also provides the configuration, control and monitoring of the hardware and software components.

2.5 Reconstruction Scheme

This section describes the way of reconstruction for the vertices, muons, electrons, E_T^{miss} . Their performances are also shown.

2.5.1 Vertex Reconstruction

The reconstruction of primary vertices is organized in the following steps iteratively [44] :

1. Reconstructed tracks compatible with originating from the interaction region are pre-selected.
2. A vertex seed is found by looking for the global maximum in the distribution of z coordinates of the tracks.
3. The vertex position is determined with a fitting algorithm. The algorithm takes the seed position and the tracks as inputs. The fitting is a robust χ^2 based one.
4. Tracks incompatible with the vertex by more than approximately 7σ are used to seed a new vertex. The compatibility of the track to the vertex is expressed in terms of χ^2 with 2 degrees of freedom.

This procedure is repeated until no unassociated tracks are left in the event or no additional vertex can be found. Figure 3.38 shows the event display of typical reconstructed vertices in the ATLAS. The resolution of the reconstructed primary vertices is approximately $30\ \mu\text{m}$ for x (y) direction and $50\ \mu\text{m}$ for z direction when the $\sqrt{\sum_{\text{tracks}} p_{\text{T}}^2}$ is more than 8 GeV. The resolution is expected to improve significantly as the $\sqrt{\sum_{\text{tracks}} p_{\text{T}}^2}$ increases.

2.5.2 Muons

The muon reconstruction algorithm used in the analysis is called STACO (Statistical Combined) [45][46]. The standalone muon track reconstruction package in the STACO is called Muonboy which reconstructs muons in the following four procedures.

1. Region of Activity (ROA), which is a geometrical region defined in the η - ϕ space with the size of about $\eta \times \phi = 0.4 \times 0.4$, are identified using information from the trigger chambers. The center of ROA is placed where at least one TGC or RPC hit exists in both η - ϕ coordinate.
2. Local segments of a straight track are reconstructed in multilayers of each muon station in the ROA. They are made in three steps.
 - (a) Segment seeds are searched in the region where more than one ϕ hits are expected by taking any combinations of two hits in different multilayers in an MDT chamber with a loose IP constraint. Then a seed is matched with other hits in the same chamber using drift time information and fitting results are examined if the segment is valid or not. In this matching, δ -ray effect and efficiency of the MDT tubes are considered. Segments are required to be associated with at least one ϕ hit and sufficiently good fitting quality. Such segments are called strict segments.
 - (b) CSC segments are reconstructed in 3-D by requiring at least one ϕ hit.

- (c) A looser search, in which no ϕ hit is required and less stringent χ^2 cut, is performed. The position in the ϕ is determined by trying five positions along the tube.

In each of these steps, segments are searched in two consecutive passes. The first pass reconstructs segments which cross both multilayers in an MDT chamber while the second pass reconstructs the segments which cross only one multilayer to retain efficiency. In the second pass, in order to reduce fake combinations, only the hits left unused in the first pass are used and a fit quality cut is applied tightly.

3. Segments in different stations are combined by a 3-D tracking to form track candidates. Effects of the magnetic field is taken into account.
 - (a) The strict segments are used as seeds for the first rough momentum estimation. Each segment is then extrapolated to the neighboring stations by varying several different values of momentum around the estimation. If some matching exists with one or more loose segments, the one with the best matching is included in the track candidate and then a fit is performed to get a more accurate momentum estimation.
 - (b) The resulting track candidates are extrapolated to the all potentially crossed stations with a finer momentum scan. Any loosely matched segment is included in the candidate track and a new fit is performed using all the segments belonging to the track candidates. Only track candidates with two or more segments are kept after this stage.
4. A global fit is performed, starting from the best result of the previous fits, but using raw hit information, such as TDC values and hit strips. In this process all the hits are classified into good or bad. Only good hits are kept. After that, the final fit including the material effect is performed to get a most realistic result. Finally tracks of the muon are obtained. The reconstructed muons in this way are called "Combined (CB)" muon.

The covariance matrices of the track candidates are then computed by varying the fitted parameters taking their correlations into account. To have track parameters at the perigee, the candidate tracks are back-extrapolated to the beam axis and their covariance matrices are propagated taking into account the energy loss and the scattering in the calorimeters.

After searching the track candidates in the muon spectrometer, the STACO algorithm tries to find an inner detector track for a given muon spectrometer track using track parameters and covariance matrices. The match χ^2 is used as the difference between the inner detector and the muon spectrometer track vectors weighted by the combined matrix,

$$\chi_{match}^2 = (\mathbf{T}_{MS} - \mathbf{T}_{ID})^T (\mathbf{C}_{MS} - \mathbf{C}_{ID})^{-1} (\mathbf{T}_{MS} - \mathbf{T}_{ID}).$$

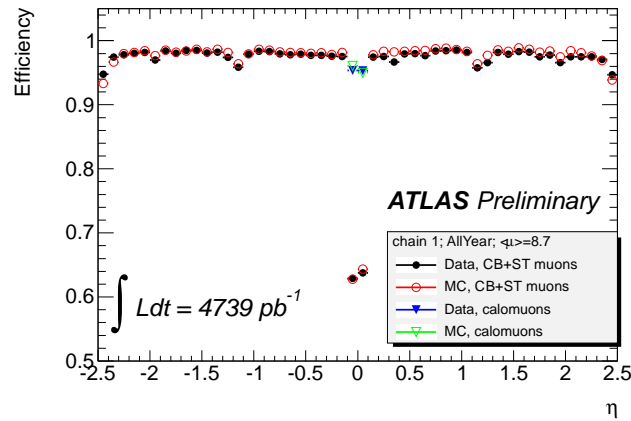
Here \mathbf{T} denotes a vector of track parameters expressed at the perigee and \mathbf{C} is its covariance matrix. Several track selection criteria, such as requirement of the same charge, η - ϕ matching, are applied on both the inner detector and the muon spectrometer track in addition to match χ^2 cut. The track parameters for the combined track is obtained by the statistical combination as,

$$\mathbf{T} = (\mathbf{C}_{ID}^{-1} - \mathbf{C}_{MS}^{-1})^{-1} (\mathbf{C}_{ID}^{-1} \mathbf{T}_{ID} - \mathbf{C}_{MS}^{-1} \mathbf{T}_{MS}).$$

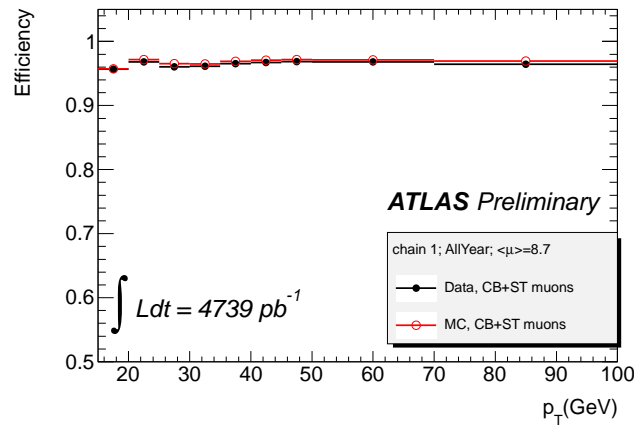
In addition to the combined muons, additional muon candidates can be obtained by a complementary algorithm [47]. It extrapolates the Inner detector tracks to the Muon Spectrometer and then tags the tracks with the first Muonboy segments which are in the inner or middle MS layer. This method can recover muons with low energy or in areas with limited MS coverage such as the place at $|\eta| \sim 0$. The muons reconstructed with the algorithm are called "Segment-Tagged (ST)" muons.

Muon reconstruction performance

Figure 2.33 shows the muon reconstruction efficiency as function of η and p_T for the Combined and Segment-Tagged muon. The efficiency at the plateau is about 97%.



(a) reconstruction efficiency as function of η



(b) reconstruction efficiency as function of p_T

Figure 2.33: Combined muon reconstruction efficiency with respect to the inner tracking efficiency as a function of the η (a) and p_T (b) of the muon for $p_T > 15$ GeV [19]. Chain 1 in the legend indicates the STACO algorithm and μ is the number of average interactions per bunch crossing. The name of calo muons shown in the legend of (a) indicates another reconstruction algorithm which is not used in the study.

Figure 2.34 shows the distribution of the invariant mass of two muons which is the closest to the Z mass in the event in data. The distribution of the $Z \rightarrow \mu\mu$ simulation is also shown.

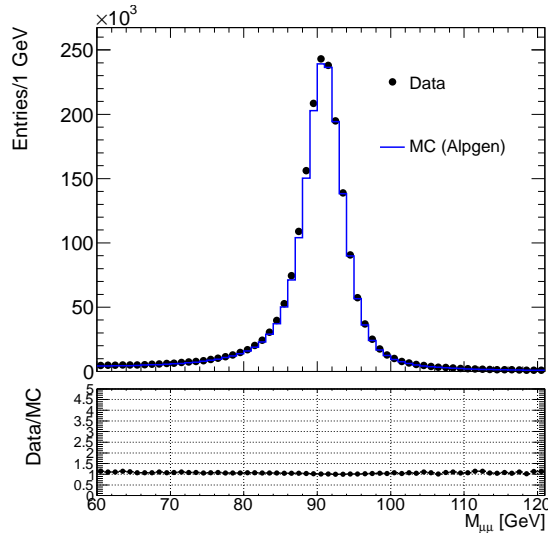


Figure 2.34: Invariant mass of $Z \rightarrow \mu\mu$.

2.5.3 Electrons

Three algorithms exist to reconstruct electrons in the ATLAS. The standard one is a cluster based reconstruction algorithm [48]. Another algorithm is a track based one dedicated mostly to low p_T electrons which is below the threshold used in this analysis. The third algorithm is dedicated to the electrons in the forward region of ATLAS ($2.5 < |\eta| < 4.9$), where the Inner Detector does not exist, and which is also out of the range used in this analysis. Here only the cluster based algorithm is mentioned.

The cluster based algorithm is seeded by a cluster which is reconstructed in the electromagnetic calorimeter and then they are associated to tracks of charged particles reconstructed in the Inner Detector. The procedure is as follows:

1. A cluster-finding algorithm forms seeds from clusters of towers (each tower covering 0.025×0.025 in $\eta \times \phi$ space) in the EM calorimeter using a sliding window algorithm with a window size of 3 towers \times 7 towers ($\eta \times \phi$).
2. In the region of the Inner Detector ($|\eta| < 2.5$), matching of a track with $p_T > 5\text{GeV}$ made by the ID to the cluster is performed. The matching proceeds in two steps. First, the eta and phi at the origin of the track are compared to the eta and phi of the cluster position. If there is reasonable agreement (0.2 in η , 0.1 in ϕ), as a second step the track is extrapolated to the calorimeter position of each compartment in depth, and $\Delta\eta$ and $\Delta\phi$ are calculated for each compartment. It is possible that more than one track matches the same seed cluster. In this case, the best match is considered as the one with smallest distance.

The track matching is affected by Bremsstrahlung losses which result in an asymmetric sign-dependent $\Delta\phi$ distribution. This issue is solved by extrapolating the track from the perigee and using the cluster energy for the electron momentum.

In addition to the reconstruction, there are electron identification criteria which provide a good separation between the electron and the other objects that fake electrons. The criteria consist of a number of variables such as the EM showers (longitudinal shower depth, lateral shower width) and the track quality and track-cluster matching. There are three types of criteria, which are defined with increasing background rejection power: loose, medium and tight. While the loose criteria has high efficiency of about 95 %, the tight criteria keep the purity of electrons high.

Electron performance

Figure 2.35 shows the identification efficiency in terms of the number of reconstructed vertices.

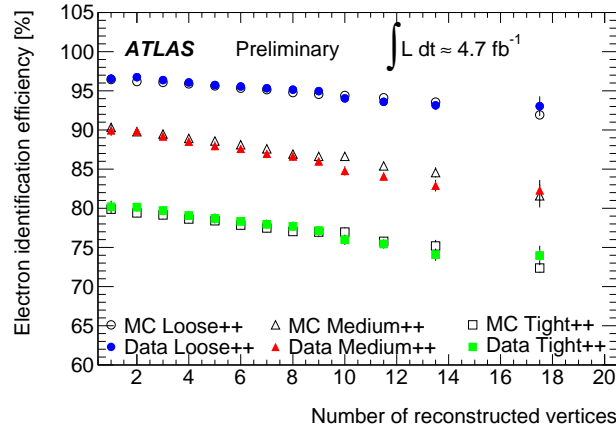


Figure 2.35: Identification efficiency in terms of the number of reconstructed vertices. The p_T range of the electrons is between 20 GeV and 50 GeV. The suffix ”++” attached to the name of each criteria means they are refined ones dedicated to 2011 data. The identification efficiency is found to drop. This loss is mainly due to an enhanced hadronic activity overlaid to the electron calorimetric shower [20].

Figure 2.36 shows the the distribution of the invariant mass of two electrons which is the closest to the Z mass in the event in data. The distribution of the $Z \rightarrow e^+e^-$ simulation is also shown.

2.5.4 Missing Energy

The E_T^{miss} reconstruction includes contributions from transverse energy deposits in the calorimeters and muons reconstructed in the muon spectrometer. The two E_T^{miss} components are calculated as [49] :

$$E_{x(y)}^{\text{miss}} = E_{x(y)}^{\text{miss,calo}} + E_{x(y)}^{\text{miss,\mu}} \quad (2.6)$$

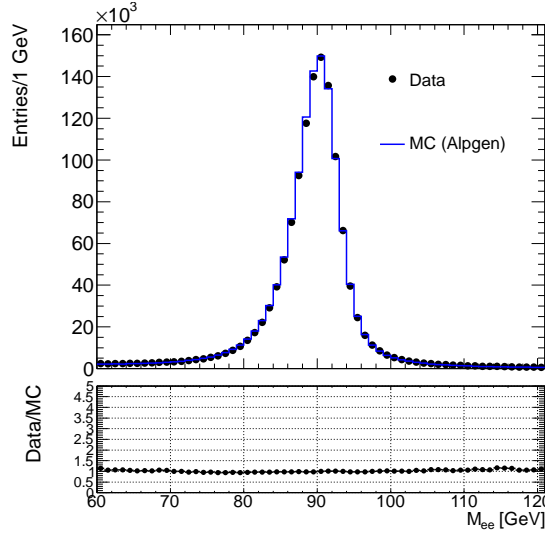


Figure 2.36: Invariant mass of $Z \rightarrow e^+e^-$.

The two terms in the above equation are referred to as the calorimeter and muon terms. The values of E_T^{miss} and its azimuthal position (ϕ^{miss}) are then calculated as:

$$\begin{aligned} E_T^{\text{miss}} &= \sqrt{(E_x^{\text{miss}})^2 + (E_y^{\text{miss}})^2} \\ \phi^{\text{miss}} &= \arctan(E_y^{\text{miss}}/E_x^{\text{miss}}) \end{aligned} \quad (2.7)$$

The Calorimeter Term

To suppress noise contributions, only cells belonging to three-dimensional topological clusters, referred as topoclusters are used. The topoclusters are firstly seeded by cells with deposited energy $|E_i| > 4\sigma_{\text{noise}}$. And then they are built by iteratively adding neighboring cells with $|E_i| > 2\sigma_{\text{noise}}$, and finally by adding neighbors of the accumulated cells.

Furthermore, in order to take into account effects from the detector response and the dead material in front and between the calorimeters, a calibration should be applied. To calculate the E_T^{miss} calorimeter term, a scheme in which the cells are calibrated on the basis of the reconstructed physics object to which the cells belong is employed. The calorimeter cells are associated with a reconstructed and identified high- p_T parent object in a chosen order: electrons, photons, hadronically decaying τ -leptons, jets and muons. Once the cells are associated with a category as described above and calibrated accordingly, E_T^{miss} is calculated as follows:

$$E_{x(y)}^{\text{miss,calo}} = E_{x(y)}^{\text{miss,e}} + E_{x(y)}^{\text{miss,\gamma}} + E_{x(y)}^{\text{miss,\tau}} + E_{x(y)}^{\text{miss,jets}} + E_{x(y)}^{\text{miss,softjets}} + E_{x(y)}^{\text{miss,calo,\mu}} + E_{x(y)}^{\text{miss,CellOut}} \quad (2.8)$$

where each term is calculated from the negative sum of calibrated cell energies inside the corresponding objects:

- $E_{x(y)}^{\text{miss,e}}$, $E_{x(y)}^{\text{miss,\gamma}}$, $E_{x(y)}^{\text{miss,\tau}}$ are reconstructed from cells in electrons, photons and taus, respectively

- $E_{x(y)}^{\text{miss,jets}}$ is reconstructed from cells in jets with $p_T > 20$ GeV
- $E_{x(y)}^{\text{miss,softjets}}$ is reconstructed from cells in jets with $7 \text{ GeV} < p_T < 20$ GeV
- $E_{x(y)}^{\text{miss,calo},\mu}$ is the contribution to E_T^{miss} originating from the energy lost by muons in the calorimeter.
- the $E_{x(y)}^{\text{miss,CellOut}}$ term is calculated from the cells in topoclusters which are not included in the reconstructed objects.

Jets are reconstructed at the *electromagnetic* scale, which is the energy scale that accounts correctly for the energy deposited in the calorimeter by electromagnetic showers [50]. Furthermore, in order to correct the energy and momentum of the jets measured in the calorimeter to those of the jets at the hadronic scale, the jet energy scale (JES) calibration is applied. Adding to them, the energy is also corrected for the pile-up effect.

The final $E_{x(y)}^{\text{miss}}$ is calculated from Equation 2.6 adding the $E_{x(y)}^{\text{miss},\mu}$ term as described below.

The Muon Term

The E_T^{miss} muon term is calculated from the momenta of muon tracks reconstructed with $|\eta| < 2.7$:

$$E_{x(y)}^{\text{miss},\mu} = - \sum_{\text{selectedmuons}} p_{x(y)}^{\mu} \quad (2.9)$$

In the region $|\eta| < 2.5$, the STACO muons are considered. In order to deal appropriately with the energy deposited by the muon in calorimeters, the muon term is calculated differently for isolated and non-isolated muons, as explained in the following:

- The p_T of an isolated muon is determined from the combined measurement of the inner detector and muon spectrometer. In this case the energy lost by the muon in the calorimeter ($E_{x(y)}^{\text{miss,calo},\mu}$) is not added to the calorimeter term to avoid double energy counting.
- For a non-isolated muon, the energy lost in the calorimeter cannot be separated from the nearby jet energy. The muon spectrometer measurement of the muon momentum after energy loss in the calorimeter is therefore used, unless there is a significant mis-match between the spectrometer and the combined measurements. In this case the combined measurement minus the parameterized energy loss in the calorimeter is used.

For higher values of pseudorapidity, outside the fiducial volume of the inner detector ($2.5 < |\eta| < 2.7$), there is no matched track requirement and the muon spectrometer p_T alone is used for both the isolated and non-isolated muons. Aside from the loss of muons outside the acceptance of the muon spectrometer ($|\eta| > 2.7$), muons can be lost in other regions (around $|\eta| = 0$ and 1.2) due to the limited coverage of the muon spectrometer. The muons reconstructed from the inner detector and calorimeter energy deposits can be used to recover their contributions to E_T^{miss} .

Although the core of the E_T^{miss} resolution is not match affected by the muon term, any muons which are non-reconstructed, badly-measured, or fake muons can be a source of significantly large fake E_T^{miss} .

E_T^{miss} performance

Figure 2.37 shows the distribution of E_T^{miss} for $Z \rightarrow \mu\mu$ and $W \rightarrow e\nu$ events. The MC simulation expectations are also superimposed. Each MC sample is weighted with its corresponding cross-section and then the total MC expectation is normalized to the number of events in data.

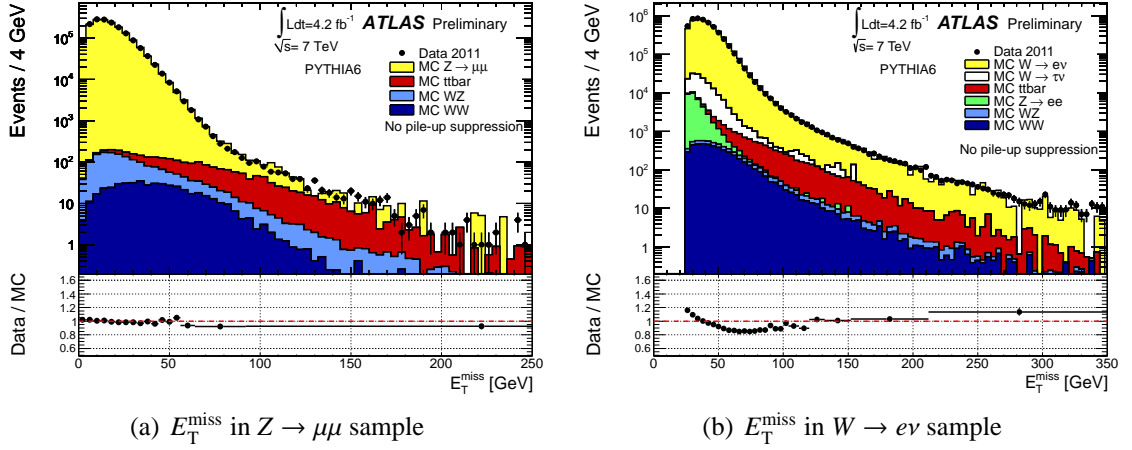


Figure 2.37: Distribution of E_T^{miss} as measured in a data sample of $Z \rightarrow \mu\mu$ (a) and $W \rightarrow e\nu$ (b) events. The expectation from Monte Carlo simulation (PYTHIA 6) is superimposed and normalized to data, after each MC sample is weighted with its corresponding cross-section. The lower part of figures show the ratio of data over MC [21].

Figure 2.5.4 shows the resolution for $Z \rightarrow \ell\ell$ events as function of the total transverse energy in the event, which is obtained by Equation (2.8).

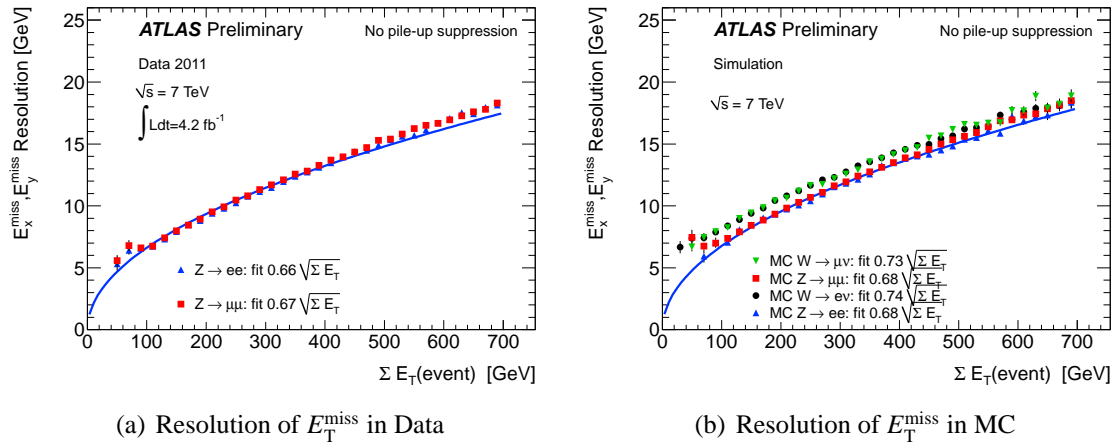


Figure 2.38: E_x^{miss} and E_y^{miss} resolution as a function of the total transverse energy in the event calculated by summing the p_T of muons and the total transverse energy in the calorimeter in data at $\sqrt{s} = 7$ TeV (a) and MC (b) [21]. The resolution of the two E_T^{miss} components is fitted with a function $\sigma = k\sqrt{\Sigma E_T}$ and the fitted values of the parameter k , expressed in $\text{GeV}^{1/2}$, are in the figure.

Chapter 3

The Datasets and Event Selection

3.1 Datasets

This section describes the data used in this analysis and the Monte Carlo simulation for estimates of both the signal and backgrounds.

3.1.1 Luminosity Measurement for the ATLAS

A precision luminosity measurement is of critical importance for all physics programs. Before mentioning data, this section describes how to measure the luminosity in the LHC and the ATLAS [27].

Principle

The luminosity of a pp collider can be expressed as

$$\mathcal{L} = \frac{R_{\text{inelastic}}}{\sigma_{\text{inelastic}}} = \frac{\mu n_b f_r}{\sigma_{\text{inelastic}}} = \frac{\mu_{\text{visible}} n_b f_r}{\sigma_{\text{visible}}}, \quad (3.1)$$

where $R_{\text{inelastic}}$ is the rate of inelastic collisions and $\sigma_{\text{inelastic}}$ is the pp inelastic cross-section, μ is the average number of inelastic interactions per bunch crossing (BC), n_b the bunch pairs colliding per revolution and f_r the revolution frequency in a storage ring. At the last term, μ_{visible} is the observed interaction rate per crossing which is measured with a variety of detectors and several different algorithms, $\sigma_{\text{visible}} = \varepsilon \sigma_{\text{inelastic}}$ is the total inelastic cross-section multiplied by the efficiency ε of a particular detector and algorithm, and similarly $\mu_{\text{visible}} = \varepsilon \mu$. Since μ_{visible} is an experimentally observable quantity, the calibration of the luminosity scale for a particular detector and algorithm is equivalent to determining the visible cross-section σ_{visible} .

van der Meer Scan

In order to use the measured interaction rate μ_{visible} as a luminosity monitor, each detector and algorithm must be calibrated by determining its σ_{visible} . The primary calibration technique to determine the absolute luminosity scale of each luminosity detector and algorithm employs

dedicated van der Meer (*vdM*) scans to infer the delivered luminosity at one point in time from the measurable parameters of the colliding bunches. By comparing the known luminosity delivered in the *vdM* scan to the visible interaction rate μ_{visible} , the visible cross-section can be determined from Equation 3.1.

The delivered luminosity can be written in terms of the accelerator parameters as

$$\mathcal{L} = \frac{n_b f_r n_1 n_2}{2\pi \Sigma_x \Sigma_y}, \quad (3.2)$$

where n_1 and n_2 are number of protons per bunch in beam 1 and beam 2, respectively, and Σ_x and Σ_y characterize the horizontal and vertical convolved beam widths. In a *vdM* scan, the beams are separated by step of a known distance which allows a direct measurement of Σ_x and Σ_y . Combining this scan with an external measurement of the bunch population product $n_1 n_2$ provides a direct determination of the luminosity when the beams are unseparated.

To achieve the desired accuracy on the absolute luminosity, these scans are not performed during normal physics operations, but rather under carefully controlled conditions with a limited number of colliding bunches and a modest peak interaction rate.

EventOR Algorithm

The majority of the algorithms used in the ATLAS luminosity determination are event counting algorithms, where each particular bunch crossing is categorized as either passing or not passing a given set of criteria designed to detect the presence of at least one inelastic *pp* collision. The two main algorithm types being used are EventOR (inclusive counting) and EventAND (coincidence counting). Here only the EventOR algorithm used in the analysis is mentioned. Since in general there can be more than one *pp* inelastic collision per bunch crossing, the visible interaction rate μ_{visible} must be determined from the observed event rates using the formulae described in the following.

Most of the primary luminosity detectors in ATLAS consist of two symmetric detector elements placed in the forward ("A") and backward ("C") direction from the interaction point (IP). For the Beam Condition Monitor, which is described in the next section, each side is further segmented into a discrete number of readout segments, typically arranged azimuthally around the beampipe.

In the EventOR algorithm, a bunch crossing will be counted if there is at least one hit on either the A side or the C side. Assuming that the number of interactions in a bunch crossing can be described by a Poisson distribution, the probability of observing an OR event can be computed as

$$P_{\text{Event.OR}}(\mu_{\text{visible}}^{\text{OR}}) = \frac{N_{\text{OR}}}{N_{\text{BC}}} = 1 - e^{-\mu_{\text{visible}}^{\text{OR}}}. \quad (3.3)$$

Here the raw event count N_{OR} is the number of bunch crossings, during a given time interval, in which at least one *pp* interaction satisfies the event-selection criteria of the OR algorithm under consideration, and N_{BC} is the total number of bunch crossings during the same interval. Solving for μ_{visible} :

$$\mu_{\text{visible}}^{\text{OR}} = -\ln\left(1 - \frac{N_{\text{OR}}}{N_{\text{BC}}}\right). \quad (3.4)$$

Beam Condition Monitor

The ATLAS uses a number of sub-detectors and algorithms to measure the luminosity simultaneously. One of these sub-detectors is the Beam Condition Monitors (BCM). The BCM was primarily used in 2011 and determined the integrated luminosity for physics analysis.

The detector consists of four small diamond sensors, which are arranged around the beampipe on each side of the IP, at a distance of $z = \pm 184$ cm [51]. The overview of the BCM is shown in Figure 3.1. The BCM is a fast device originally designed to monitor background levels and issue beam-abort requests when beam losses start to risk damaging the Inner Detector. The fast readout of the BCM also provides a bunch-by-bunch luminosity signal at $|\eta| = 4.2$ with a time resolution of ≈ 0.7 ns. The horizontal and vertical pairs of BCM detectors are read out separately, which leads to two luminosity measurements labeled as BCMH and BCMV respectively. These two measurements are treated as being made by independent devices for calibration and monitoring purposes. In 2011, the BCMV with EventOR algorithm is primarily used to determine the luminosity.

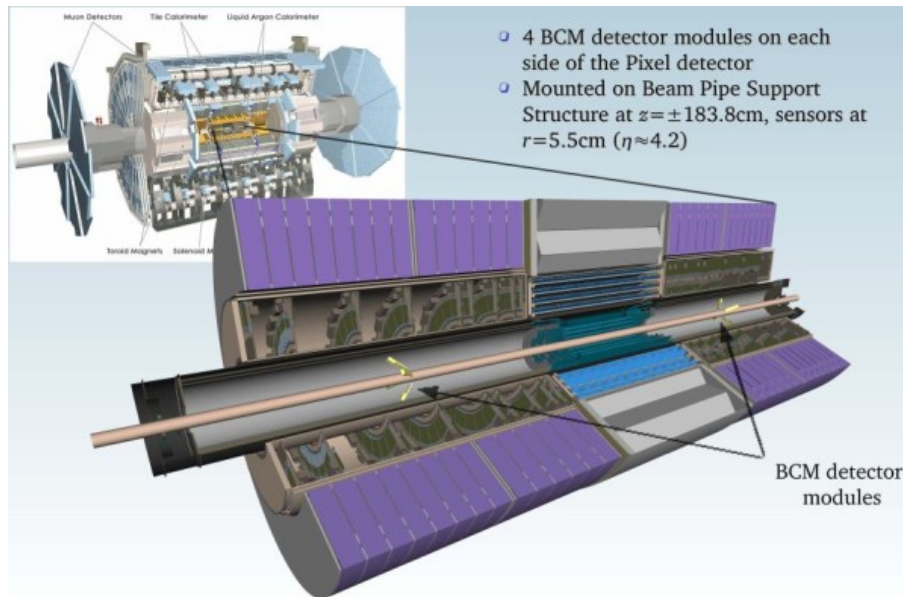


Figure 3.1: Beam Condition Monitor [22]

3.1.2 Data

In 2011, the ATLAS experiment collected data of proton-proton collisions at $\sqrt{s} = 7$ TeV. The data can be identified with luminosity blocks which are the unit of time for data-taking (~ 1

minute period). In order to ensure that every analyzer can share the identical events with good quality for the physics analysis, the data are selected further with a common criterion based on the luminosity blocks, which is provided by the ATLAS experiment. The list of luminosity blocks which passes the criterion is called Good Runs List (GRL) [52]. Figure 3.2 and Table 3.2 show the recorded integrated luminosity, and selected ones with a GRL which is used in this analysis. The integrated luminosity used in this analysis is 4.64 fb^{-1} and the uncertainty is 1.8 % [27]. The 2011 data can be classified into 10 periods depending on the condition of the operation and each period is given an alphabet from D-M so that they can be identified. Table 3.2 shows the run numbers and the integrated luminosity which are corresponding to each period.

Total recorded events	~ 1.39 billion
Total recorded integrated luminosity	5.25 fb^{-1}
Integrated luminosity selected by a GRL	4.64 fb^{-1}

Table 3.1: Total recorded events and integrated luminosity in 2011. The integrated luminosity selected by a GRL, which is used in the study, is also shown.

Period	Run numbers	Integrated luminosity selected by a GRL [pb^{-1}]
D (Apr.14-Apr.29)	179710-180481	164.51
E (Apr.30-May.03)	180614-180776	48.23
F (May.15-May.25)	182013-182519	130.93
G (May.27-Jun.14)	182726-183462	502.09
H (Jun.16-Jun.03)	183544-184169	256.48
I (Jul.13-Jul.29)	185353-186493	333.24
J (Jul.30-Aug.04)	186516-186755	223.49
K (Aug.04-Aug.22)	186873-187815	583.27
L (Sep.07-Oct.05)	188902-190343	1387.29
M (Oct.06-Oct.30)	190503-191933	1014.49
Total	–	4643.99

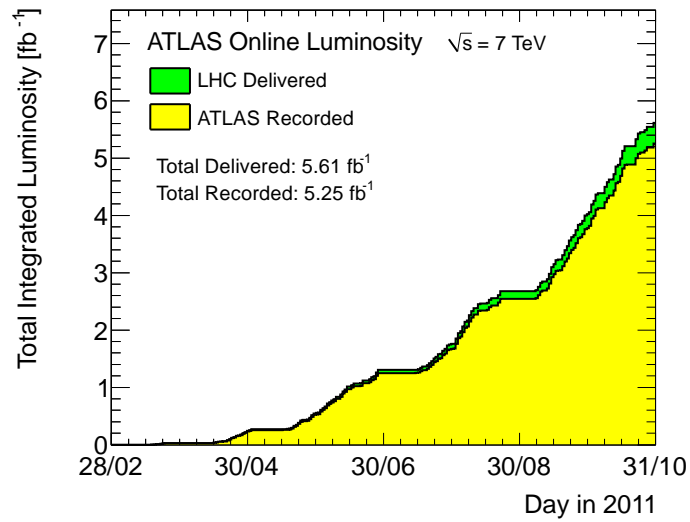
Table 3.2: Run numbers and integrated luminosity in each period.

The ATLAS provides several data streams to make analyses work efficiently, in this study two streams are used. One is dedicated to muons. Each event is selected by at least one muon trigger. The other is dedicated to electrons and each event is selected by at least one electron or photon trigger. When an event has one or more muons and also one or more electrons, the event is recorded in both the two streams. To avoid double counting of the event, a treatment as below is performed in the analysis:

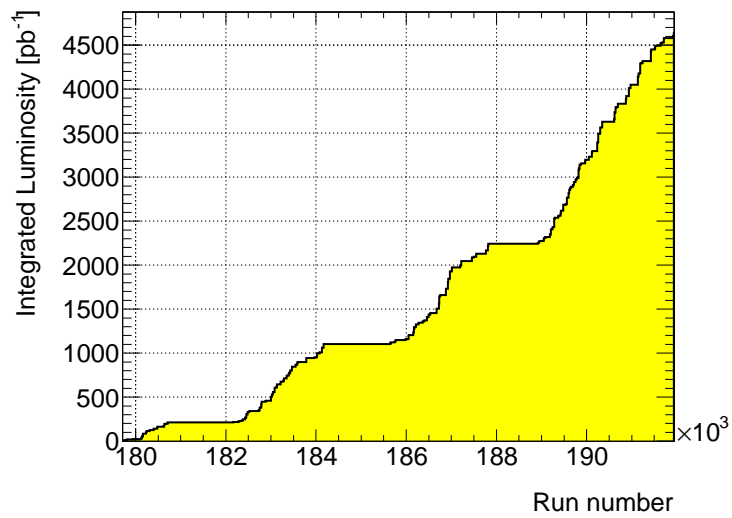
Muons Stream Take events satisfying either below conditions.

- events triggered by both the muon trigger and electron trigger
- events triggered only by the muon trigger

Electrons Stream Take events triggered only by the electron trigger



(a) Cumulative luminosity versus day delivered to (green), and recorded by ATLAS (yellow) during stable beams [53].



(b) Cumulative luminosity versus run selected with a Good Runs List. The luminosity is used in this analysis.

Figure 3.2: Integrated Luminosity in 2011.

3.1.3 Monte Carlo Simulation

Monte Carlo samples are used to estimate the signal acceptance and the backgrounds. They are prepared through the same ATLAS event reconstruction scheme of data to ensure the consistency between data and MC. The procedure are as follows.

- Event generation: This is performed by event generators such as MC@NLO.
- Simulation: The standard simulation performed by the GEANT4 particle simulation package, which simulates the passage of particles through matter [54]. It includes a complete range of functionality including tracking, geometry, physics models and hits.
- Digitization: In this stage, the energy deposition simulated at the previous stage is converted into the information of detector responses.
- Reconstruction: Physics objects such as electrons, muons and E_T^{miss} , are reconstructed by specific algorithms in this stage.

The MC simulation used in 2011 is divided into four periods to reflect the data-taking conditions as closely as possible. The fraction of total represented by different periods is 3.2% for periods B-D, 17.4% for periods E-H, 25.8% for periods I-K and 53.5% for periods L-M. The average number of interactions per bunch crossing for the different periods is shown in Figure 3.3. These conditions are not exactly the same in the recorded data. Therefore they are reweighted in each event to correct the small difference between data and MC in the analysis. Furthermore, in order to reflect more accurate detector performance such as reconstruction of electrons and muons, the scale factors are applied to each event in MC samples.

The generators for the signal sample and background samples that describe past data well are selected as follows.

Signal

The $W^\pm Z$ production processes and subsequent pure leptonic decays are modeled by the MC@NLO version 4.0 [55] event generator with the PDF set CT10 [2], which incorporates the next-to-leading-order (NLO) QCD matrix elements into the parton shower by interfacing to the HERWIG/Jimmy programs [56]. The gauge boson decays into τ leptons are included in the MC event generator and these τ leptons decay to all known final states. The hard gluon emission is treated with an NLO computation and soft/collinear emission is treated with a regular parton shower MC. Full spin correlations and W and Z boson widths are included in the generator.

Backgrounds

Background processes for the $W^\pm Z$ process come from jets produced in association with W^\pm or Z bosons, W^+W^- and ZZ pairs, and top-quark production events. ALPGEN [57] is used to model the $W^\pm/Z + \text{jets}$ and Drell-Yan process for W^\pm/Z bosons decaying to e , μ and τ leptons. Events with multi-jet production from heavy-flavor partons are modeled with PYTHIA B [58]. The W^+W^- and ZZ processes are modeled with HERWIG [59] and PYTHIA [60], respectively. The $W^\pm/Z + \gamma$ and $t\bar{t} + W^\pm/Z$ processes are produced with MADGRAPH [61] or Sherpa [62]. The $t\bar{t}$

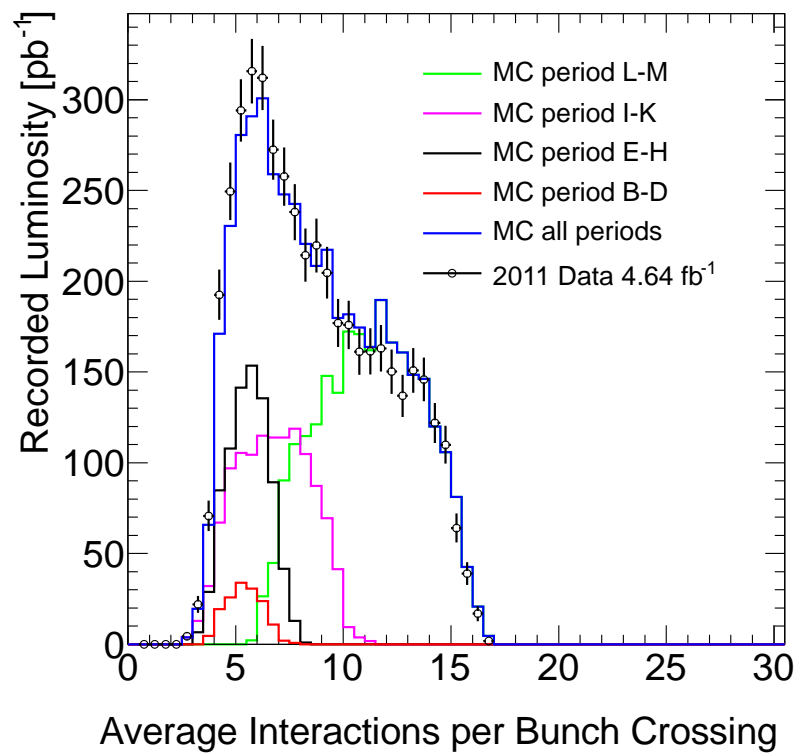


Figure 3.3: The average number of interactions per bunch crossing for the different periods.

and single top quark events are modeled with MC@NLO. Whenever LO event generators are used, the cross-sections are corrected to NLO matrix element calculations.

HERWIG is used to model the hadronization, initial-state radiation and QCD final-state radiation (FSR), except for the samples generated with PYTHIA or MADGRAPH. The two generators use PYTHIA to model them. PHOTOS [63] is used for QED FSR, and TAUOLA [64] for the τ lepton decays.

Since the MC may not model jet fragmentation well, a data-driven method to estimate the Z+jets events and $t\bar{t}$ events is also used for the cross-section and the Triple Gauge Coupling measurements. The more detail is presented in the Section 3.3.

3.2 Event Selection

Events are selected by the cut-based analysis. All final states with electrons and muons for $W^\pm Z$ events are considered, i.e. $\mu^+\mu^-\mu^\pm$, $\mu^+\mu^-e^\pm$, $e^+e^-\mu^\pm$ and $e^+e^-e^\pm$, where the first and second leptons are from the Z boson decay and the third lepton is from W boson decay.

3.2.1 Event Selection Criteria

The event selection criteria are basically determined so that the significance defined as

$$\frac{N_{\text{signal}}}{\sqrt{N_{\text{signal}} + N_{\text{backgrounds}}}} \quad (3.5)$$

is maximum, where N_{signal} and $N_{\text{backgrounds}}$ are the number of the signal and backgrounds events after all selection cuts except the cut itself considered, respectively. The selections are required in the analysis in the order of the list below.

Good Runs List

Events in data are firstly selected based on the Good Runs List which is described in Section 3.1.2. All events in MC, on the other hand, pass this selection.

Trigger Requirement

To obtain $W^\pm Z$ events which decay into muons or electrons as much as possible, the lowest p_T single electron or muon trigger enabled during the corresponding run period is required.

The correspondence relation is shown in Table 3.3. The convention of the naming for triggers is explained in Section 2.4.1.

Primary Vertex Requirement

Events which have the primary vertex reconstructed with at least 3 tracks are selected.

Trigger requirement	electron	muon
period D-I	EF_e20_medium	EF_mu18_inside-out
period J		
period K	EF_e22_medium	EF_mu18_inside-out_medium
period L-M	EF_e22vh_medium1 or EF_e45_medium1	

Table 3.3: Electron and muon triggers that are used in the analysis. The convention of the naming for triggers is explained in Section 2.4.1.

Overlap Removal

Overlapped objects are removed from the event as follows.

- Electrons within $\Delta R < 0.1$ of any selected muon are removed, where $\Delta R = \sqrt{(\Delta\eta)^2 + (\Delta\phi)^2}$.
- If two selected electrons overlap within $\Delta R < 0.1$, the lower p_T electron is removed.
- Jets within $\Delta R < 0.3$ of any selected muon or electron are removed.

E_T^{miss} Cleaning

If jets with $p_T > 20$ GeV which do not overlap ($\Delta R > 0.3$) with a selected lepton pass a bad jet criteria, the event contains the jets is discarded. The bad jet is identified by examining some of the common sources of spurious (noise spikes or coherent noise) or out-of-time (no-collision background and cosmics) energy in the calorimeters.

Event Cleaning

Events with a liquid Argon calorimeter noise are removed. This selection is applied only in data.

Z Mass Requirement

Invariant mass of two leptons of the same flavor and opposite charge is required to be $|M_{ll} - M_{Z,PDG}| < 10$ GeV, where $M_{Z,PDG}$ is the Z boson mass of 91.1876 GeV [25]. When there are more than or equal to two pairs that fulfill the requirement, the one whose invariant mass is the closest to $M_{Z,PDG}$ is taken. Figure 3.4 shows the distribution of the invariant mass before this cut.

Third Lepton Requirement

At least 3 leptons passing the object selection criteria are required. The lepton which is not associated to the Z boson candidate is required to be the Combined (Tight) quality for muon (electron) and to have $p_T > 20$ GeV. The quality for the muon and electron is explained in Section 2.5.2 and 2.5.3, respectively. If there are more than or equal to two candidates that fulfill the requirement, the one with the highest p_T is taken.

E_T^{miss} Requirement

E_T^{miss} in the event is required to have larger than 25 GeV. Figure 3.5 shows the distribution of the E_T^{miss} before this cut for each channel.

W Transverse Mass Requirement

The transverse mass of the W boson M_T^W is required to have $M_T^W > 20$ GeV. The M_T^W is defined as

$$M_T^W = \sqrt{2p_T^l E_T^{\text{miss}}(1 - \cos(\Delta\phi))}. \quad (3.6)$$

Figure 3.6 shows the distribution before this cut for each channel.

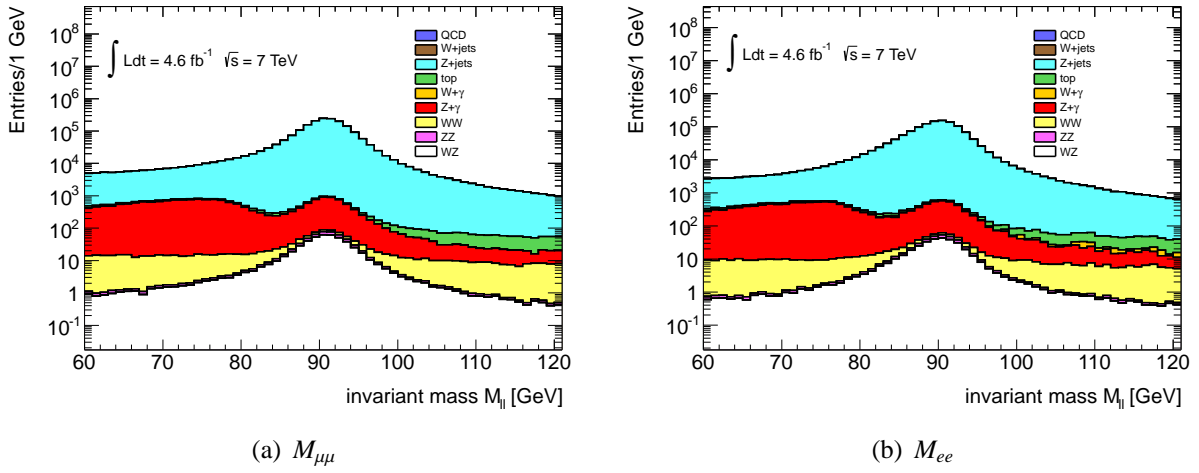


Figure 3.4: Invariant mass of two leptons which are the closest to the Z mass in the event. These distributions are the ones before the Z mass requirement. (a) is the one of muon pairs and (b) is the one of electrons.

Trigger Matching

At least one of the reconstructed leptons (muon or electron) is ensured that the lepton triggered the event. This is performed by matching the object of corresponding trigger in Table 3.3 with the reconstructed lepton. The requirement for the matching is $\Delta R < 0.1$ for muons and $\Delta R < 0.15$ for electrons, where ΔR is the distance between the reconstructed lepton and the trigger object. The lepton is also required to have $p_T > 20$ GeV for the muon and $E_T > 25$ GeV for the electron. If there are more than or equal to two leptons that fulfill the requirement, the lepton with the highest p_T is taken for the matching.

Corrections with the Scale Factors

To reproduce the real detector performance in MC, the Scale Factors (SF) is applied to items below in MC.

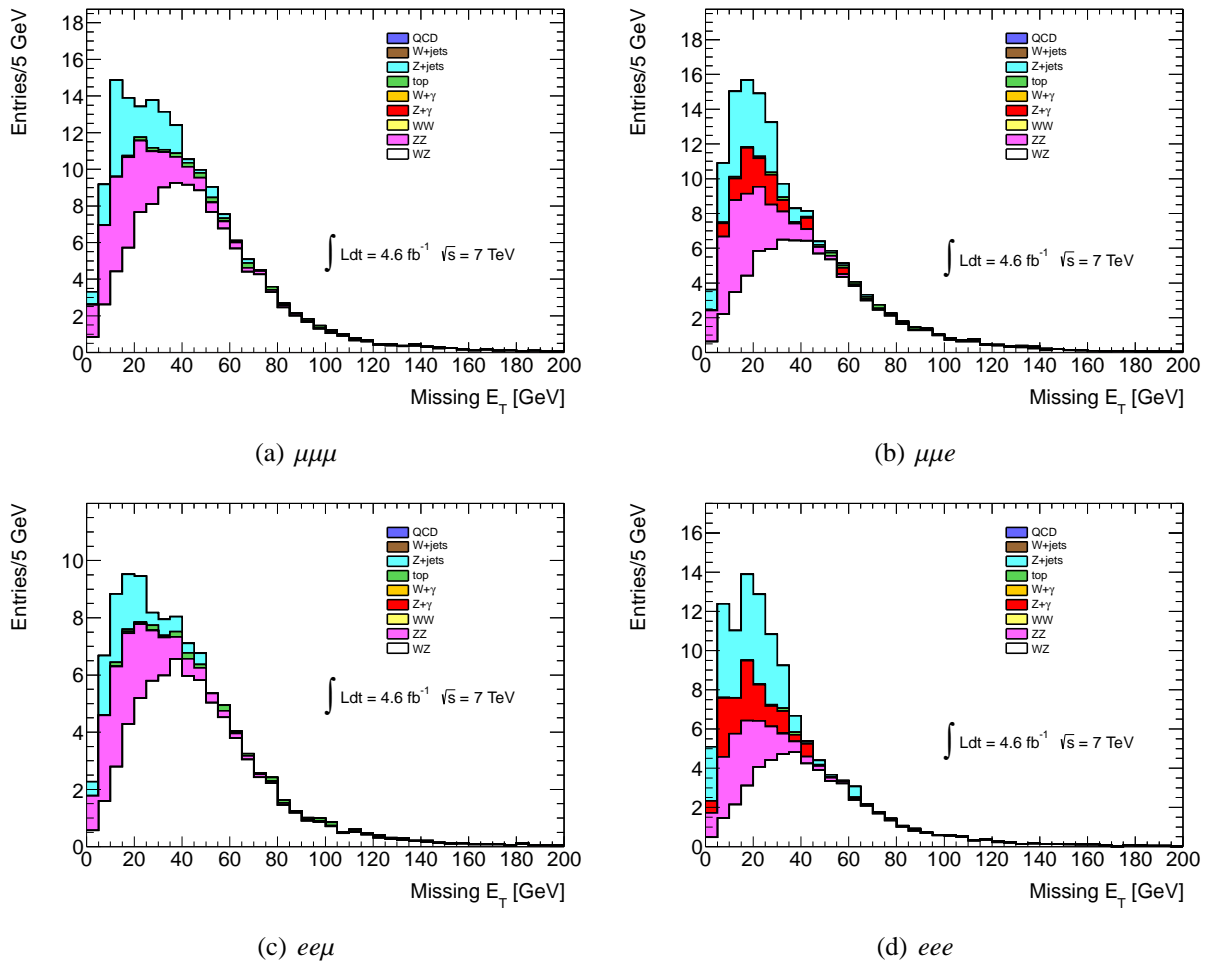


Figure 3.5: Distributions of the E_T^{miss} before the cut.

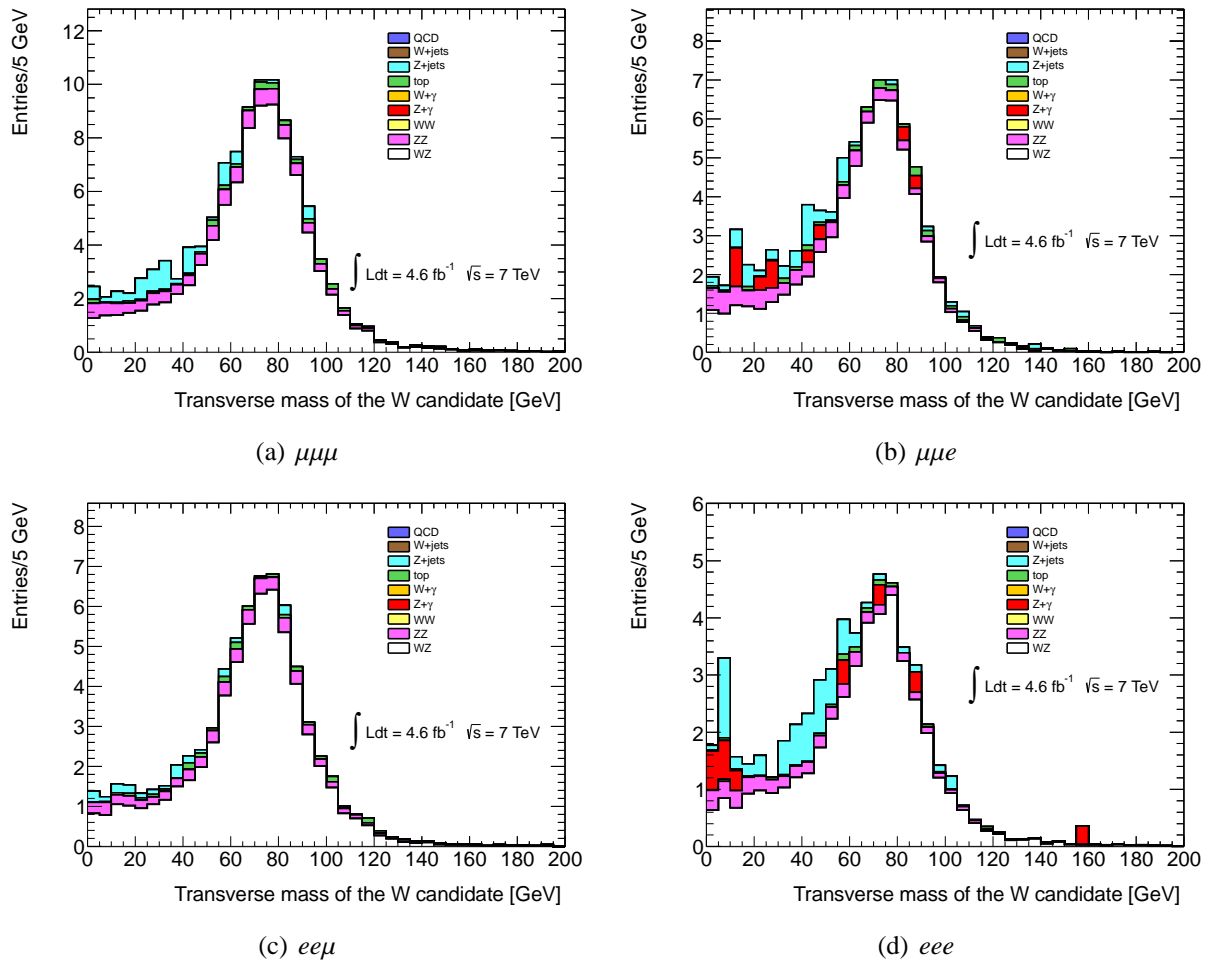


Figure 3.6: Distributions of the transverse mass of the W boson before the cut.

- Reconstruction efficiency for muons
- Reconstruction and identification efficiency for electrons
- Isolation and impact parameter efficiency for muons and electrons
- Trigger efficiency for muons and electrons

The SF for above items except the trigger efficiency is defined as

$$\text{SF} = \frac{\varepsilon_{\text{Data}}}{\varepsilon_{\text{MC}}}, \quad (3.7)$$

where $\varepsilon_{\text{Data}}$ is the corresponding efficiency measured in data and ε_{MC} is the one measured in MC. For the trigger efficiency, the SF depends on the lepton flavor and the number of leptons. Therefore it is defined as

$$\text{SF} = \frac{1 - \prod_{k=1}^N (1 - \varepsilon_{\text{Data}}^k)}{1 - \prod_{k=1}^N (1 - \varepsilon_{\text{MC}}^k)}, \quad (3.8)$$

where N is the number of leptons coming from W^\pm and Z which pass the p_T cut required in the trigger matching selection, $\varepsilon_{\text{Data}}^k$ and $\varepsilon_{\text{MC}}^k$ are the trigger efficiency for the lepton flavor of k -th lepton. Figure 3.7 shows the SF of reconstruction efficiency for muons. Figure 3.8 shows the SF of reconstruction and identification efficiency for electrons. Figure 3.9 shows the SF of isolation efficiency. Figure 3.10 to 3.14 show the muon and electron trigger efficiency for a calculation of the SF.

Objects selection described in Section 3.2.2 is performed after the event cleaning.

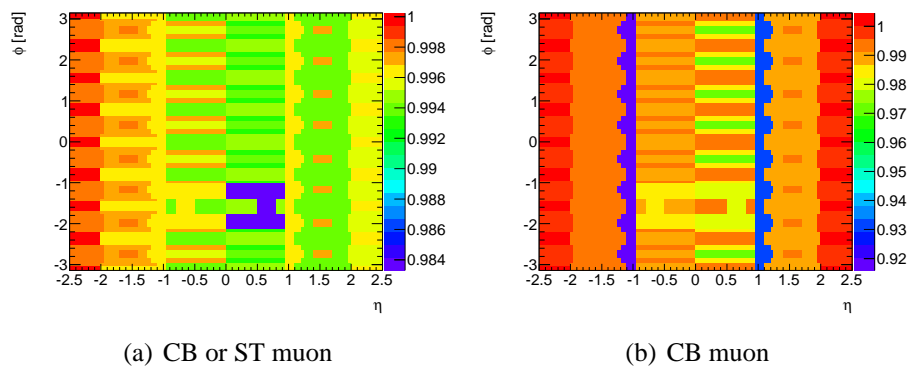


Figure 3.7: Scale Factor of the muon reconstruction efficiency. They are measured in ten regions for each side as described in Section 2.3.5.

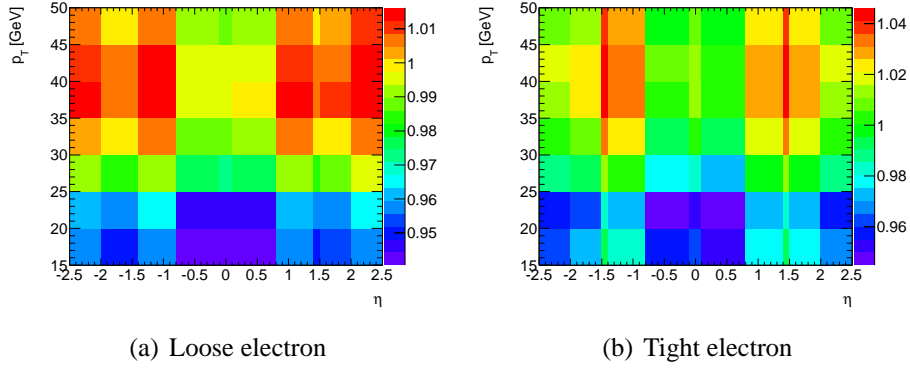


Figure 3.8: Scale Factor of the reconstruction and identification efficiency for electrons.

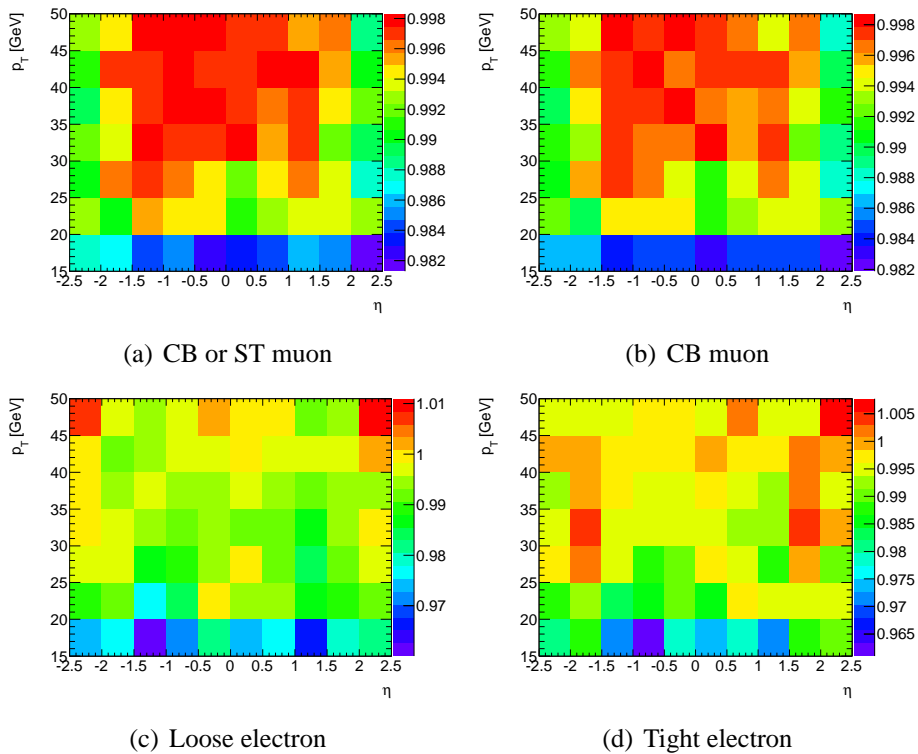


Figure 3.9: Scale Factor of the isolation efficiency.

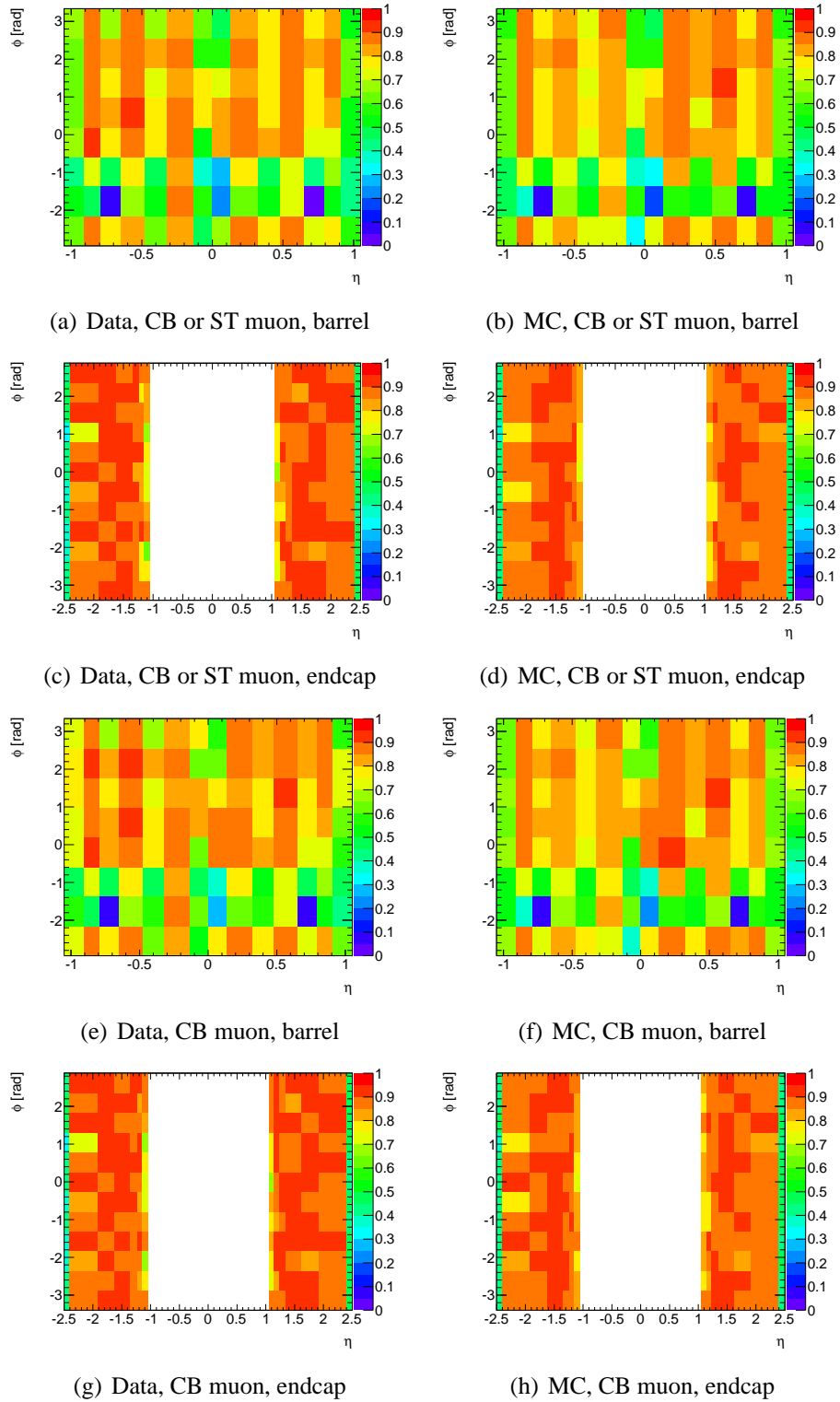


Figure 3.10: Trigger efficiency of EF_mu18_inside-out for the Scale Factor. (a) to (d) are the ones with respect to the Combined or Segment-Tagged muon, while (e) to (h) are the ones with respect to the Combined muon.

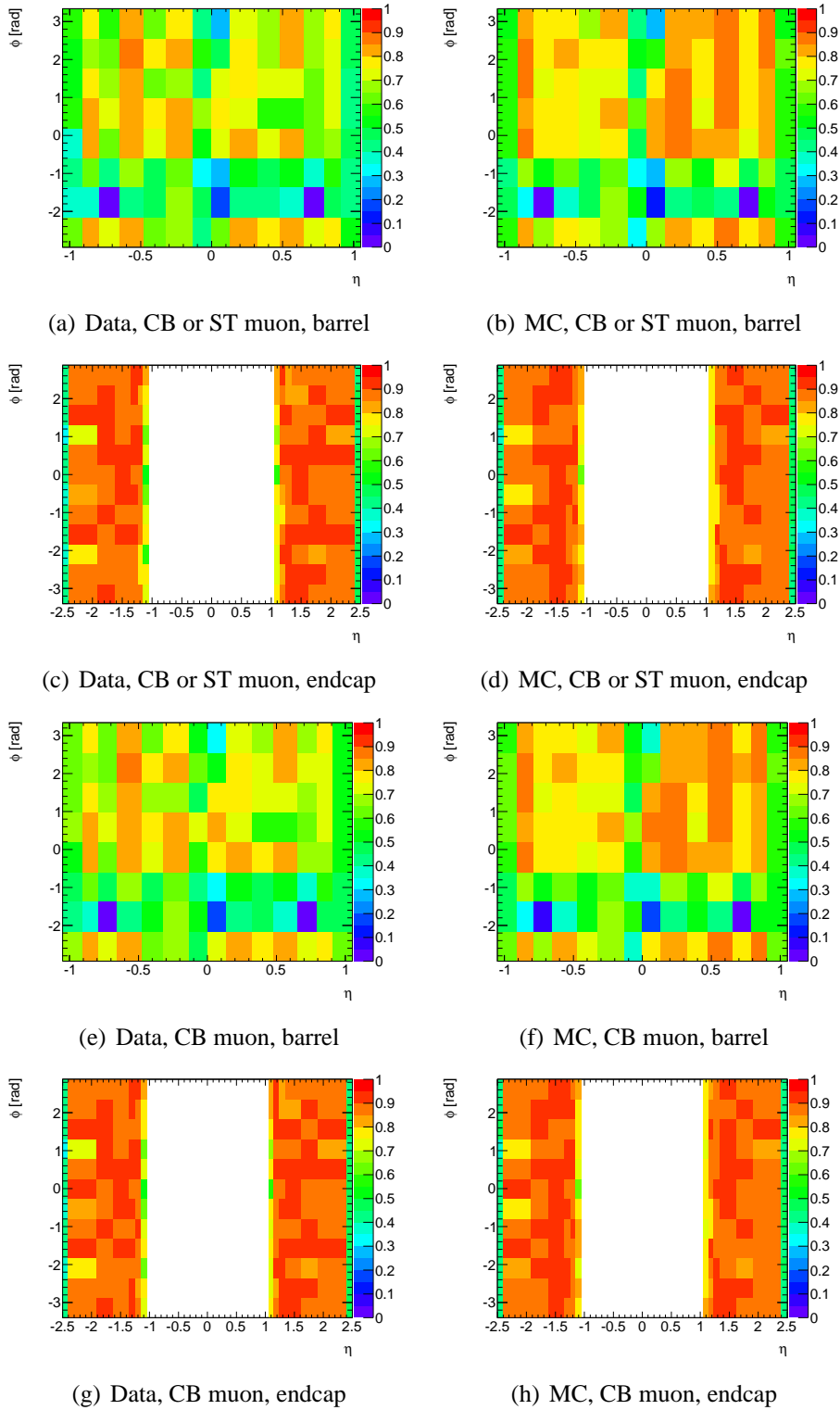


Figure 3.11: Trigger efficiency of `EF_mu18.inside-out_medium` for the Scale Factor. (a) to (d) are the ones with respect to the Combined or Segment-Tagged muon, while (e) to (h) are the ones with respect to the Combined muon.

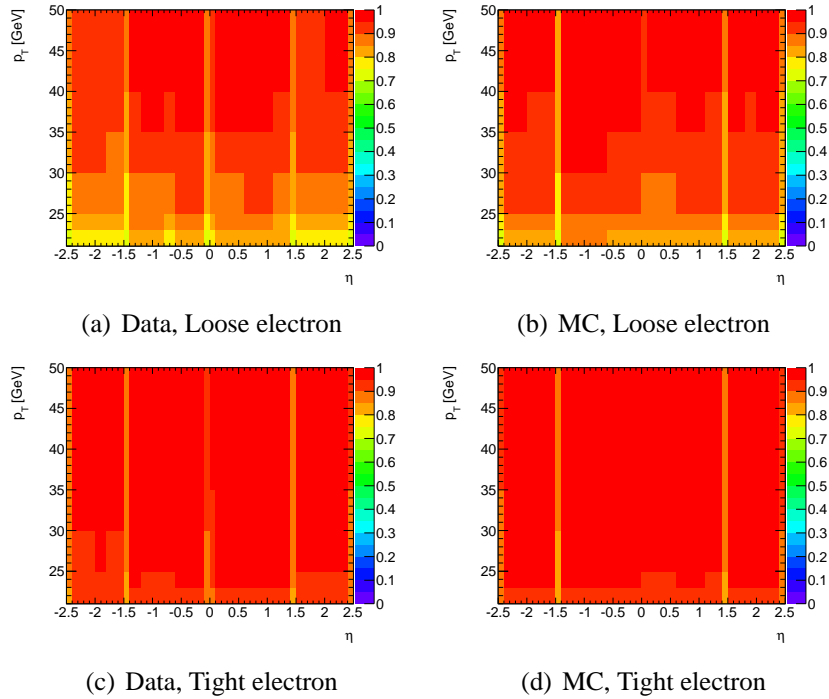


Figure 3.12: Trigger efficiency of EF_e20_medium for the Scale Factor. (a) and (b) are the one with respect to the Loose electron, while (c) and (d) are the ones with respect to the Tight electron.

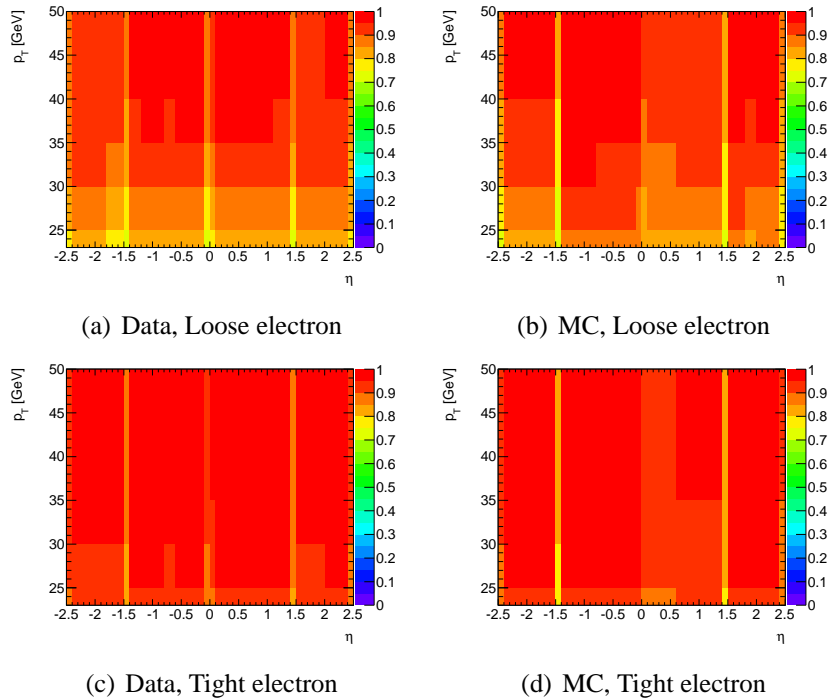


Figure 3.13: Trigger efficiency of EF_e22_medium for the Scale Factor. (a) and (b) are the one with respect to the Loose electron, while (c) and (d) are the ones with respect to the Tight electron.

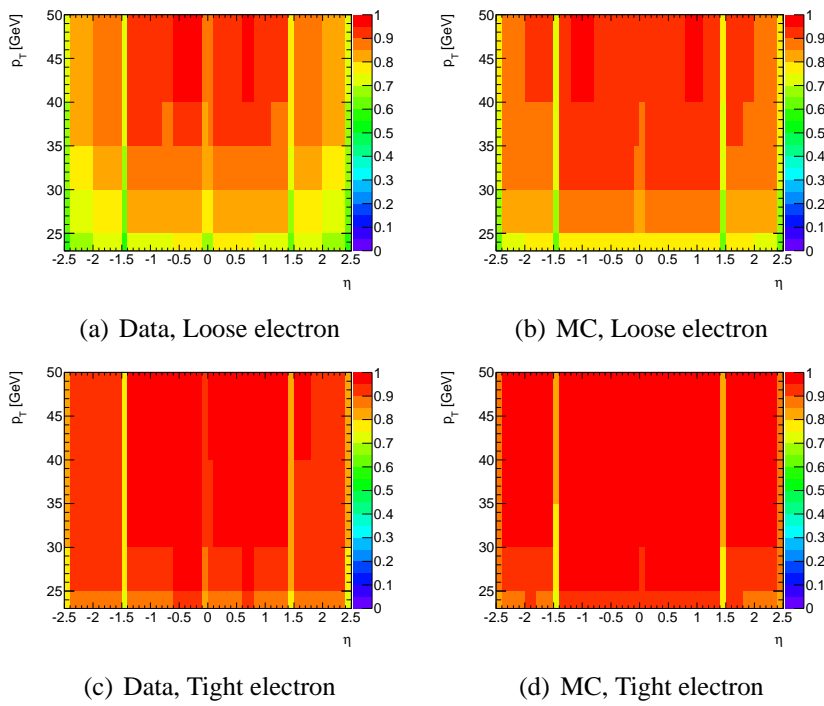


Figure 3.14: Trigger efficiency of EF_e22vh_medium1 for the Scale Factor. (a) and (b) are the one with respect to the Loose electron, while (c) and (d) are the ones with respect to the Tight electron.

3.2.2 Object Selection Optimization

The main objects needed to reconstruct a $W^\pm Z$ event are E_T^{miss} , muons and electrons. Although hadronic jets are also used, they are only for cleaning purposes.

Background Rejection with the Isolation

Jets that fake electrons can be a significant background for the $W^\pm Z$. In order to get better S/N, it is important to reduce such objects. One of powerful ways of reducing fake objects is requiring small amount of activity around the electron to be considered as the one decaying from a W or Z boson. This method is called isolation. The isolation criteria should be different from physics processes, that is why an optimization for $W^\pm Z$ is needed. There are mainly two types of the isolation methods. One is to use tracks around the electron, called tracking isolation hereafter. The other way is to use energy deposits in the calorimeter around the electron, called calorimetric isolation hereafter [65].

The calorimetric isolation computes the reconstructed energy in a cone of half opening angle R around the electron candidate direction. The energy of electron itself is not included in the calculation. Figure 3.15 shows a schematic view of the cone around the electron. While a larger cone will contain more energy in case of misidentified jets, a smaller cone is more robust against energy depositions from pile-up events.

The tracking isolation computes the sum of scalar p_T of tracks in a cone of R around the electron. In contrast to the calorimetric isolation, neutral particles do not contribute to this quantity. Low p_T tracks ($p_T < 1$ GeV) and ones which are not reconstructed are also not included in the calculation. Thus the rejection power is weaker than the calorimetric isolation. The advantage of the tracking isolation, however, is that the contribution from tracks associated with different vertices can be rejected by applying the track quality criteria. Thus the tracking isolation is robust against the pile-up.

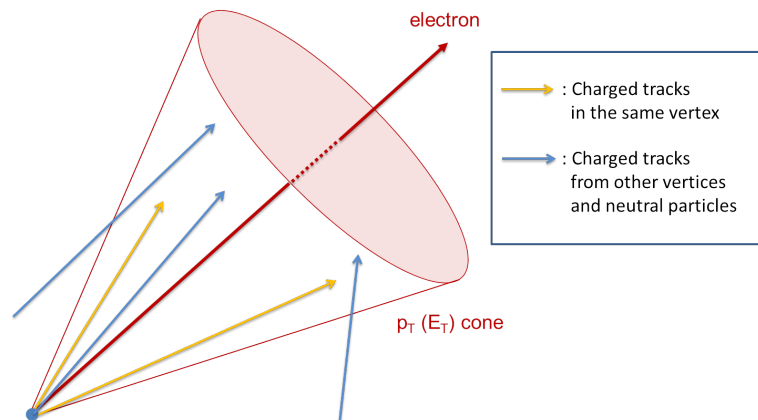


Figure 3.15: Isolation cone. While only the charged tracks (orange arrows) in the same vertex are mainly used in the tracking isolation, tracks coming from other vertices or neutral particles (blue arrows) also contribute to the calorimetric isolation.

One of main backgrounds for $W^\pm Z$ process is Z +jets events. The Z +jets event can have

non isolated lepton, and the lepton can be misidentified as the one coming from the W boson. In that case the event is regarded as a $W^\pm Z$ event. In order to reduce those events, one needs to find reasonable isolation variables and the values. To find them, isolation efficiencies and background rejection efficiencies which are defined as below are measured with Z +jets event candidates using the Tag-and-Probe method. The Tag-and-Probe method is described in Section 2.4.1. If the leptons derived from Z +jets events are categorized into four groups as shown in Table 3.4, one can define the isolation efficiency for isolated electrons and the background rejection efficiency for non isolated electrons as below.

	$E_T^{\text{miss}} < 25 \text{ GeV}$	$E_T^{\text{miss}} \geq 25 \text{ GeV}$
Probe leptons of Z boson	B	A
Leptons of non Z boson	C	D

Table 3.4: A matrix for determination of the isolation variables and their values. Events with Z boson candidate are selected. The Z boson candidate is identified when two leptons in the event has an invariant mass $|M_{ll} - M_{Z,PDG}| < 10 \text{ GeV}$. Remaining leptons are identified as the ones of non Z boson.

$$\varepsilon_{\text{iso}} = \frac{\text{The number of electrons in the region A passing the isolation requirement}}{\text{All electrons in the region A}} \quad (3.9)$$

$$\varepsilon_{\text{rejection}} = 1 - \frac{\text{The number of electrons in the region C passing the isolation requirement}}{\text{All electrons in the region C}} \quad (3.10)$$

The region A is the signal region. The rejection efficiency $\varepsilon_{\text{rejection}}$ is defined by using the region D since leptons from W boson exist in the region D. The reasonable isolation cuts are the one where the $\varepsilon_{\text{rejection}}$ is high as much as possible while keeping the ε_{iso} high. Here consider four types of isolation variables with three different cone sizes as below.

- absolute calorimetric isolation: E_T -cone($R = 0.2$ or 0.3 or 0.4)
- absolute tracking isolation: p_T -cone($R = 0.2$ or 0.3 or 0.4)
- relative calorimetric isolation: $\frac{E_{T\text{-cone}(R = 0.2 \text{ or } 0.3 \text{ or } 0.4)}}{E_T}$
- relative tracking isolation: $\frac{p_{T\text{-cone}(R = 0.2 \text{ or } 0.3 \text{ or } 0.4)}}{p_T}$

The energy used in the calorimetric isolation is corrected to reduce the pile-up effect. Figure 3.16 shows that the isolation efficiency versus the rejection efficiency of electrons for each variable with three different cone sizes. They show that the cone size 0.3 is the best trade-off variable at the region where the isolation efficiency is high. Furthermore, they also show that the relative cone isolation variable has better performance than the absolute cone isolation. Figure 3.17 shows a comparison between the relative isolations and an adopted point for the electron selection.

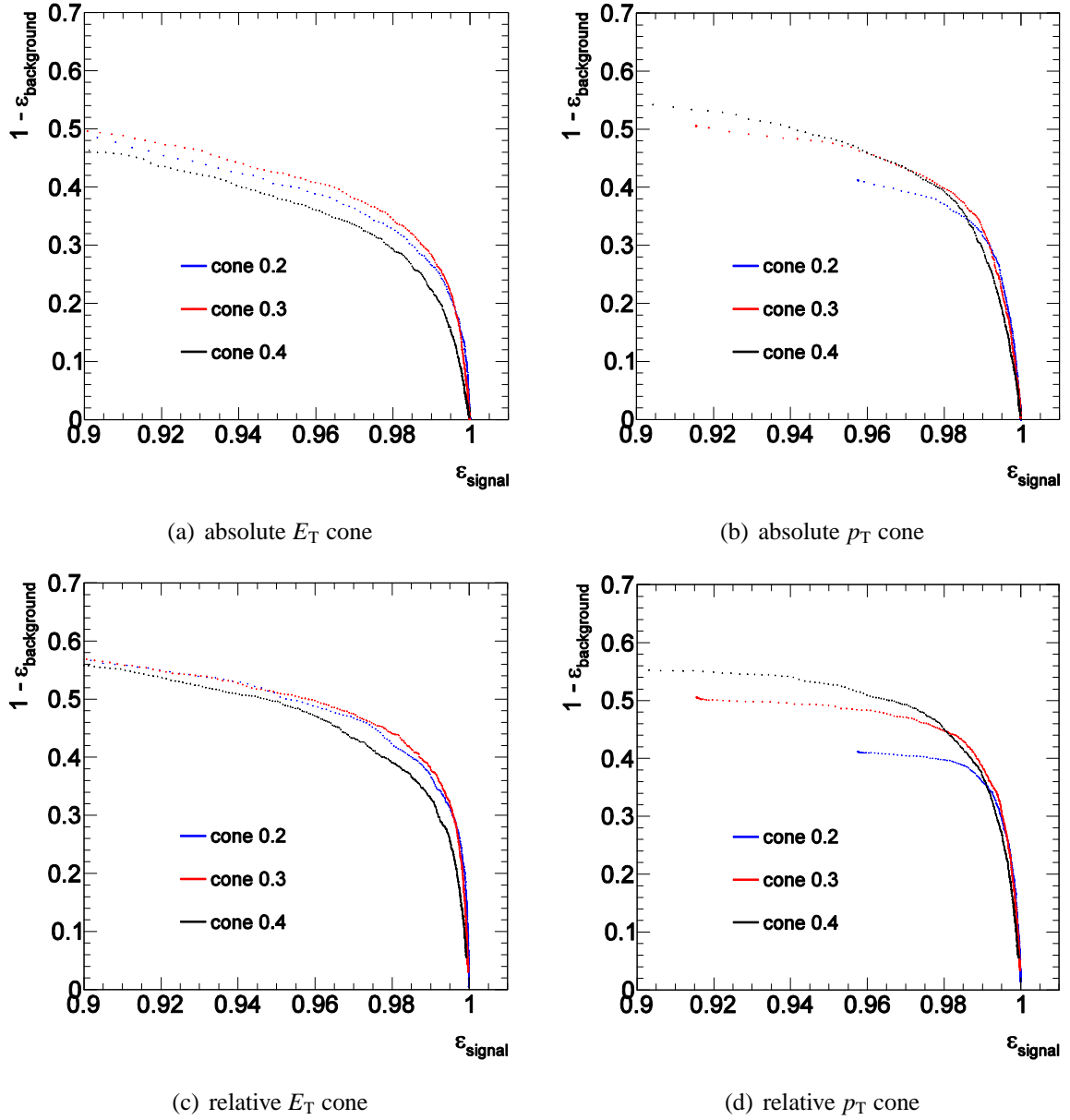


Figure 3.16: Isolation efficiency (x-axis) versus rejection efficiency (y-axis) of four types of isolation variables for electrons with three different cone sizes.

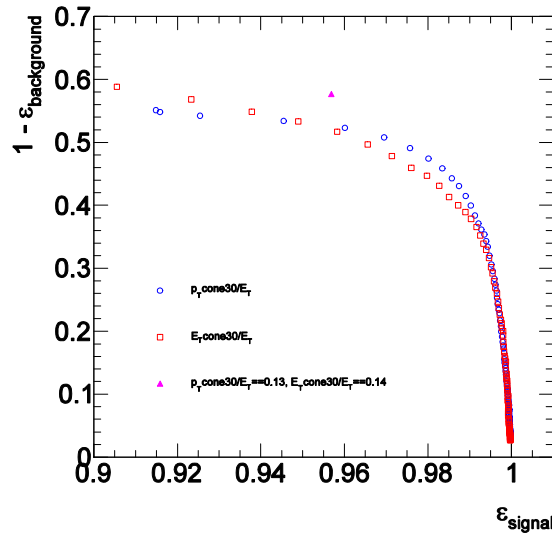


Figure 3.17: Comparison between relative isolations. The magenta triangle is the adopted point used for the electron selection.

Selections of Muons

The reconstructed muons used in this analysis are either Combined (CB) or Segment-Tagged muons (ST), which are described in Section 2.5.2.

The object selection criteria for muons are summarized below.

- CB or ST muons
- $p_T > 15\text{GeV}$.
 - Figure 3.19(a) shows the distribution before the p_T cut.
- As a track quality cut in the Inner Detector,
 - At least one hit in the b-layer of the Pixel layers
 - At least two hits in all Pixel layers
 - At least six hits in the SCT
 - The number of layers in the Pixel and SCT which have no hit made by the track is required to be less than three
 - Quality cut on the TRT is dependent on the η as follows:
 - * If $|\eta| < 1.9$, number of hits and outliers of the TRT is required to be greater than six. And the fraction of $\frac{\text{number of outliers}}{\text{number of outliers and hits}}$ is also required to be less than 0.9
 - * If $|\eta| \geq 1.9$, the fraction of $\frac{\text{number of outliers}}{\text{number of outliers and hits}}$ is required to be less than 0.9 only when the number of hits and outliers is greater than six
- $|\eta| < 2.5$

- $|z_0| < 1\text{mm}$ and $|d_0|/\sigma_{d_0} < 3$.
 - The d_0 and z_0 are defined as the transverse and longitudinal impact parameters as illustrated in Figure 3.18. They are defined with respect to the interaction point unless otherwise mentioned. Figure 3.19(b) and 3.19(c) show their distributions before the cut on the variable displayed.
- $p_{\text{T-cone}}(R = 0.3)/p_{\text{T}} < 0.15$.
 - Figure 3.19(d) shows the distribution before the cut.

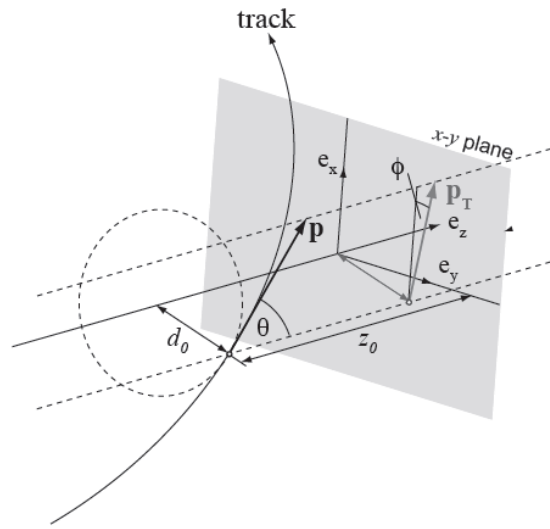


Figure 3.18: The illustration of the d_0 and z_0 . While the d_0 is defined as the transverse impact parameter, the z_0 is longitudinal one. In this thesis, they are defined with respect to the interaction point unless otherwise mentioned [23].

Figure 3.20 and 3.21 show the distribution of muon quantities in the $Z \rightarrow \mu\mu$ sample after these selections.

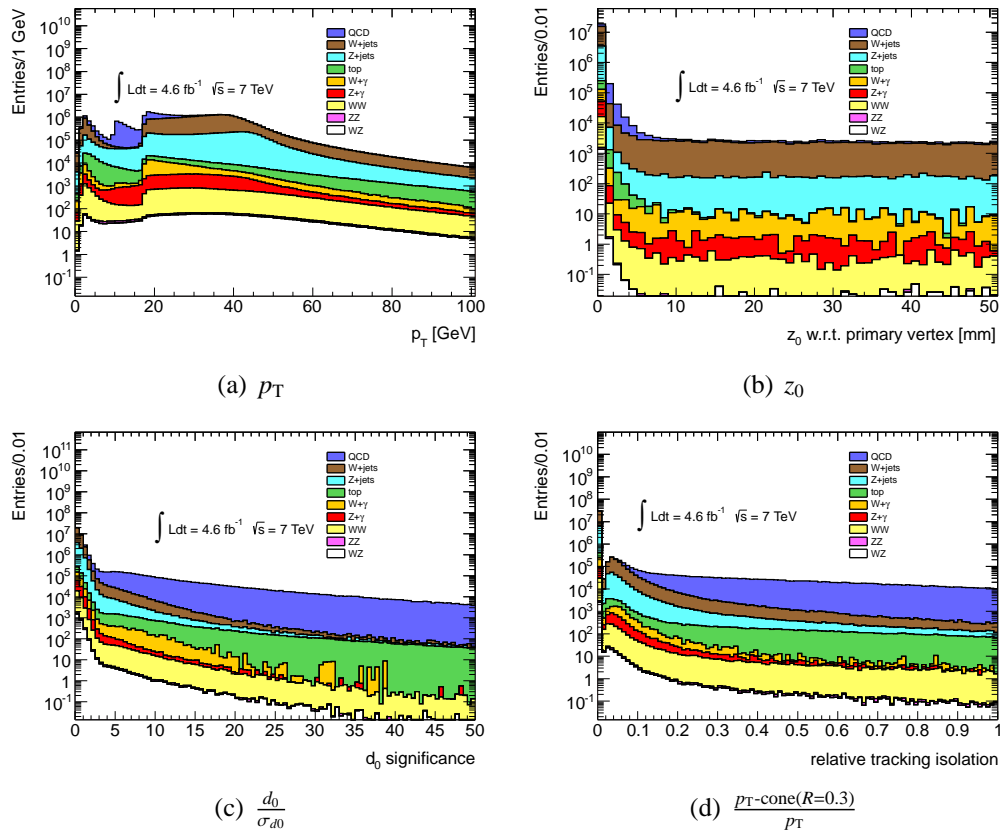


Figure 3.19: Distributions of the variables used for the muon selection before the cut on the variables displayed.

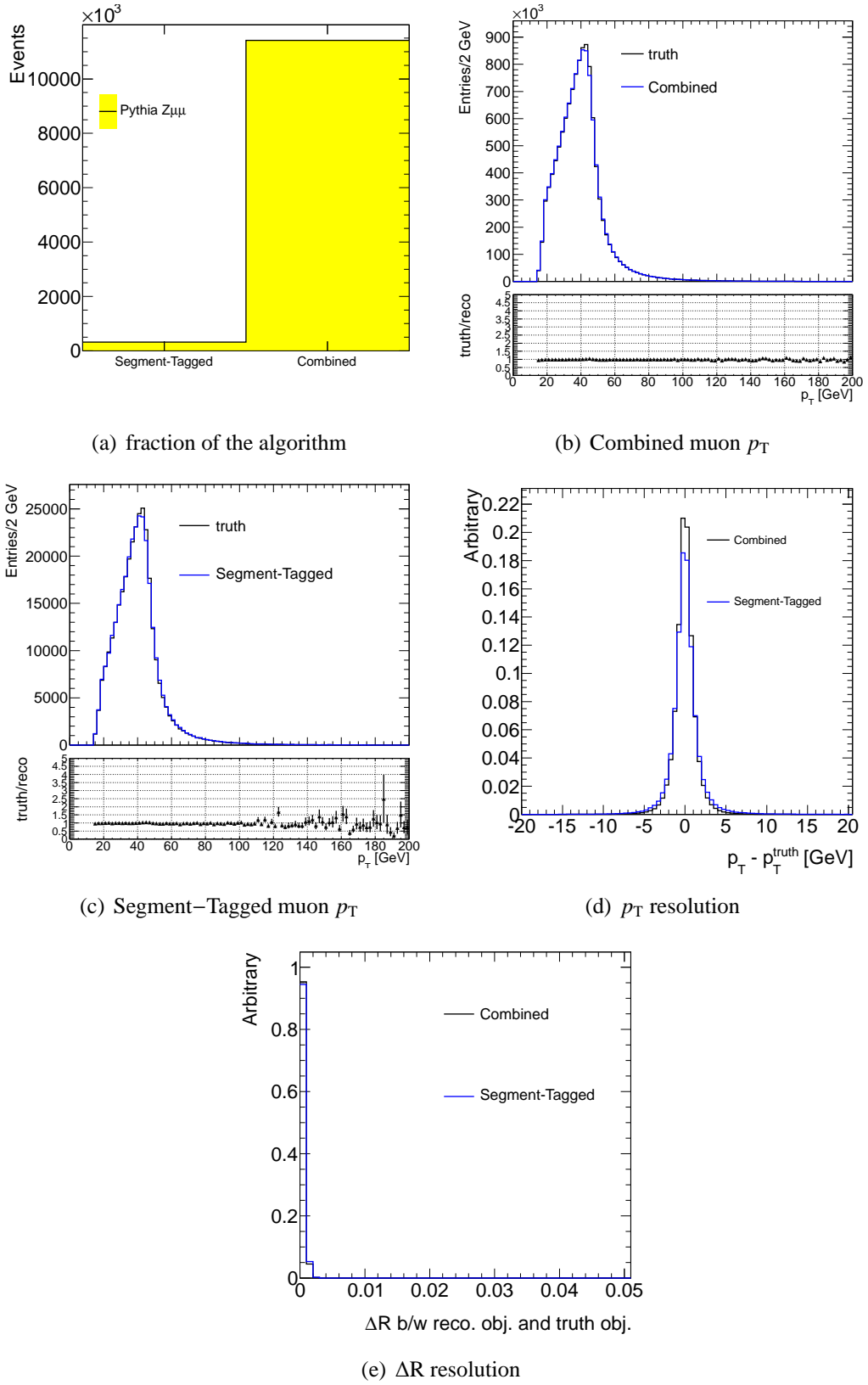


Figure 3.20: Distribution of muon quantities in the $Z \rightarrow \mu\mu$ sample after the selections for muons (1).

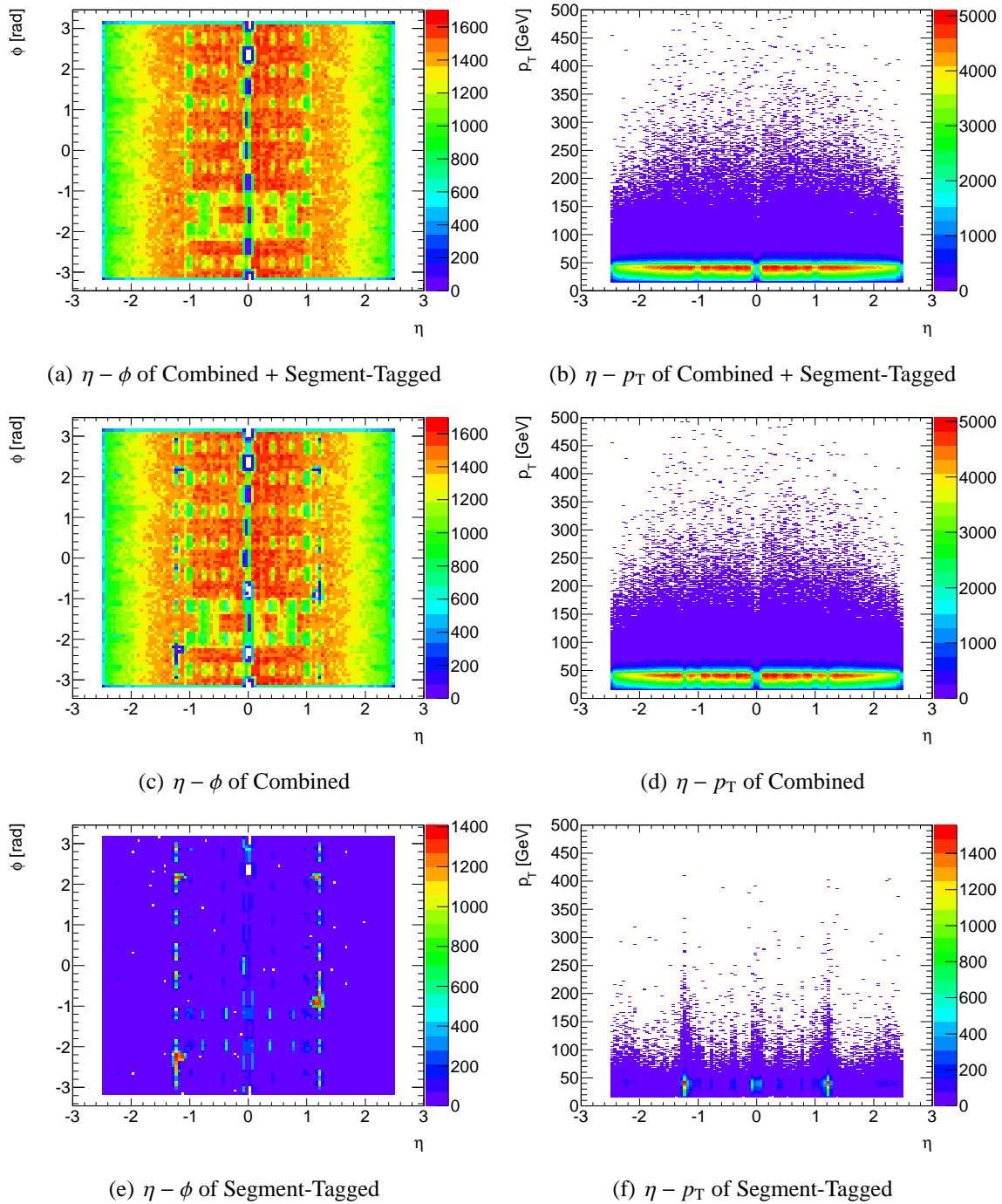


Figure 3.21: Distribution of muon quantities in the $Z \rightarrow \mu\mu$ sample after the selections for muons (2). (a) and (b) are the distribution of CB + ST. The presence of the detector support structure ($\phi \sim -1.5$), magnet support (every $\pi/8$ at $|\eta| \simeq 0.4$ and 0.75), services for the calorimeters ($|\eta| \simeq 0$) can be seen in η - ϕ plane (a). $|\eta| \simeq 1.2$ is the transition region of the magnetic field. Muons around the region are recovered by the Segment-Tagged algorithm (e).

Selections of Electrons

The energy and direction of electrons are measured both in the Inner Detector and the Electromagnetic calorimeter. The η and ϕ measured in the Inner Detector are used if the track has at least 4 Silicon hits (=Pixel hits + SCT hits). Otherwise the ones measured in the calorimeter are used instead. The transverse energy is calculated as,

$$E_T = \frac{\text{cluster energy}}{\cosh(\eta)}. \quad (3.11)$$

Distribution of quantities of the electrons are shown in Figure 3.23.

The η range used in this analysis is chosen carefully to ensure the presence of the Inner Detector tracking coverage and to avoid the transition region between the barrel and the end-cap calorimeters where the energy is not well measured. The object selection criteria for electrons are summarized below.

- Electrons reconstructed with the calorimeter-based algorithm
- Object quality criteria have to be passed
 - In 2011, there was a hardware problem on the liquid Argon calorimeter. The criteria are for avoiding the electron objects affected by the regions or other data quality issues. The effect can be seen in Figure 3.23(d).
- $E_T > 15$ GeV.
 - Figure 3.22(a) shows the distribution before the E_T cut.
- $|\eta| < 1.37$ or $1.52 < |\eta| < 2.47$
- A loose quality of identification for electrons coming from Z bosons is required (A tight quality cut for electrons coming from W boson is required). The qualities are mentioned in Section 2.5.3.
- $|z_0| < 1$ mm.
 - Figure 3.22(b) shows the distribution before the cut.
- $|d_0|/\sigma_{d_0} < 10$
 - Figure 3.22(c) shows the distribution before the cut.
- $E_{T\text{-cone}(R = 0.3)}/E_T < 0.14$ and $p_{T\text{-cone}(R = 0.3)}/E_T < 0.13$.
 - Figure 3.22(d) and 3.22(e) show their distribution before the cut on the variable displayed.

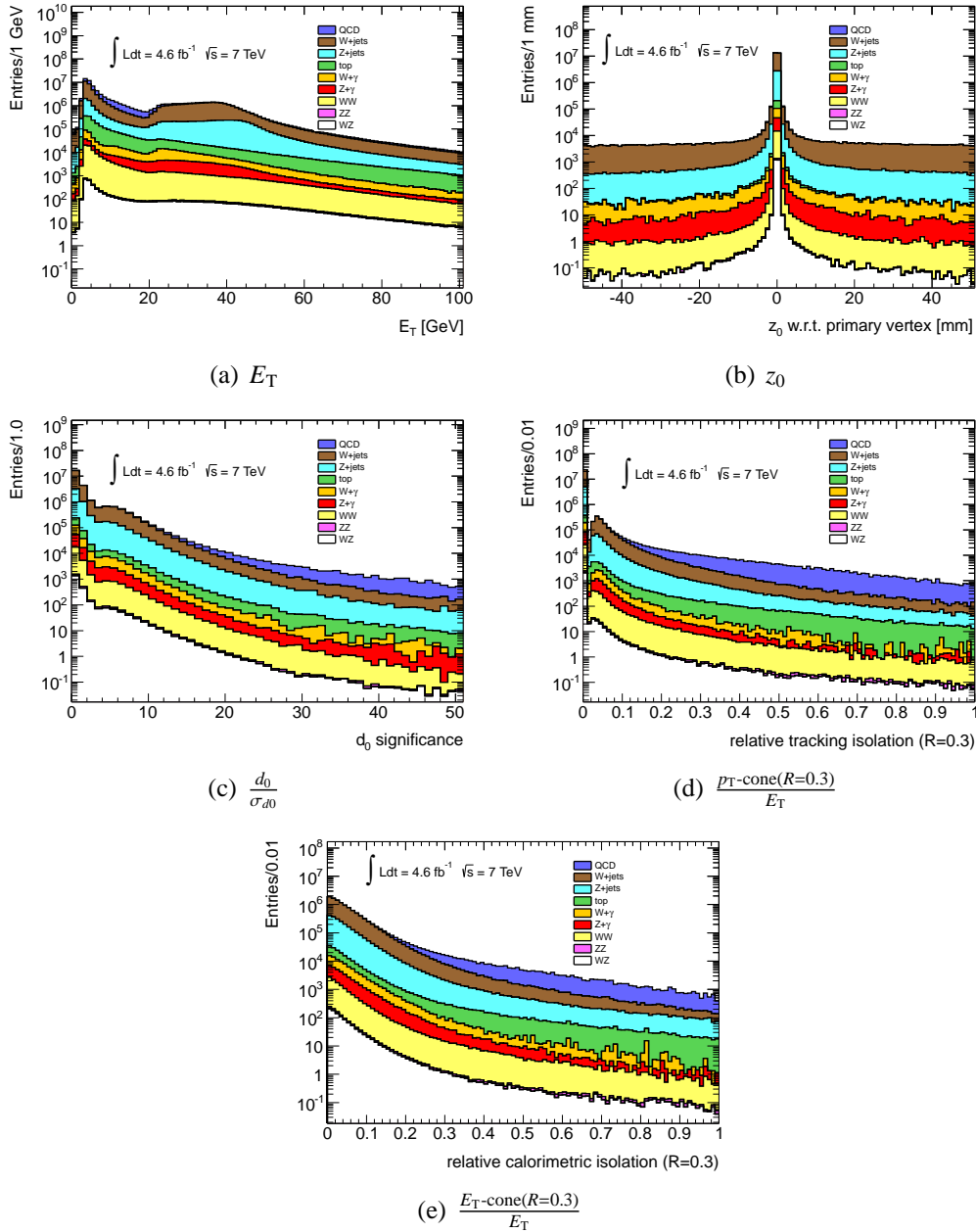


Figure 3.22: Distributions of the variables used for the electron selection before the cut on the variables displayed.

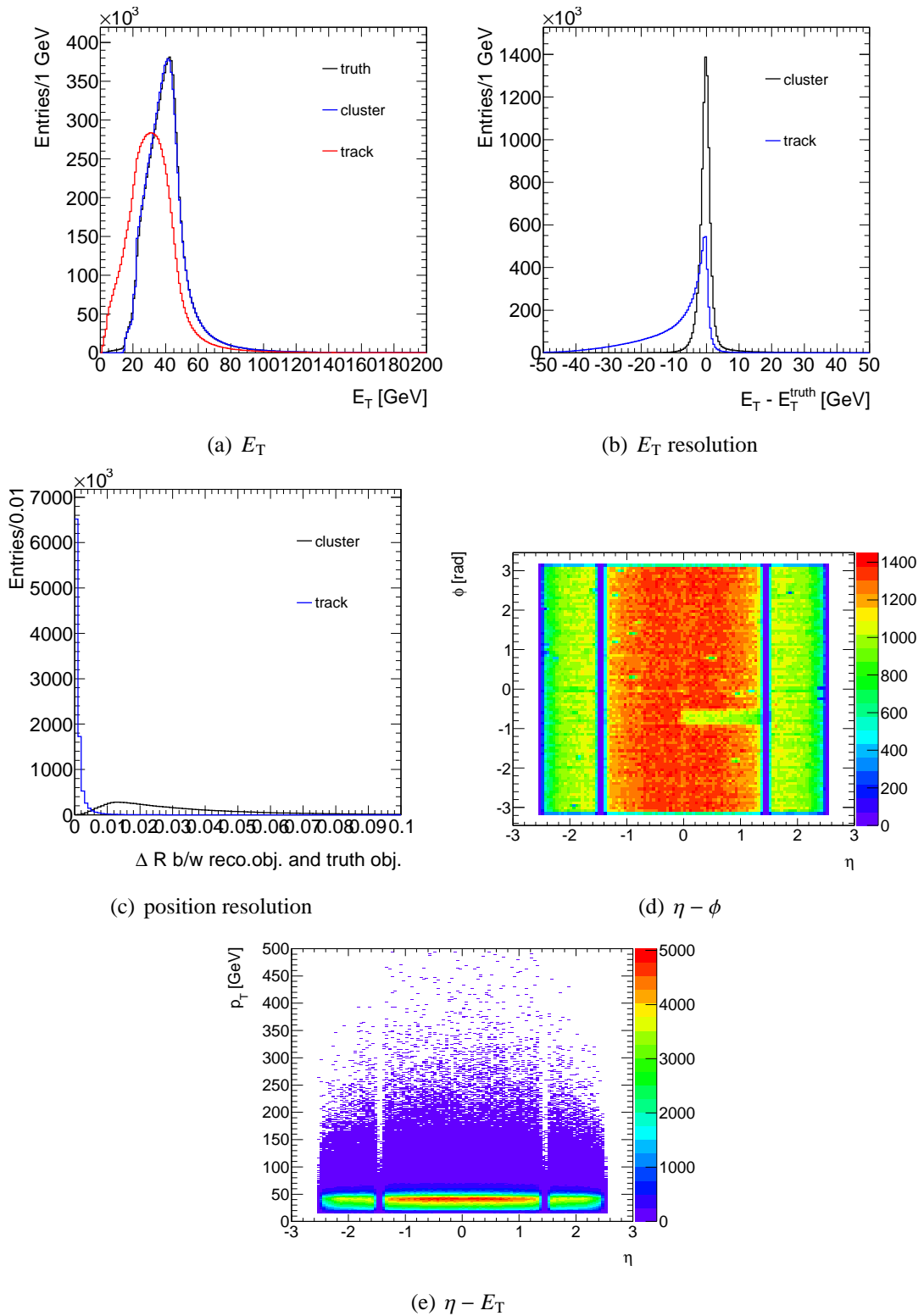


Figure 3.23: Distribution of electron quantities in the $Z \rightarrow ee$ sample after the selections for electrons. (a) E_T (p_T) distributions measured at the calorimeter ("cluster" in the figure), the ID ("track" in the figure) and truth information. The cluster energy is employed for E_T of electrons in this analysis. (c) ΔR distributions between the truth information and the position measured at the calorimeter or the ID. The positions of the ID are employed for the ones of electrons in this analysis.

The number of events at each selection in each channel is shown in Figure 3.24. The expected number of signal events after each selection is shown in Table 3.5. The relative acceptance of signal events after each selection is shown in Table 3.6.

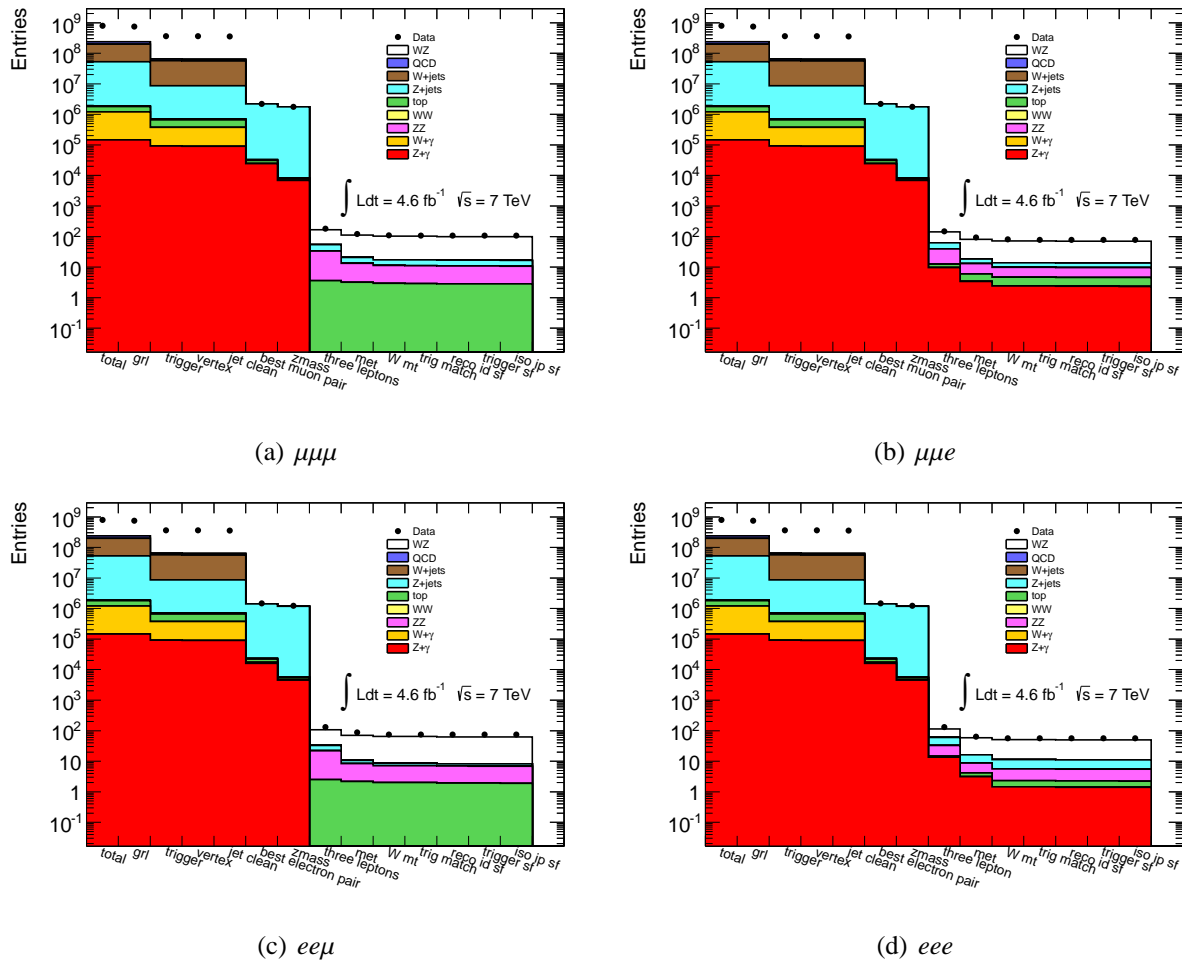


Figure 3.24: The expected number of MC events after each cut and correction. The number of events in data after each cut are also shown.

Cutflow	Events			
	$\mu\mu\mu$	$\mu\mu e$	$ee\mu$	eee
All	1202.26			
Muon or electron trigger	1120.78			
Primary vertex	1117.91			
E_T^{miss} cleaning	1116.16			
Z cut	317.37		218.88	
Three leptons	106.55	74.82	70.55	51.22
E_T^{miss} cut	86.44	59.17	57.00	40.50
$W^\pm M_T$ cut	81.85	55.67	54.05	38.07
Trigger match	81.67	55.29	53.99	38.04
Corrections	78.32	54.20	51.77	37.24

Table 3.5: The expected number of signal events after each cut for $W^\pm Z \rightarrow \ell\nu\ell'\ell'$ for $\mathcal{L} = 4.64\text{fb}^{-1}$. The ℓ and ℓ' are muon or electron. The event in which τ lepton(s) decay into muon(s) or electron(s) is also included.

Cutflow	Acceptance (%)			
	$\mu\mu\mu$	$\mu\mu e$	$ee\mu$	eee
All	100			
Muon or electron trigger	93.22			
Primary vertex	99.74			
E_T^{miss} cleaning	99.84			
Z cut	28.43		19.61	
Three leptons	33.57	23.57	32.23	23.40
E_T^{miss} cut	81.12	79.09	80.80	79.07
$W^\pm M_T$ cut	94.70	94.08	94.82	93.99
Trigger match	99.78	99.31	99.90	99.93
Corrections	95.89	98.04	95.89	97.89

Table 3.6: Relative acceptance of signal events after each cut for $W^\pm Z \rightarrow \ell\nu\ell'\ell'$ events.

3.3 Background Estimation

Major backgrounds in the $W^\pm Z$ process come from the ZZ diboson process, jets associated with Z boson, top quark pair productions ($t\bar{t}$, $t\bar{t} + W$ or Z) and $Z + \gamma$ events. This section describes how to estimate them.

3.3.1 ZZ

ZZ events in which both Z bosons decay leptonically are a major background for all the $W^\pm Z$ channels. The shape of this background is estimated from MC simulation by applying the selections described in Section 3.2.1 and 3.2.2 with the corrections. Each ZZ event which passes the $W^\pm Z$ selection has E_T^{miss} greater than 25 GeV. In the case, the value of E_T^{miss} comes mainly from a lepton which is outside the fiducial acceptance of the detector. Figure 3.25 shows the η distributions of truth muons and electrons which are not detected. As described in 2.3.5, muon spectrometer covers $|\eta| < 2.7$ and has a gap around $|\eta| = 0$ for services. If a muon traverses the region, the muon does not deposit its energy in the calorimeter and can cause large E_T^{miss} . The η distribution of electrons show peaks at $|\eta| \sim 1.4$, which corresponds to the transition region between the calorimeters.

The total number of events is determined by scaling the shape of distribution according to the theoretical cross-section and the measured luminosity.

3.3.2 $Z + \gamma$

Leptonic decays of Z bosons produced in association with photons can be identified as tri-lepton event if a photon converts into an electron-positron pair. This process is simulated in MADGRAPH generator, together with the simulation programs PYTHIA for the hadronization. PHOTOS, TAUOLA and GEANT4 are for the detector simulation of photon conversions.

3.3.3 $t\bar{t}$

Top quarks can produce multiple leptons thorough subsequent leptonic decays of W bosons and semi-leptonic decays of bottom quarks. Besides that, particles within jets produced in hadronic decay of W boson can also be identified as electrons. Most of those events can be removed by requiring isolation cuts and the impact parameter cuts for leptons which come from the b quark or light quark jets. On the other hand, those reconstructed leptons may not be well modeled in MC, therefore a data-driven method is preferred to estimate the events. According to the MC, however, approximately only three $t\bar{t}$ events remain after all selection cuts and it indicates that full data-driven estimate is difficult to perform due to the low statistics. That is why a data driven correction is applied to the $t\bar{t}$ events instead of the full data-driven method. In order to provide a correction factor, $t\bar{t}$ enriched control sample needs to be defined. As the control region, the same sign of leptons for Z candidate selection is chosen instead of the opposite sign pairs. Since $t\bar{t}$ events do not contain an actual Z boson, their distribution is not affected from the requirement. Figure 3.26(a) and 3.26(b) show them, which are the distributions of the invariant mass and the E_T^{miss} for the signal sample and the control sample.

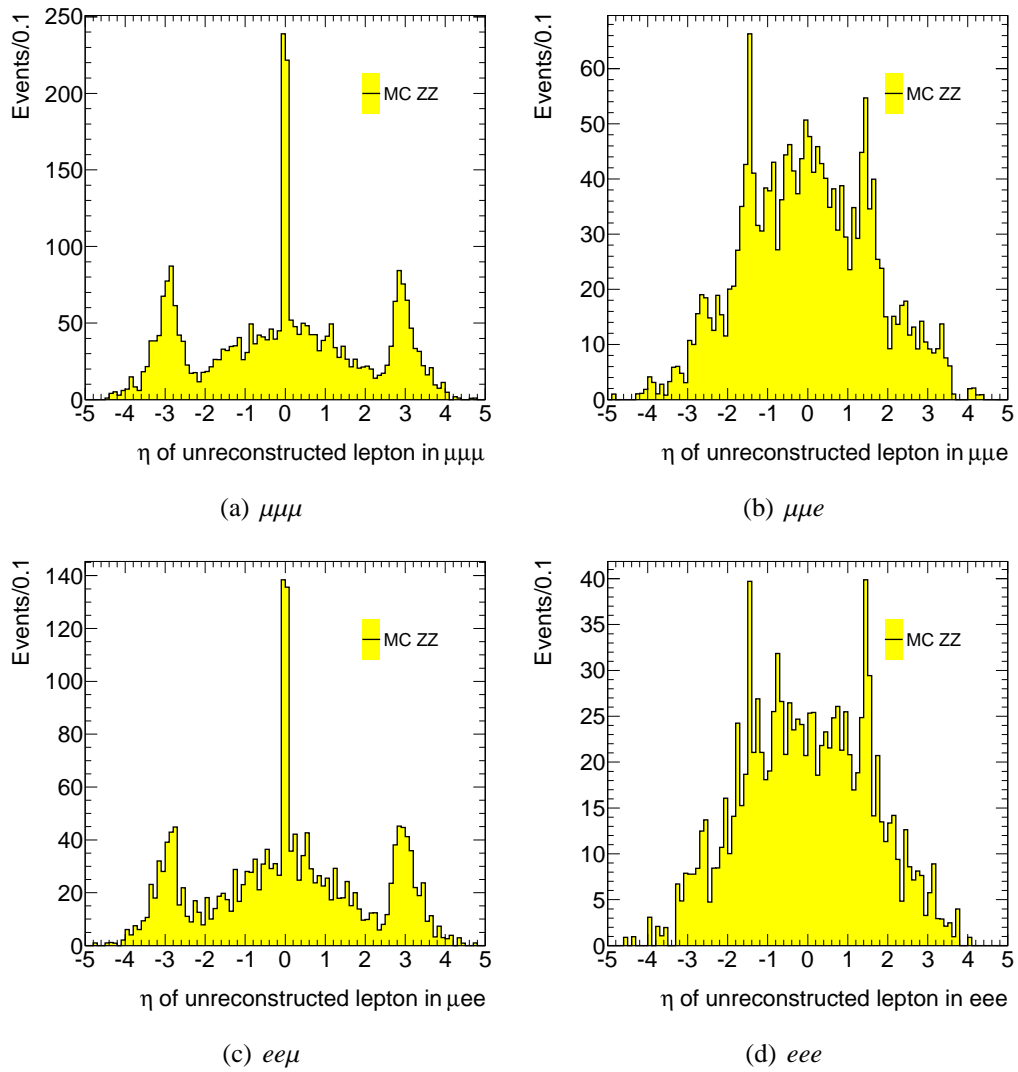


Figure 3.25: Missing leptons in ZZ . p_T of each truth lepton is greater than 15 GeV.

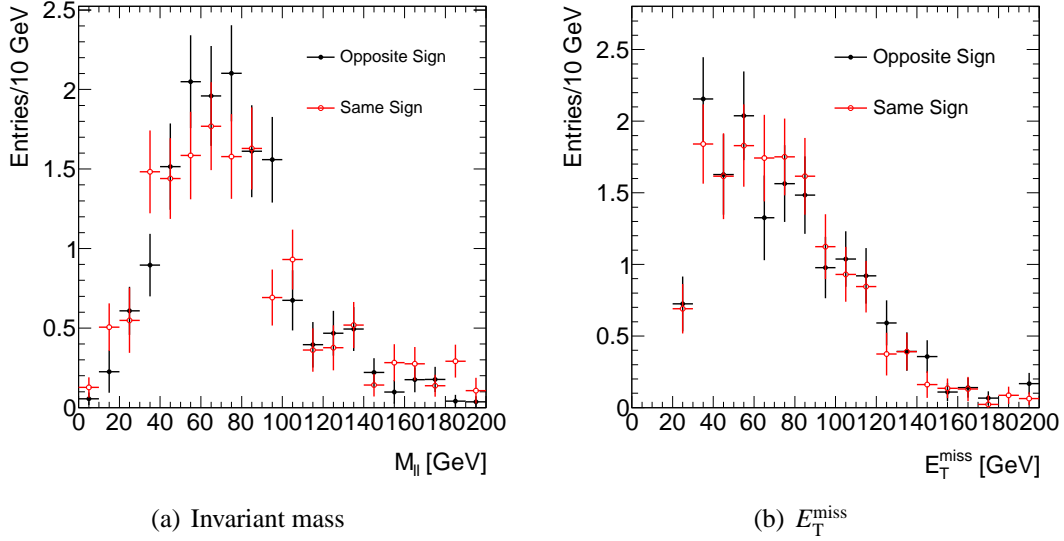


Figure 3.26: (a) Invariant mass distribution for the lepton pair closet to the Z boson mass after all selection cuts except the Z mass cut in $t\bar{t}$ simulation sample. (b) E_T^{miss} distribution after all selection cuts except the Z mass cut in $t\bar{t}$ simulation sample.

Figure 3.27(b) and 3.27(a) show the distribution of E_T^{miss} when the same sign lepton pairs are required. They show that only the $t\bar{t}$ is main component. The region where the purity of $t\bar{t}$ events is greater than 80 % is $E_T^{\text{miss}} < 200$ GeV for $e\mu\mu$, $60 \text{ GeV} < E_T^{\text{miss}} < 200$ GeV for $ee\mu$. These range are used to estimate the correction factor. The ratio of data to MC is 2.06 ± 0.77 for $\mu\mu e$ and 2.32 ± 1.13 for $ee\mu$ and the final correction factor is determined as 2.2 with an uncertainty of 1.0.

Apart from the $t\bar{t}$ estimate mentioned above, the $t\bar{t}$ associated with a weak boson event is considered separately. Since both $t\bar{t} + W^\pm$ and $t\bar{t} + Z$ have real three leptons unlike the event of $t\bar{t}$ only, those events are easy to pass the selections compared to the one including non-isolated lepton or the lepton derived from b-quark. Therefore non-negligible events can remain in spite of very low production cross-section. These events are estimated with MC.

3.3.4 Z+jets

Z+jets events are another main background to the $W^\pm Z$ events. These events can contain a third lepton from heavy-flavor quark decays or muons from in-flight decays of pions and kaons. While leptons from the decay of Z bosons are primarily isolated, leptons from bottom or charm quark decays tend to be spatially correlated with jets. That is why leptons originated from hadronic decays can be removed by isolation requirements. In order to estimate the Z+jets events, a full data-driven method is employed since the MC prediction for jet fragmentation may not be modeled well. The estimate is performed in two steps as described follows.

Preparing the fake lepton factor on Z+jets events To estimate the Z+jets events in the signal region, a fake lepton factor as the lepton fake probability is prepared. Since the fake

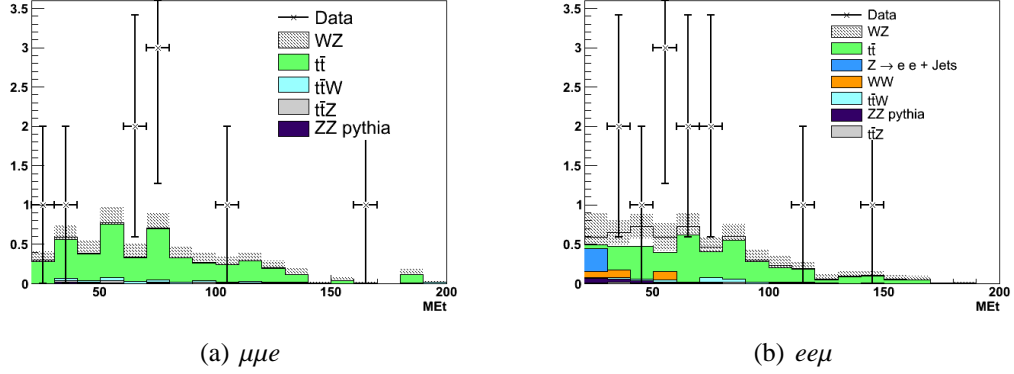


Figure 3.27: E_T^{miss} distribution after all selection cuts with a pair of same charge having a mass closest to the Z mass in $\mu\mu e$ channel (a) and $ee\mu$ channel (b).

lepton factor is expected to depend strongly on the kinematics, the control region which is used to determine the fake lepton factor should be as similar as possible to the signal region. As such the region, the event having a Z boson and an additional lepton candidate but failing the E_T^{miss} selection to explicitly exclude the signal region is chosen.

The additional lepton candidates in those selected events are then categorized into two groups. For muons, if the candidate fails passing the isolation selection, it is identified as a "Bad" muon and if it passes the selection, the candidate is identified as a "Good" muon. For electrons, in addition to the isolation selection, the identification criteria are also used. Likewise for the case of muons, if the electron candidate fails passing isolation selection or loose identification, the candidate is identified as the "Bad" electron and if it passes both the selections, it is categorized as the "Good" electron. All the other selections required on the additional candidate are the same as described in 3.2.2. The "Good" leptons and "Bad" ones for the fake lepton factor determination are corresponding to the regions B and C in Figure 3.28, respectively.

The fake lepton factor is defined as

$$f_{\text{lepton}} = \frac{N_{\text{Good lepton}}}{N_{\text{Bad lepton}}}, \quad (3.12)$$

where $N_{\text{Good lepton}}$ the number of "Good" muons or electrons and $N_{\text{Bad lepton}}$ is the number of "Bad" muons or electrons. Events which have three real leptons contribute to both the numerator and denominator of the fake lepton factor. This contribution is estimated with MC and subtracted. Figure 3.29(a) and 3.29(b) show the number of "Bad" and "Good" electrons as function of p_T , respectively. The distributions for muons are shown in Figure 3.30(a) and 3.30(b).

In addition to the inclusive estimate, the fake lepton factor in bins of Z boson p_T , p_T^Z is prepared for the aTGC limit extraction of the p_T^Z distribution for WZ candidates. The differential fake lepton factor is determined as the same way of the inclusive estimate, except the events is divided by the p_T^Z . Figure 3.31(a) and 3.31(b) show the fake lepton factor as a function of p_T^Z for muons and electrons. The fake lepton factor measured in MC is also shown as a comparison.

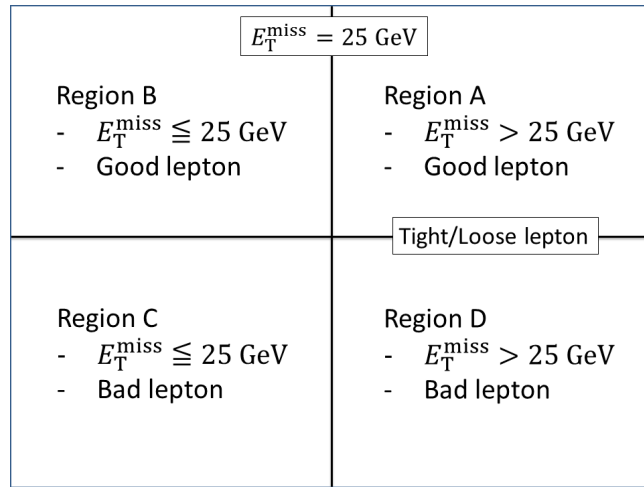


Figure 3.28: Matrix for the data-driven on Z+jets

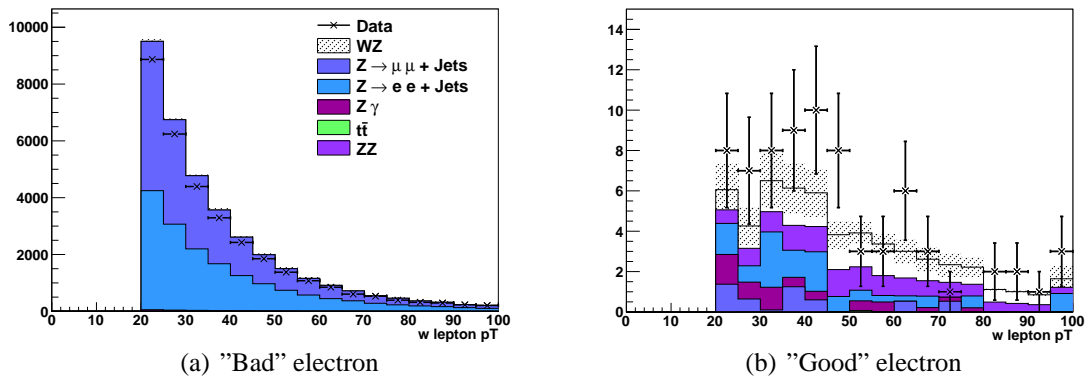


Figure 3.29: p_T of additional electrons in low E_T^{miss} region

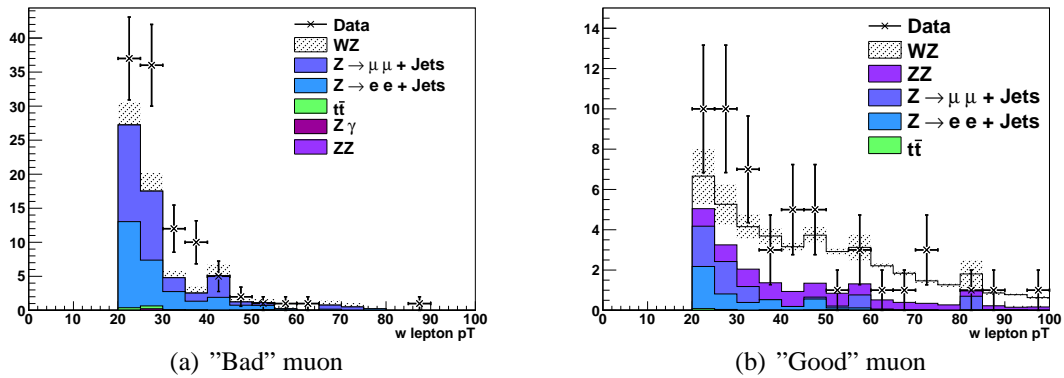


Figure 3.30: p_T of additional muons in low E_T^{miss} region

Due to lack of data statistics in the last two bins of p_T^Z , the fake lepton factor is calculated for the last three bins together.

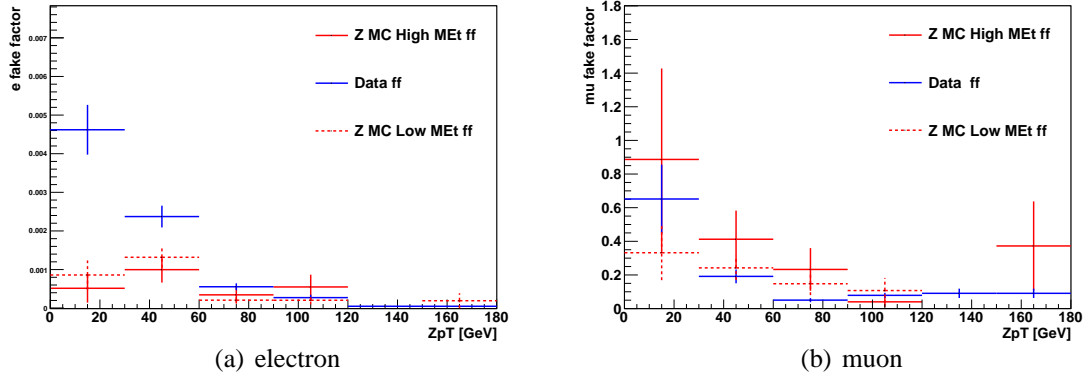


Figure 3.31: Fake lepton factor in bins of p_T^Z

Z+jets events estimation using fake lepton factor To estimate the contribution of Z+jets to signal region corresponding to the region A in Figure 3.28, a control sample of Z+jets events which corresponds to the region D and to which the fake lepton factor applies is identified in data. This sample contains two reconstructed leptons passing all object selections and at least one jet which could be identified as a lepton. The jet in the control region fails passing the isolation selection, which is for muons, and identification and isolation, which are for electrons. The sample is required to pass all event selection criteria including the E_T^{miss} and M_T^W selections to be as close to the signal region as possible. The estimate of Z+jets in the signal region is obtained by scaling each event with the fake lepton factor.

3.4 Systematic Uncertainty

Systematic uncertainties considered are the one related to the trigger, reconstructed objects (muons, electrons, E_T^{miss}), background estimations with data and simulations. The uncertainties for the trigger, the muon (electron) reconstruction efficiency, the electron identification efficiency and the muon (electron) isolation and impact parameter efficiency are evaluated on their scale factors. The summary of all relative acceptance uncertainty from the simulations is shown in Table 3.7.

Uncertainty on the trigger

The trigger efficiency is measured by the Tag-and-Probe method. The concept is explained in Section 2.4.1. The uncertainties on the trigger efficiency consist of the one of the muon trigger and the one of the electron trigger.

- As the uncertainties on scale factors for the single muon trigger, six sources are considered [17]. The variations of scale factors in terms of p_T and the variation of the bin size which is used to derive the scale factors are considered to be uncertainties. Since the tag and probes are produced back-to-back in ϕ , probes tend to be located opposite to high efficiency regions. Possible bias due to the effect was also evaluated. The selection criteria for the tag and probes is also another source. The sensitivity of the scale factors to the MC modeling can be another source. The effect of different pile-up simulation model is also considered. The resulting change of each source in the scale factors is quoted as the systematic uncertainty for each source. The individual systematic uncertainties are considered to be uncorrelated and are added in quadrature to obtain the total systematic uncertainty $\sigma_{\text{mutrigger}}$ on the muon trigger.
- The uncertainties on the electron trigger include the biases due to the selection criteria for the tag and probes, the invariant mass cut and the ΔR requirement between the trigger and reconstructed electrons. The variations seen as a function of η is also considered as systematic sources [18] [66]. The individual systematic uncertainties are considered to be uncorrelated and are added in quadrature to obtain the total systematic uncertainty $\sigma_{\text{electrigger}}$ on the muon trigger.

The final uncertainty on the muon and electron trigger for $W^\pm Z \rightarrow \ell \nu \ell' \ell'$ process is obtained as the difference in signal acceptance by shifting the scale factors by $\pm 1\sigma_{\text{mutrigger}}$ and $\pm 1\sigma_{\text{electrigger}}$, respectively,

Uncertainty on the muons

The uncertainties on reconstructed muons are divided into three types.

- Uncertainty on the muon reconstruction efficiency. As is the case off the trigger efficiency, the reconstruction efficiency is also measured by the Tag-and-Probe method, though the probes are defined as the Inner Detector tracks instead of Combined muons. As the uncertainty estimation, the cuts on the selection for tag and probes are varied [67]. The amount of simulated background is also varied. And the resulting change in the scale factors is quoted as systematic uncertainty. The individual systematic uncertainties are considered to be uncorrelated and are added in quadrature to obtain total systematic uncertainty.
- Uncertainty on the momentum resolution of p_T . The uncertainty of the material budget in the Inner Detector is evaluated by constraining multiple scattering correction in simulations. The uncertainty originated from the alignment accuracy in the Muon Spectrometer is also evaluated [68].
- Uncertainty on the muon isolation and impact parameter efficiency. The isolation and impact parameter efficiency is measured by the Tag-and-Probe method. The uncertainty is estimated by varying the cuts on the selection for tag and probes.

Uncertainty on the electrons

The sources of the systematics on the electron are the reconstruction and identification efficiency, isolation and impact parameter efficiency, and energy scale and resolution.

- Uncertainty on the electron reconstruction and identification efficiency. The efficiency is measured by the Tag-and-Probe method. The dominant systematic uncertainty on the efficiency is the background subtraction from the probe samples [69]. The uncertainty was estimated by varying the background level under the signal, the cuts applied to the tag component and background subtraction method itself.
- Uncertainty on the electron isolation and impact parameter efficiency. The isolation and impact parameter efficiency is measured by the Tag-and-Probe method. The uncertainty is estimated by varying the cuts on the selection for tag and probes.
- Uncertainty on the energy scale and resolution. The imperfect knowledge of the material in front of the electromagnetic calorimeter affects the electron energy measurement. This is the dominant systematic source of the electron energy scale. As other sources, electronic calibration and the cross-talk of the calorimeter, pile-up effect are also considered [69]. The dominant uncertainty for the energy resolution is due to the uncertainty on the sampling term, as the constant term is correctly reproduced by the simulation. The uncertainty is estimated by increasing the sampling term in the simulation.

Uncertainty on the E_T^{miss}

Since the calculation of E_T^{miss} is built from other reconstructed objects, the uncertainties on those objects can be propagated to the E_T^{miss} in a straightforward way. Besides that, the uncertainties from propagating the muon and electron energy scale and resolution uncertainties are included in the muon and electron uncertainties, therefore they are not considered in the E_T^{miss} uncertainty. The remaining sources of the systematic uncertainty come from the jet objects, which are the topocluster energy scale, the jet energy scale and resolution, and the pile-up effect. Each systematic uncertainty is propagated to the E_T^{miss} .

Background estimations with data

$t\bar{t}$ The uncertainties on the $t\bar{t}$ events estimate is split into two terms. One is the original statistical uncertainty coming from MC but multiplied by the correction factor which is estimated in Section 3.3.3. The second one is derived from the uncertainty on the correction factor.

Z+jets The systematic uncertainties on the Data Driven estimate for the Z+jets events consist two components. One is derived from the scale factor which is used when the fake lepton factor to be applied from low E_T^{miss} control region to the high E_T^{miss} signal region. This is estimated from simulation and dijet data. An additional systematic uncertainty comes from the subtraction of non Z+jets samples in the control regions in data. These samples include WZ, ZZ, and $t\bar{t}$ simulations. This is estimated by varying the uncertainty of each sample.

Generator

As the generator uncertainty, the difference between the MC@NLO and POWHEG BOX [70] is taken as the uncertainty.

Parton distribution functions

The uncertainty on the CT10 NLO PDF set is obtained using PDF error sets.

$$\sigma^+ = \sigma^- = \frac{\sqrt{\sum_i^n = 1 [\max(A_i - A_{WZ}, 0)]^2} + \sqrt{\sum_i^n = 1 [\max(A_{WZ} - A_i, 0)]^2}}{2A_{WZ}} \quad (3.13)$$

where A_{WZ} is the acceptance for $W^\pm Z$ signals which is evaluated with the central value of the CT10 NLO, A_i is the acceptance evaluated at a shifted value of CT10 for one sigma at a parameter. The uncertainty between different PDF sets is estimated by comparing CT10 to the central MSTW 2008 NLO PDF set [71]. The uncertainty due to the statistics of the sample is also considered.

QCD scale

The uncertainty of renormalization (μ_r) and factorization (μ_f) scales on A_{WZ} are also evaluated. It is obtained by varying the scale by a factor of 2 and 0.5 in the MC@NLO sample.

Source	$\mu\mu\mu$	$\mu\mu e$	$ee\mu$	eee
μ -reconstruction efficiency	0.8	0.5	0.3	–
μ - p_T scale and resolution	0.1	0.1	<0.1	–
μ -isolation and impact parameter efficiency	0.6	0.4	0.2	–
e-reconstruction efficiency	–	0.8	1.7	2.5
e-identification efficiency	–	1.2	2.3	3.5
e-energy resolution	–	<0.1	0.1	0.1
e-energy scale	–	0.3	0.3	0.5
e-isolation and impact parameter efficiency	–	0.4	1.1	1.5
E_T^{miss} -jet energy scale	0.1	0.1	0.1	0.1
E_T^{miss} -jet energy resolution	0.3	0.4	0.3	0.3
E_T^{miss} -cluster energy scale	0.2	0.6	0.2	0.4
E_T^{miss} -pileup	0.1	0.3	0.1	0.3
μ -trigger efficiency	0.3	0.2	0.1	–
e-trigger efficiency	–	<0.1	<0.1	<0.1
Generator	0.4	0.4	0.4	0.4
PDF	1.2	1.2	1.2	1.2
QCD scale	0.4	0.4	0.4	0.4
Luminosity	1.8	1.8	1.8	1.8

Table 3.7: Summary of all relative acceptance uncertainties (%) for each channel which is used in the cross-section calculation.

3.5 Summary

Kinematic distributions of $W^\pm Z \rightarrow \ell \nu \ell' \ell'$ candidates after all the selections are shown in Figure 3.32 to 3.37. Figure 3.38 shows an example of event display for a WZ candidate.

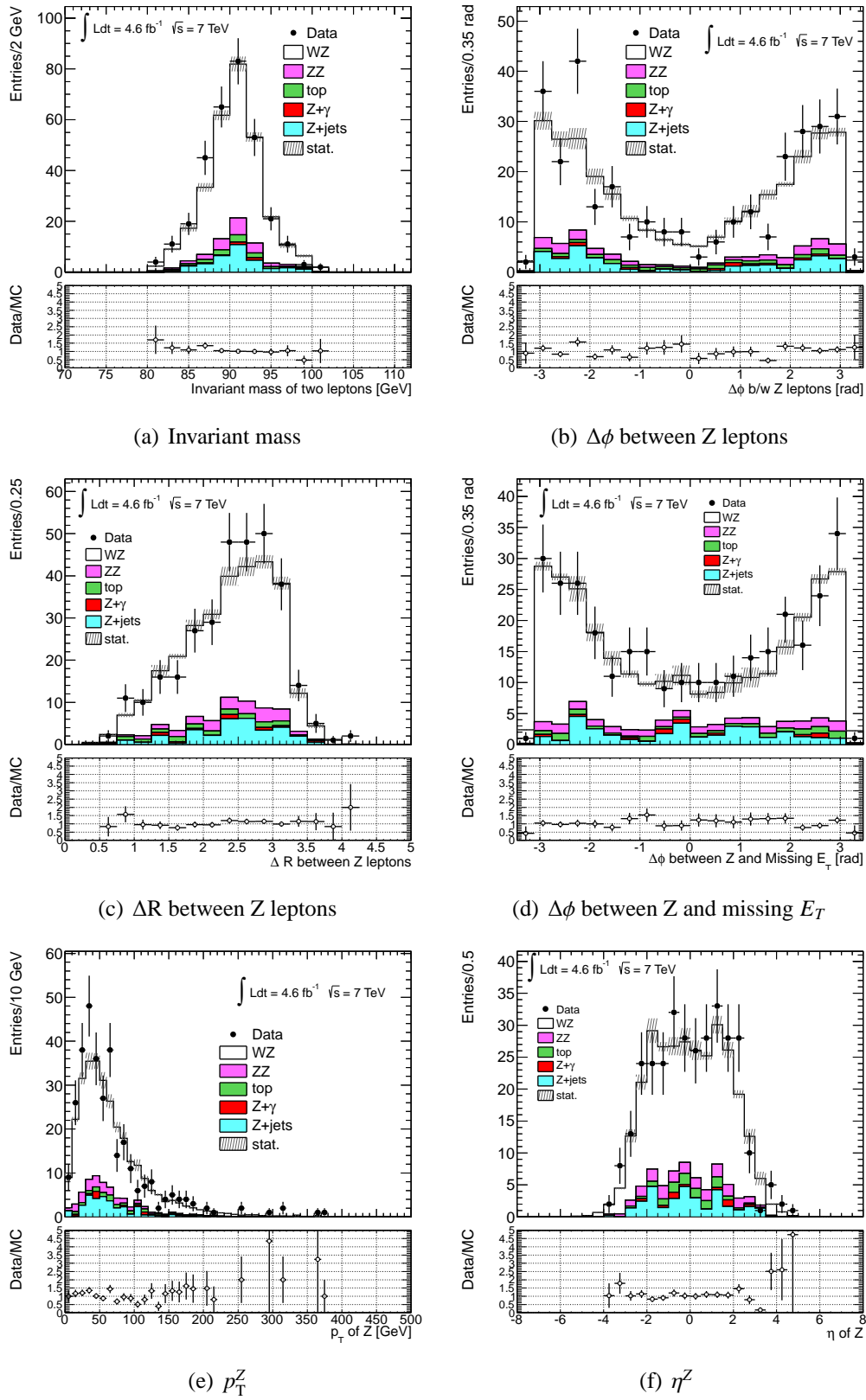


Figure 3.32: Distributions after all selection cuts 1.

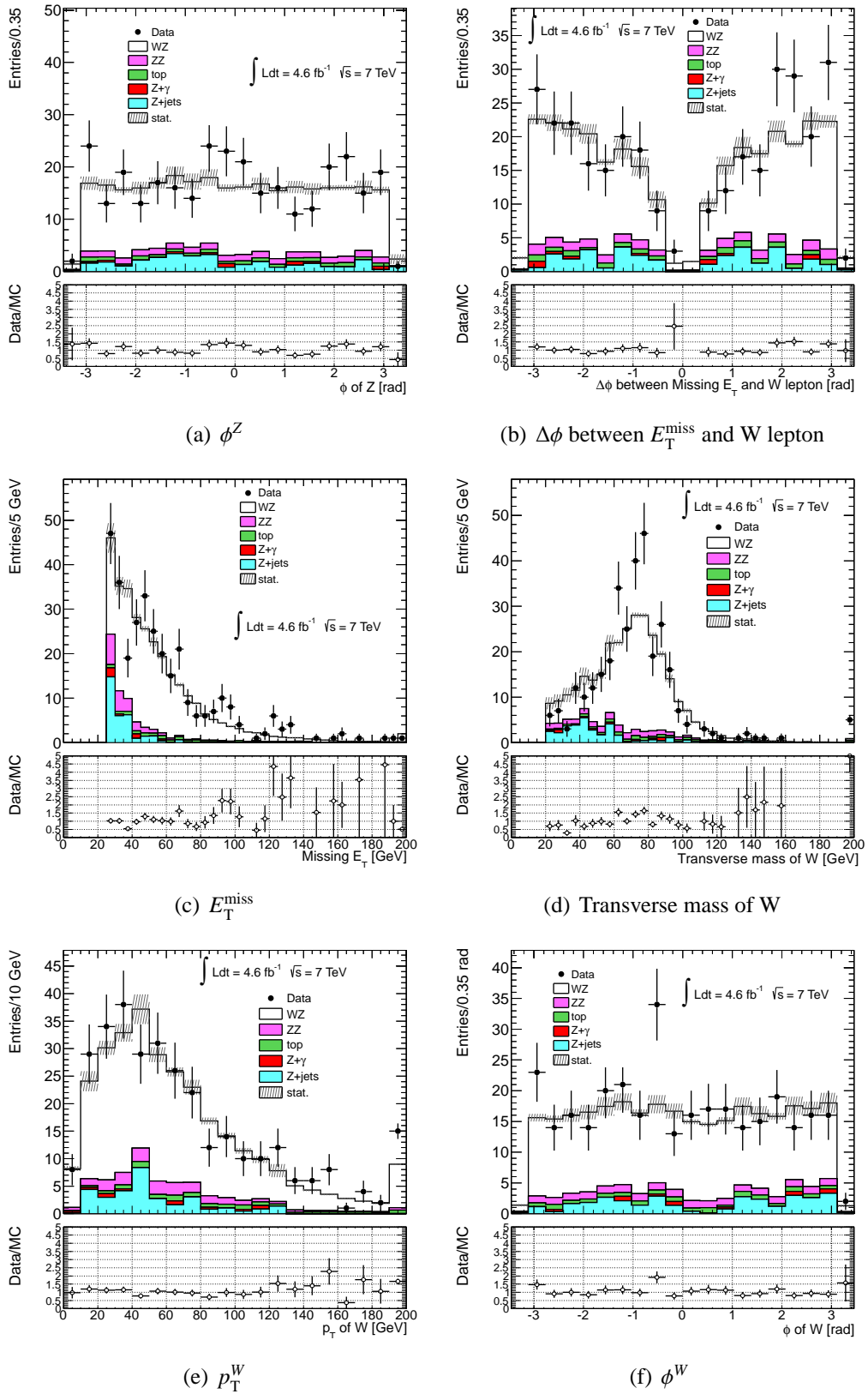
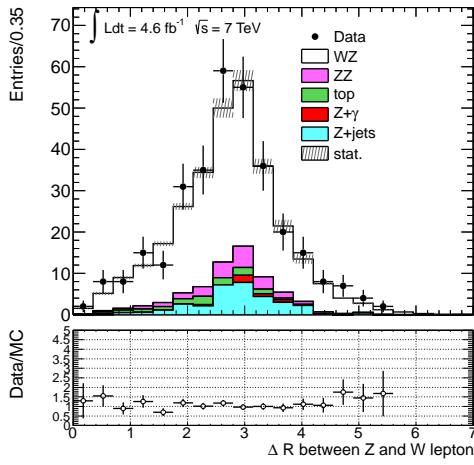
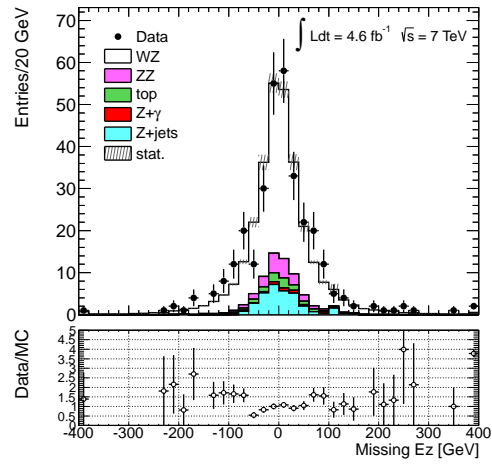
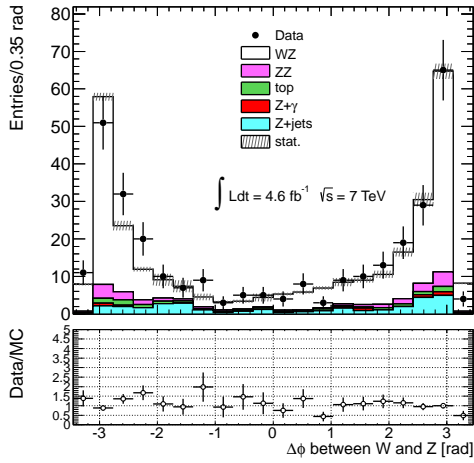
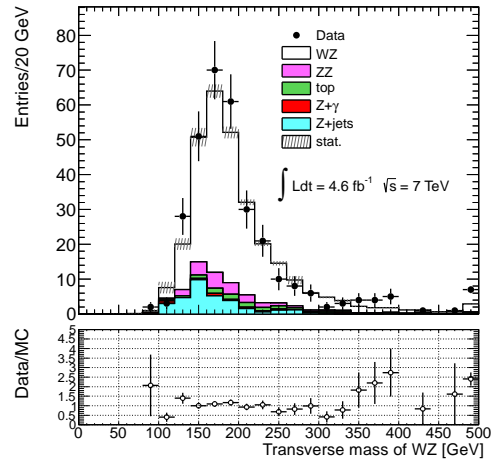
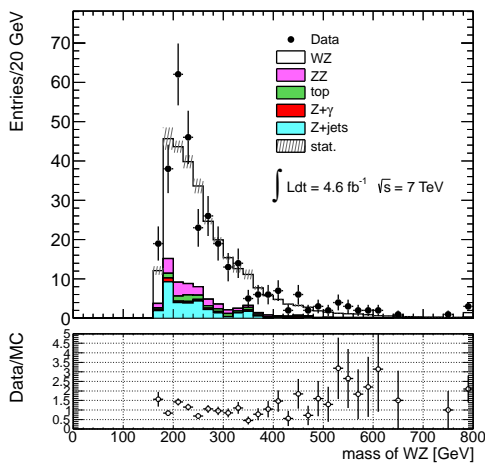


Figure 3.33: Distributions after all selection cuts 2.

(a) ΔR between Z and W lepton(b) estimated missing E_Z (c) $\Delta\phi$ between W and Z(d) M_T^{WZ} 

(e) Invariant mass of WZ

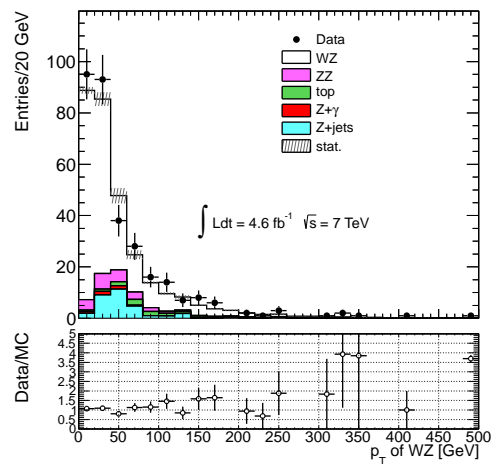
(f) p_T^{WZ}

Figure 3.34: Distributions after all selection cuts 3. The missing E_Z and the invariant mass of WZ are estimated by assuming the W boson mass.

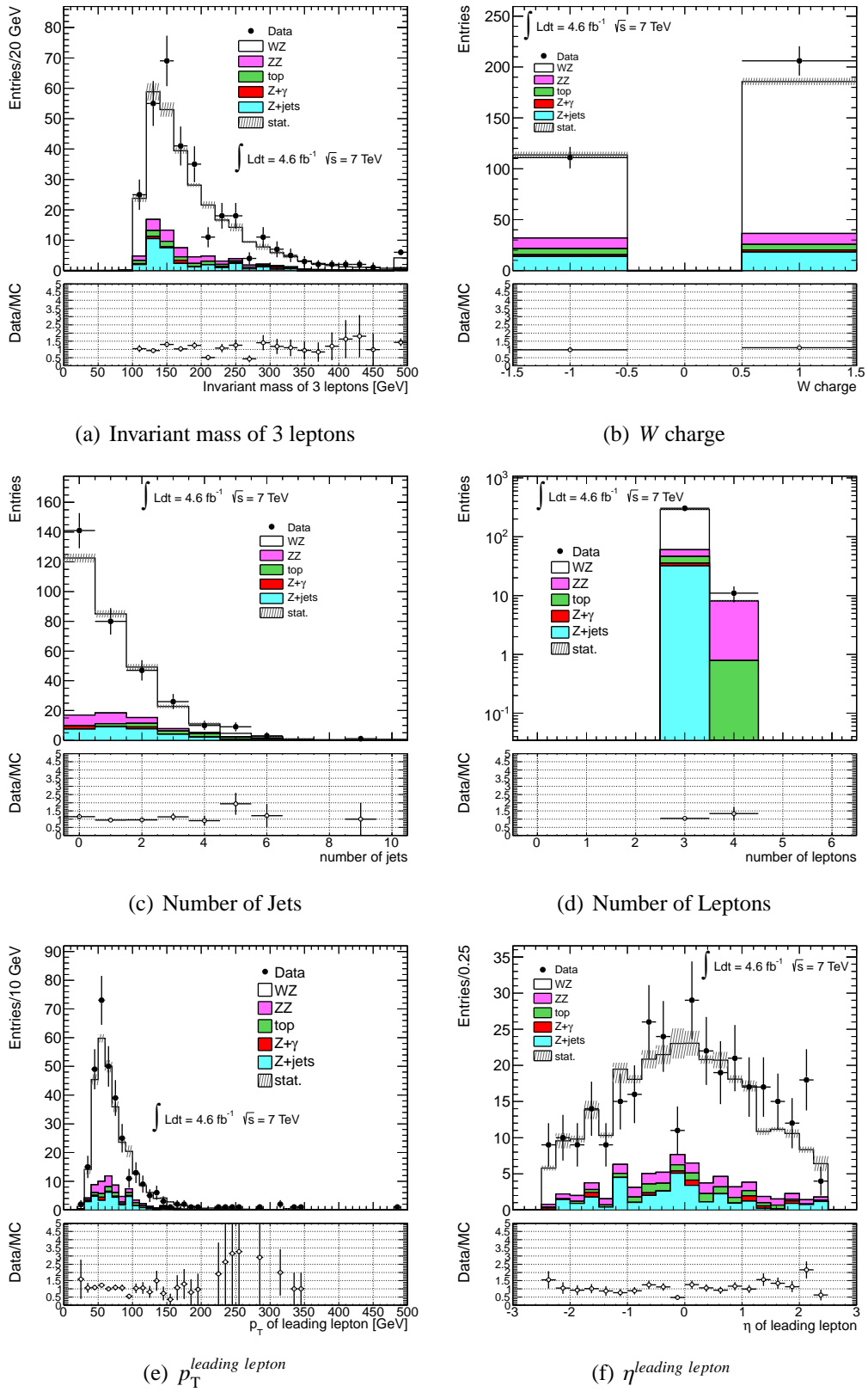


Figure 3.35: Distributions after all selection cuts 4.

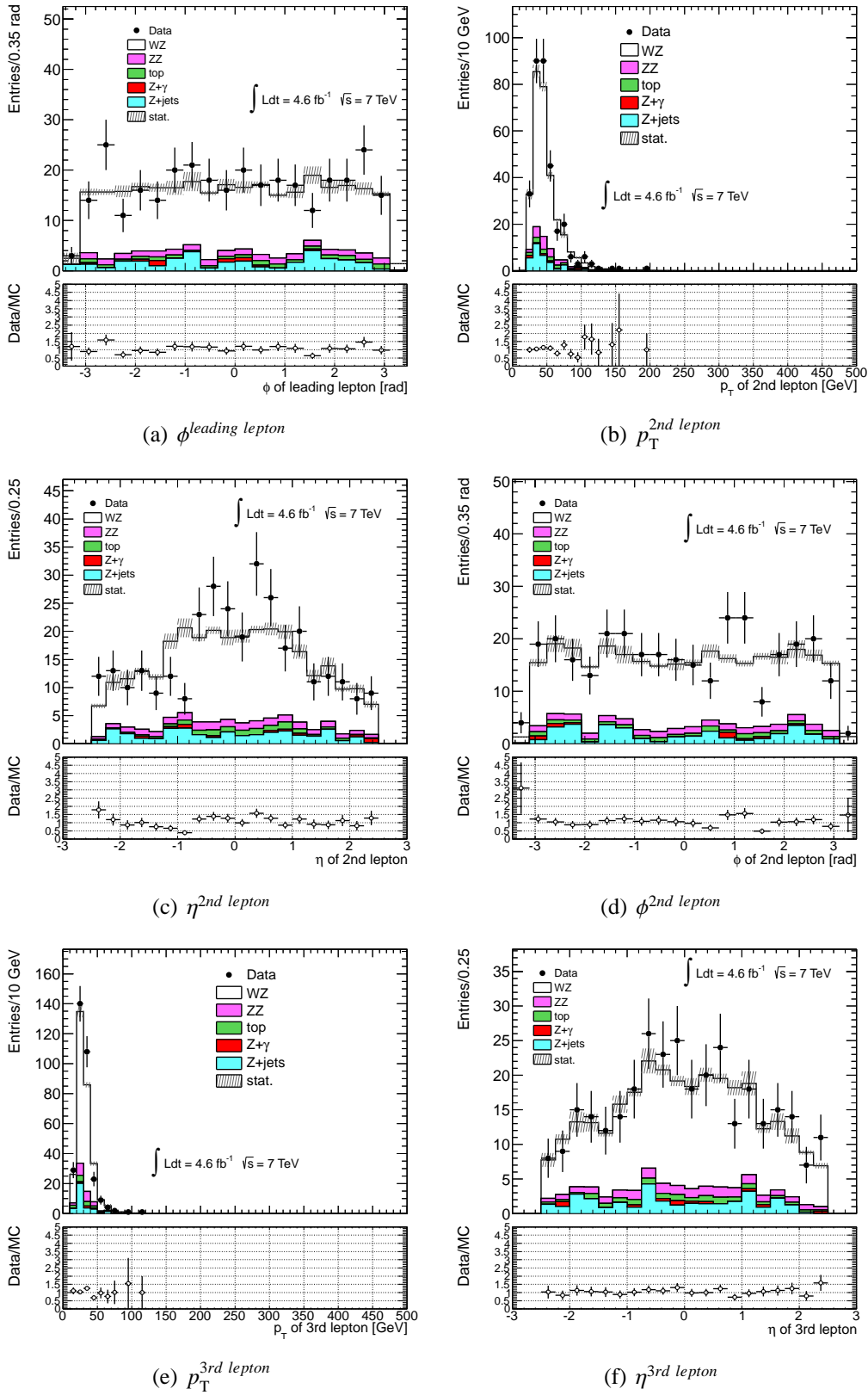
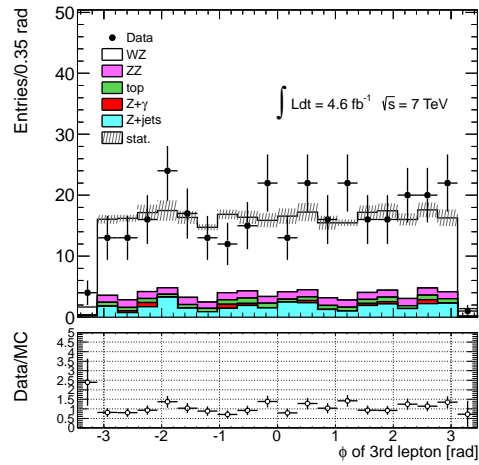


Figure 3.36: Distributions after all selection cuts 5.

(a) $\phi^{\text{third lepton}}$ **Figure 3.37:** Distributions after all selection cuts 6.

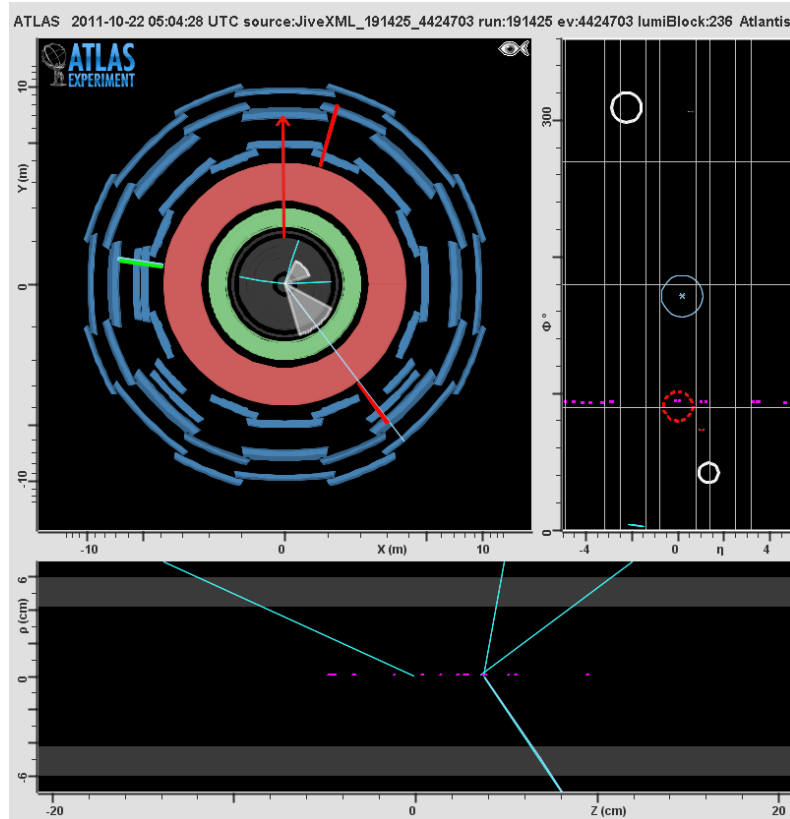


Figure 3.38: An event display of the typical WZ candidate (Run number: 191425, Event: 4424703). The upper left window shows the X-Y plane of the detector. Two bold red lines are muons of the Z candidate, while the bold green line is the electron derived from the W candidate. The red arrow in the figure indicates the direction of E_T^{miss} . The upper right window shows the η - ϕ plane. The bottom window shows the z -R plane around the interaction point. Vertices are shown on the window.

3.5.1 Comparison of Final Numbers of Observed and Expected Events

The number of expected and observed events after applying all selection cuts with statistical and systematic uncertainties are shown in Table 3.8. 317 $W^\pm Z$ candidates are observed in data, 231.2 signal and 68.1 background events are expected. The Z +jets background is estimated using data-driven methods, top quark production is estimated with MC and rescaled to data as described in 3.3.3 and 3.3.4. All the other productions come from MC simulations. For each channel, the fractional systematic uncertainties are calculated by combining different sources in quadrature and then applying to the central value of MC-based estimates. The systematic uncertainties on the Z +jets are estimated from the data-driven method.

Final State	$\mu\mu\mu$	$\mu\mu e$	$e e\mu$	eee	Combined
Observed	108	78	75	56	317
ZZ	$7.9 \pm 0.1 \pm 0.2$	$5.0 \pm 0.1 \pm 0.1$	$4.9 \pm 0.1 \pm 0.2$	$3.2 \pm 0.1 \pm 0.2$	$21.0 \pm 0.1 \pm 0.7$
Z+jets	$9.1 \pm 3.9 \pm 3.9$	$10.2 \pm 2.4 \pm 2.2$	$3.7 \pm 1.7 \pm 1.6$	$8.8 \pm 2.1 \pm 1.9$	$31.9 \pm 5.3 \pm 7.5$
Top	$4.0 \pm 0.5 \pm 1.1$	$3.5 \pm 0.5 \pm 1.0$	$2.9 \pm 0.5 \pm 0.8$	$1.1 \pm 0.3 \pm 0.2$	$11.5 \pm 0.9 \pm 3.4$
Z+ γ	–	$2.3 \pm 0.9 \pm 0.1$	–	$1.4 \pm 0.7 \pm 0.1$	$3.7 \pm 1.1 \pm 0.1$
Bkg (total)	$21.0 \pm 3.9 \pm 4.0$	$21.0 \pm 2.6 \pm 2.4$	$11.5 \pm 1.8 \pm 1.8$	$14.5 \pm 2.2 \pm 1.9$	$68.1 \pm 5.5 \pm 8.2$
Expected signal	$81.7 \pm 0.7 \pm 2.0$	$56.6 \pm 0.6 \pm 1.6$	$54.0 \pm 0.5 \pm 2.1$	$38.9 \pm 0.5 \pm 2.0$	$231.2 \pm 1.1 \pm 7.8$
Expected S/B	3.9	2.7	4.7	2.7	3.4

Table 3.8: Summary of observed events and expected signal and background contributions in the four tri-lepton channels and combined. The first error is statistical while the second is systematic.

Chapter 4

Cross Section Measurement

4.1 Cross Section Extraction

In order to calculate a cross section, a log-likelihood approach is employed. This approach takes into account the Poisson statistics of the samples. For the calculation, the number of observed and expected events as well as the number of estimated background events are needed and those are shown in Table 3.8.

Since the number of expected signal and background events are not perfectly known, nuisance parameters are introduced to express fractional errors. The likelihood function with the nuisance parameters can be defined as

$$L(\sigma, \boldsymbol{\beta}) = \prod_{i=1}^4 \text{Pois}(N_{\text{obs}}^i, N_s^i(\sigma, \boldsymbol{\beta}) + N_b^i(\boldsymbol{\beta})) \cdot e^{-\frac{\boldsymbol{\beta}\boldsymbol{\beta}}{2}}, \quad (4.1)$$

where $\text{Pois}(N_{\text{obs}}^i, N_s^i(\sigma, \boldsymbol{\beta}) + N_b^i(\boldsymbol{\beta}))$ is the Poisson probability of observing N_{obs}^i events in channel i when N_s^i signal and N_b^i background events are expected, σ the total cross-section of $W^\pm Z$ which is to be calculated and $\boldsymbol{\beta}$ is the nuisance parameters assumed to be a standard normal distribution. The N_s^i and N_b^i are affected by the nuisance parameters as

$$\begin{aligned} N_s^i(\sigma, \boldsymbol{\beta}) &= N_s^i(\sigma) \left(1 + \sum_k \beta_k S_k^i\right), \\ N_b^i(\boldsymbol{\beta}) &= N_b^i \left(1 + \sum_k \beta_k B_k^i\right), \end{aligned} \quad (4.2)$$

where S_k^i and B_k^i are the relative uncertainties on the signal and background, respectively, due to the k -th source of uncertainty in channel i as listed in Table 3.7 and Table 3.8. The components of $\boldsymbol{\beta}$ are nominally zero, but allowed to float in the fit with Gaussian constraints imposed. The $N_s^i(\sigma)$ in the total volume can be expressed as

$$N_s^i(\sigma) = \frac{\sigma}{\sigma_{MC}} \times N_{MC}, \quad (4.3)$$

To find the most probable value of the cross section σ , the negative log-likelihood function is minimized simultaneously over the σ and all the nuisance parameters β_k . The final results for the total cross-section measurement in each channel and for the combined measurement are shown in Table 4.1. The uncertainties are estimated by taking the difference between the cross-section at the minimum of the negative log-likelihood function and the cross-section where the negative log-likelihood is 1/2 unit above the minimum in the direction of the fit parameter σ .

Channel	Cross-section [pb]
$\mu\mu\mu$	$18.7^{+2.3}_{-2.2}$ (stat.) ± 1.3 (syst.) ± 0.4 (lumi.)
$\mu\mu e$	$17.7^{+2.9}_{-2.6}$ (stat.) ± 1.2 (syst.) ± 0.4 (lumi.)
$ee\mu$	$20.7^{+3.0}_{-2.7}$ (stat.) ± 1.1 (syst.) ± 0.4 (lumi.)
eee	$18.8^{+3.6}_{-3.2}$ (stat.) ± 1.7 (syst.) ± 0.4 (lumi.)
Combined	$19.0^{+1.4}_{-1.3}$ (stat.) ± 0.9 (syst.) ± 0.4 (lumi.)

Table 4.1: Measured total cross-sections for each channel and combined. The systematic uncertainty includes all sources except luminosity.

Calculation of uncertainties on cross-section

As described above, the likelihood function with nuisance parameters takes into account all uncertainties. The contribution from each source of uncertainties is obtained by changing the acceptance of the signal and background in the likelihood function by one sigma upward and downward separately, and performing the re-minimizing the function. The difference between the nominal cross-section value and the one obtained from the shifted acceptance is taken as the estimate of systematic uncertainty on the cross-section. The systematic uncertainties are summarized in Table 4.2. All uncertainties are added in quadrature to yield the total uncertainty except the one of luminosity. The largest single source of systematic uncertainty is the data-driven estimate of the background contributions, dominated by that for $Z + \text{jets}$ production.

Source	$\mu\mu\mu$	$e\mu\mu$	$ee\mu$	eee	Combined
μ -reconstruction efficiency	+0.9 -0.9	+0.6 -0.6	+0.3 -0.3	—	+0.5 -0.5
μ - p_T scale and resolution	+0.1 -0.1	+0.1 -0.1	+0.0 -0.0	—	+0.1 -0.1
μ -isolation and impact parameter efficiency	+0.7 -0.7	+0.5 -0.5	+0.2 -0.2	—	+0.4 -0.4
e-reconstruction efficiency	—	+0.9 -0.9	+1.9 -1.8	+2.9 -2.7	+1.1 -1.1
e-identification efficiency	—	+1.4 -1.3	+2.5 -2.4	+4.1 -3.8	+1.6 -1.6
e-energy resolution	—	+0.0 -0.0	+0.1 -0.1	+0.1 -0.1	+0.0 -0.0
e-energy scale	—	+0.3 -0.3	+0.3 -0.3	+0.6 -0.6	+0.2 -0.2
e-isolation and impact parameter efficiency	—	+0.3 -0.3	+1.2 -1.2	+1.6 -1.5	+0.6 -0.6
E_T^{miss} -Jet Energy Scale	+0.1 -0.1	+0.1 -0.1	+0.1 -0.1	+0.1 -0.1	+0.1 -0.1
E_T^{miss} -Jet Energy Resolution	+0.2 -0.2	+0.5 -0.5	+0.3 -0.3	+0.3 -0.3	+0.3 -0.3
E_T^{miss} -cluster	+0.2 -0.2	+0.7 -0.7	+0.2 -0.2	+0.4 -0.5	+0.4 -0.4
E_T^{miss} -pileup	+0.1 -0.1	+0.3 -0.3	+0.1 -0.1	+0.3 -0.3	+0.2 -0.2
μ -trigger efficiency	+0.3 -0.3	+0.2 -0.2	+0.1 -0.1	—	+0.2 -0.2
e-trigger efficiency	—	+0.0 -0.0	+0.0 -0.0	+0.0 -0.0	+0.0 -0.0
generator	+0.4 -0.4	+0.4 -0.4	+0.4 -0.4	+0.4 -0.4	+0.4 -0.4
PDF	+1.2 -1.2	+1.2 -1.2	+1.2 -1.2	+1.2 -1.2	+1.2 -1.2
QCD scale	+0.4 -0.4	+0.4 -0.4	+0.4 -0.4	+0.4 -0.4	+0.4 -0.4
signal statistics (MC)	+0.9 -0.9	+1.1 -1.1	+0.9 -0.9	+1.3 -1.3	+0.5 -0.5
background statistics (MC)	+0.1 -0.1	+1.6 -1.6	+0.2 -0.2	+1.7 -1.7	+0.4 -0.4
background statistics (Data Driven)	+4.5 -4.5	+4.3 -4.3	+2.8 -2.8	+5.1 -5.1	+2.3 -2.2
Data Driven method for Z+jets	+4.4 -4.4	+3.9 -3.9	+2.5 -2.5	+4.5 -4.6	+3.1 -3.0
Data Driven method for top	+1.3 -1.3	+1.8 -1.8	+1.3 -1.3	+0.5 -0.5	+1.3 -1.3
Total (no luminosity systematics)	+6.8 -6.8	+6.8 -6.8	+5.5 -5.4	+9.0 -8.9	+4.9 -4.8

Table 4.2: Relative systematic uncertainties (%) on the total cross-section for each channel and the combined result.

Chapter 5

Triple Gauge Coupling Measurement

5.1 Extraction Procedure

To set limits on the aTGC parameters, a frequentist approach is adopted [72] [73]. The procedure is as follows.

1. A likelihood function is constructed.

$$L(N_{\text{obs}}|\alpha, \boldsymbol{\beta}) = \prod_{i=1}^N \text{Pois}(N_{\text{obs}}^i, N_s^i(\alpha, \boldsymbol{\beta}) + N_b^i(\boldsymbol{\beta})) \cdot e^{-\frac{\boldsymbol{\beta}\boldsymbol{\beta}}{2}}, \quad (5.1)$$

$$N_s^i(\alpha, \boldsymbol{\beta}) = N_s^i(\alpha) \left(1 + \sum_{k=1}^n \beta_k S_k^i\right), \quad (5.2)$$

$$N_b^i(\boldsymbol{\beta}) = N_b^i \left(1 + \sum_{k=1}^n \beta_k B_k^i\right), \quad (5.3)$$

where N_{obs} the number of observed events, α the aTGC parameters $\Delta g_1^Z, \Delta \kappa^Z, \Delta \lambda^Z$. N is the number of bins of a histogram to be used for the aTGC extraction and $\boldsymbol{\beta}$ the nuisance parameters which represent the Gaussian constrained systematics. The function is the same of the one for the cross section extraction described in Equation 4.1, if α and N are replaced with the σ and number of channels $N = 4$, respectively.

2. A test statistic $q(\alpha)$ is constructed by taking the ratio of the profile maximum likelihood at a test aTGC parameter value α to the full maximum likelihood.

$$q(\alpha) = \frac{L(N_{\text{obs}}|\alpha, \hat{\boldsymbol{\beta}})}{L(N_{\text{obs}}|\hat{\alpha}, \hat{\boldsymbol{\beta}})}, \quad (5.4)$$

where $\hat{\boldsymbol{\beta}}$ is the estimator of $\boldsymbol{\beta}$ that maximizes the numerator for the fixed test value of α , $\hat{\alpha}$ and $\hat{\boldsymbol{\beta}}$ are the values of α and $\boldsymbol{\beta}$ which maximize the denominator.

3. The observed test statistic $q_{\text{obs}}(\alpha)$ is calculated using the N_{obs} for a value of α . And 10000 of pseudo experiments for the same α of $q_{\text{obs}}(\alpha)$ are generated. At the pseudo experiment,

the β is fluctuated around the mean value of $\hat{\beta}$ of $q_{\text{obs}}(\alpha)$ as Gaussian and the number of pseudo observed events $N_{\text{pe-obs}}$ is generated randomly by assuming a Poisson distribution whose mean is computed from the α and β with the Equation 5.2. Then the test statistic $q_{\text{pe}}(\alpha)$ for each pseudo experiment is calculated and the distribution of $q_{\text{pe}}(\alpha)$ is made. Finally the p-value defined as the fraction of $q_{\text{pe}}(\alpha)$ which are smaller than the $q_{\text{obs}}(\alpha)$ is calculated.

4. By scanning the aTGC parameter α , the step 3 is repeated. The 95% confidence interval (C.I.) of α for the observed data is determined where the p-value is greater than 5%.

The limits are set on each aTGC parameter by setting the other two aTGC parameters to zero.

5.1.1 Reweighting the aTGC Parameters

To determine limits on aTGCs with the procedure described in the previous section, many points of α in a certain range need to be prepared. The MC@NLO version 4.0 [55] used for the estimate of $W^\pm Z$ events can be reweighted to any phase space of aTGC($\Delta g_1^Z, \Delta \kappa^Z, \lambda^Z$). Each event of the MC@NLO has a vector of 10 weights w for the reweighting. The general amplitude for the $W^\pm Z$ process can be written as follows:

$$\mathcal{A} = \mathcal{A}_0 + \Delta g_1^Z \mathcal{A}_{\Delta g_1^Z} + \Delta \kappa^Z \mathcal{A}_{\Delta \kappa^Z} + \lambda^Z \mathcal{A}_{\lambda^Z}, \quad (5.5)$$

with \mathcal{A}_0 the SM result. An event weight (i.e. the cross-section) is therefore:

$$\begin{aligned} w(\Delta g_1^Z, \Delta \kappa^Z, \lambda^Z) &= w_0 + (\Delta g_1^Z)^2 w_1 + (\Delta \kappa^Z)^2 w_2 + (\lambda^Z)^2 w_3 \\ &\quad + 2\Delta g_1^Z w_4 + 2\Delta \kappa^Z w_5 + 2\lambda^Z w_6 \\ &\quad + 2\Delta g_1^Z \Delta \kappa^Z w_7 + 2\Delta g_1^Z \lambda^Z w_8 + 2\Delta \kappa^Z \lambda^Z w_9. \end{aligned} \quad (5.6)$$

Each aTGC parameters is a form of $\alpha_0 / \left(1 + \frac{\hat{s}}{\Lambda^2}\right)^2$ where \hat{s} is the four-momentum squared of the $W^\pm Z$ system and Λ is the cut-off scale as explained in Section 1.1.5. The final expected number of signal events $N_s^i(\Delta g_1^Z, \Delta \kappa^Z, \lambda^Z)$ is obtained by accumulating those weight with the form of

$$\begin{aligned} N_s^i(\Delta g_1^Z, \Delta \kappa^Z, \lambda^Z) &= W_0^i + (\Delta g_1^Z)^2 W_1^i + (\Delta \kappa^Z)^2 W_2^i + (\lambda^Z)^2 W_3^i \\ &\quad + 2\Delta g_1^Z W_4^i + 2\Delta \kappa^Z W_5^i + 2\lambda^Z W_6^i \\ &\quad + 2\Delta g_1^Z \Delta \kappa^Z W_7^i + 2\Delta g_1^Z \lambda^Z W_8^i + 2\Delta \kappa^Z \lambda^Z W_9^i, \end{aligned} \quad (5.7)$$

where W_j^i is the accumulated weight of w_j^i over the events which pass all selections described in Section 3.2.1.

5.2 Observable Selection

As described in Section 1.1.5, the presence of aTGCs modifies the $W^\pm Z$ cross section. The Figure 5.1 shows that the $W^\pm Z$ cross-section has a quadratic dependence on the aTGC. Furthermore, some observables that are sensitive to $\sqrt{\hat{s}}$ are expected to be deviated from the Standard Model more significantly than the cross section alone since those observables include not only the effect on the cross-section but also the one on their distributions. The dependence of the aTGCs on some observables that are sensitive to $\sqrt{\hat{s}}$ can be found in Figure 5.2. Those figures show large deviations from the Standard Model distributions at high mass or momentum.

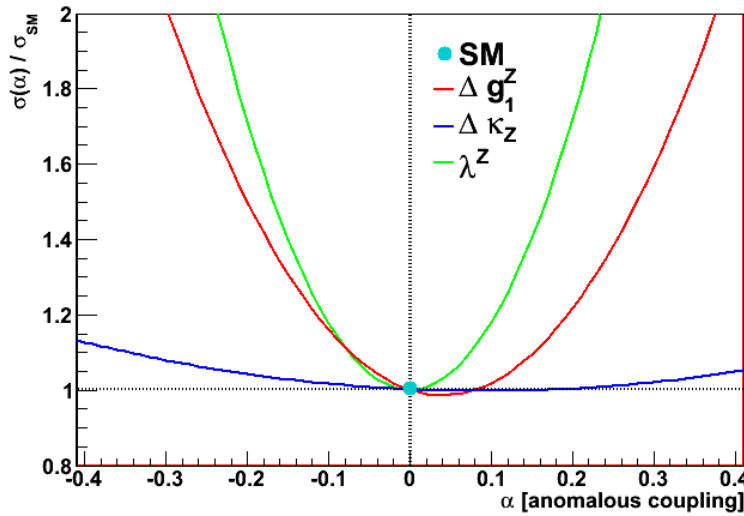
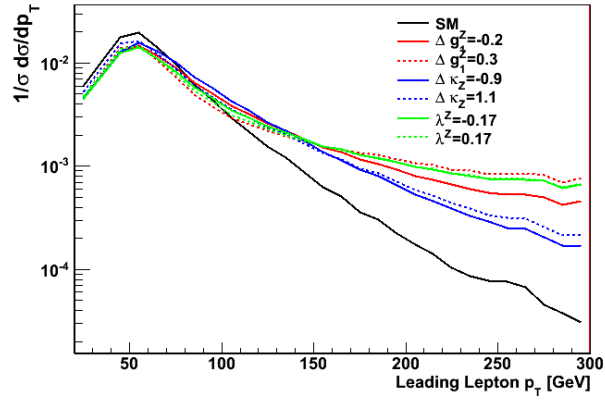
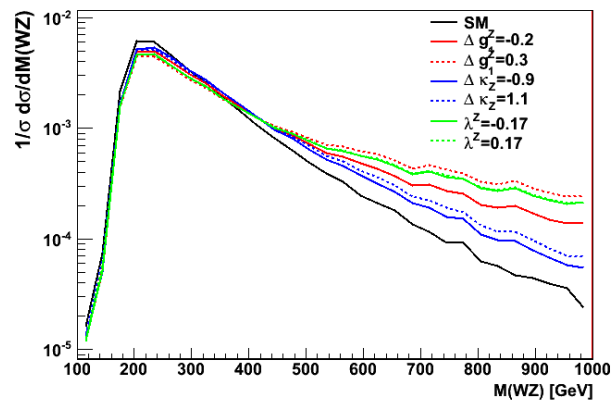
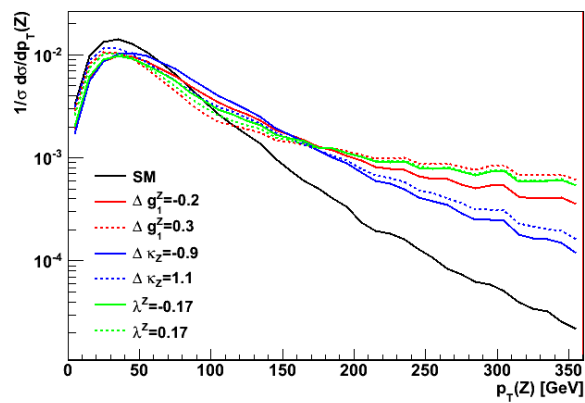


Figure 5.1: The aTGC parameter dependence on the cross section at 7 TeV.

In order to find the most sensitive distribution to the aTGC parameters, a toy study was performed for leading lepton p_T , invariant mass of the three leptons of WZ , m_{WZ} and p_T^Z . For the study each distribution is divided into 4 bins. The binning is selected so that each bin has the same number of expected $W^\pm Z$ events to exclude a potential bias due to different binnings. The optimization of the binning is performed separately and described in Section 5.3. For each aTGC parameter and for each observable, the width of the 95% confidence interval is calculated in 5000 toy experiments. The results show that the measured p_T of Z boson gives the narrowest expected limits for all three aTGC and hence the observable is employed.

(a) leading lepton p_T 

(b) Invariant mass of the W and Z boson

(c) Z boson p_T **Figure 5.2:** The impact of aTGCs on the truth distributions.

5.3 Binning Selection

The ratio of number of expected Standard Model to aTGC events varies as the binning of the distribution for the p_T of Z boson changes. In order to choose a binning for the extraction of aTGC limits, a toy study, which is the same way of the selection of observable, is performed. The study finds the sensitive binnings, which are six bins in p_T^Z of width 30 GeV followed by a wide bin that includes 180-2000 GeV. Figure 5.3 shows the p_T^Z distribution of the selected events together with the SM prediction and non-zero anomalous couplings without form factor for illustration. Table 5.1 and 5.2 show the final number of events and the relative acceptance uncertainties in each bin of the p_T^Z , respectively.

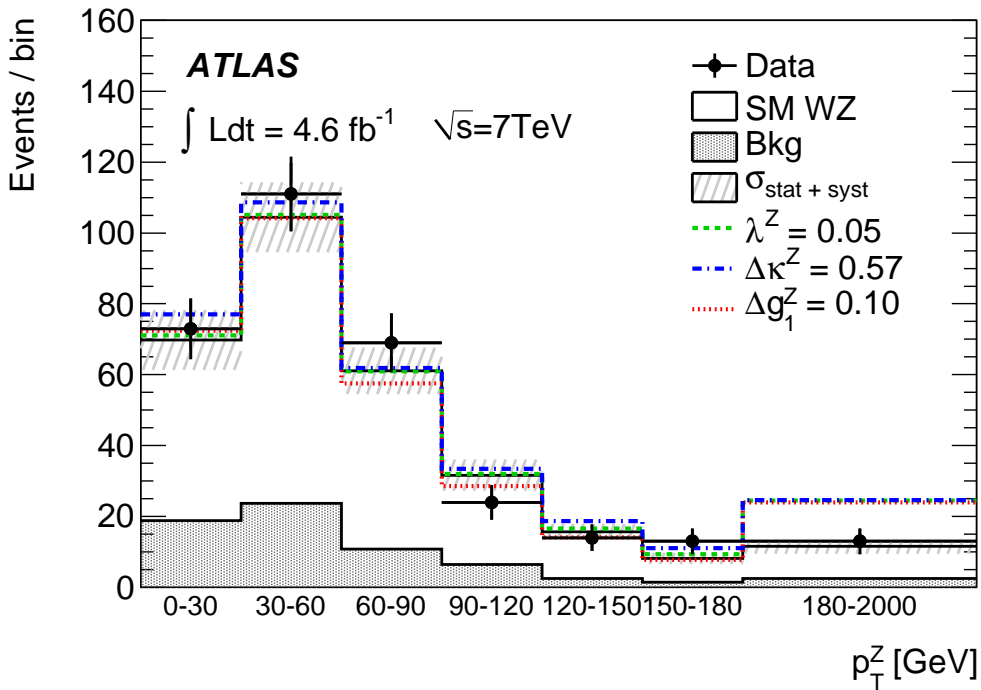


Figure 5.3: The p_T distribution of Z bosons.

$p_T(Z)$ [GeV]	[0,30]	[30,60]	[60,90]	[90,120]	[120,150]	[150,180]	[180,2000]
Observed	73	111	69	24	14	13	13
ZZ	$4.8 \pm 0.1 \pm 0.3$	$7.4 \pm 0.1 \pm 0.5$	$4.3 \pm 0.1 \pm 0.3$	$2.1 \pm 0.1 \pm 0.2$	$1.0 \pm 0.0 \pm 0.1$	$0.6 \pm 0.0 \pm 0.1$	$0.8 \pm 0.0 \pm 0.1$
W/Z+jets	$12.2 \pm 4.0 \pm 2.6$	$11.5 \pm 2.4 \pm 2.1$	$3.3 \pm 1.9 \pm 0.6$	$1.5 \pm 1.0 \pm 0.3$	$0.5 \pm 0.5 \pm 0.2$	$0.4 \pm 0.5 \pm 0.1$	$0.6 \pm 0.6 \pm 0.2$
Top	$1.4 \pm 0.4 \pm 0.5$	$2.9 \pm 0.5 \pm 0.9$	$2.9 \pm 0.4 \pm 0.9$	$1.8 \pm 0.4 \pm 0.5$	$0.9 \pm 0.2 \pm 0.2$	$0.4 \pm 0.1 \pm 0.0$	$1.1 \pm 0.1 \pm 0.1$
W/Z+ γ	$0.4 \pm 0.4 \pm 0.0$	$2.0 \pm 0.8 \pm 0.1$	$0.3 \pm 0.3 \pm 0.0$	$1.0 \pm 0.6 \pm 0.1$	$0.0 \pm 0.0 \pm 0.0$	$0.0 \pm 0.0 \pm 0.0$	$0.0 \pm 0.0 \pm 0.0$
Bkg (total)	$18.7 \pm 4.0 \pm 2.6$	$23.8 \pm 2.6 \pm 2.4$	$10.8 \pm 2.0 \pm 1.2$	$6.4 \pm 1.2 \pm 0.6$	$2.4 \pm 0.5 \pm 0.3$	$1.5 \pm 0.5 \pm 0.2$	$2.5 \pm 0.6 \pm 0.2$
Expected signal	$52.1 \pm 0.6 \pm 3.0$	$76.3 \pm 0.7 \pm 4.8$	$49.4 \pm 0.5 \pm 3.9$	$24.7 \pm 0.4 \pm 2.5$	$12.0 \pm 0.3 \pm 1.0$	$7.2 \pm 0.2 \pm 0.7$	$9.4 \pm 0.2 \pm 0.9$
Expected S/B	2.8	3.2	4.6	3.8	4.9	4.9	3.8

Table 5.1: The number of observed events and expected signal and background contributions in different $p_T(Z)$ ranges used for anomalous Triple Gauge Coupling limit setting. The first error is statistical while the second is systematic.

$p_T(Z)$ [GeV]	[0,30]	[30,60]	[60,90]	[90,120]	[120,150]	[150,180]	[180,2000]
μ -reconstruction efficiency	0.6	0.6	0.6	0.6	0.6	0.6	0.6
μ - p_T scale and resolution	0.1	<0.1	0.1	0.2	0.4	0.2	0.3
μ -isolation and impact parameter efficiency	0.3	0.4	0.5	0.5	0.6	0.6	0.6
e-reconstruction efficiency	1.0	1.0	1.2	1.0	1.1	0.1	1.1
e-identification efficiency	1.4	1.4	1.0	1.4	1.4	0.6	1.3
e-energy resolution	0.1	<0.1	0.3	0.1	0.1	0.5	0.1
e-energy scale	0.2	0.2	0.1	0.4	0.4	0.4	1.1
e-isolation and impact parameter efficiency	0.4	0.6	0.8	0.7	0.7	<0.1	0.7
E_T^{miss} -jet energy scale	0.1	0.1	0.2	<0.1	0.2	0.4	<0.1
E_T^{miss} -jet energy resolution	<0.1	<0.1	0.3	0.4	0.1	0.1	0.6
E_T^{miss} -cluster energy scale	<0.1	0.2	0.4	0.5	0.2	0.1	0.1
E_T^{miss} -pileup	<0.1	0.1	0.4	0.4	0.1	<0.1	0.2
μ -trigger efficiency	0.1	0.2	0.2	0.2	0.2	0.1	0.1
e-trigger efficiency	<0.1	<0.1	<0.1	<0.1	<0.1	<0.1	<0.1
Generator	0.6	3.0	3.9	1.1	1.1	4.3	1.5
PDF	4.3	4.2	4.1	4.0	4.2	4.0	4.2
QCD scale	2.6	2.6	4.8	8.7	6.7	7.3	8.0
Luminosity	1.8	1.8	1.8	1.8	1.8	1.8	1.8

Table 5.2: Summary of all relative acceptance uncertainties (%) in bins of p_T^Z which is used in the calculation of the aTGC limit.

5.4 Result

Table 5.3 shows the observed 95 % C.I. and the expected ones on the aTGC with two different cut-off scales, $\Lambda = 2$ TeV and $\Lambda = \infty$. Comparison for each aTGC parameter with the result of Tevatron is shown in Figure 5.4.

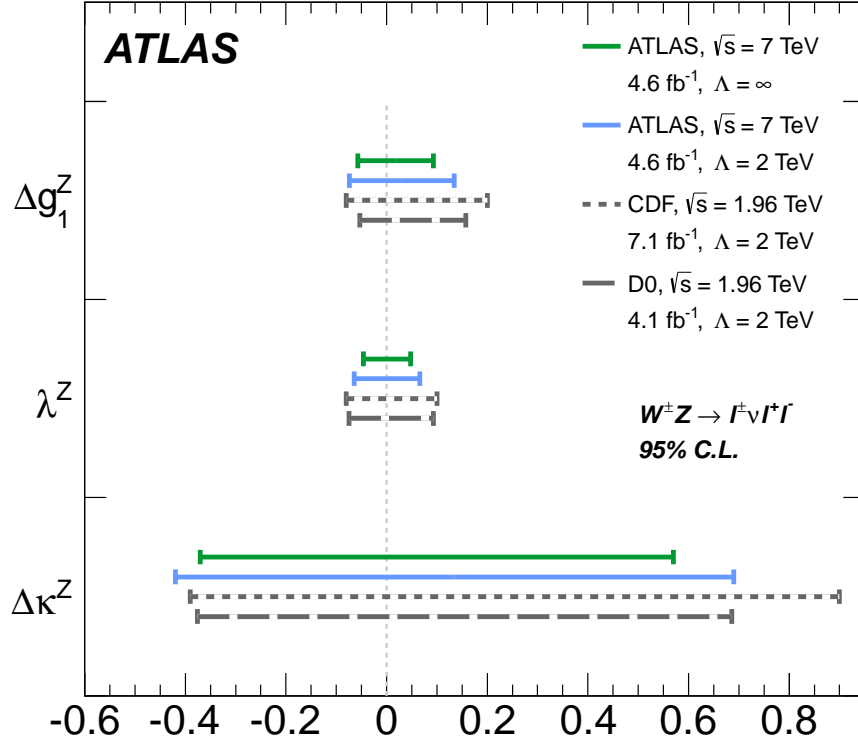


Figure 5.4: Limits of the aTGC parameters.

	Observed 95 % C.I. $\Lambda = 2$ TeV	Observed 95 % C.I. no cut-off, $\Lambda = \infty$	Expected 95 % C.I. no cut-off, $\Lambda = \infty$
Δg_1^Z	[-0.074, 0.133]	[-0.057, 0.093]	[-0.046, 0.080]
$\Delta \kappa^Z$	[-0.42, 0.69]	[-0.37, 0.57]	[-0.33, 0.47]
λ^Z	[-0.064, 0.066]	[-0.046, 0.047]	[-0.041, 0.040]

Table 5.3: Observed and expected 95 % C.I. on the aTGC

Chapter 6

Discussion

6.1 Comparison of the Cross Section Measurement with Other Experiments

Figure 6.1 shows the $W^\pm Z$ cross-section measurement with the CDF [3] and D0 [4] experiment at 1.96 TeV in $p\bar{p}$ collisions, the CMS [24] experiment at 7 TeV in pp collisions as well as the result of this study. The orange band corresponds to prediction of σ_{WZ} in $p\bar{p}$ collisions at 1.96 TeV and pp collisions at 7 TeV. The measurement of the $W^\pm Z$ cross-section in this thesis is the one with the highest center of mass energy at present and also the most accurate result at the energy. This result is consistent with the Standard Model expectation within the uncertainty and confirms that the GWS theory is true even at the high center of mass energy. The total cross-section at 7 TeV measured with the ATLAS is $19.0^{+1.4}_{-1.3}$ (stat.) ± 0.9 (syst.) ± 0.4 (lumi.). The dominant uncertainty is the statistic one. Therefore it is meaningful to see it with more statistics.

6.2 Comparison of the Limit on the anomalous TGC with Other Experiments

As seen in the Figure 5.4, the limits on anomalous TGC are also determined at 7 TeV with 4.6 fb^{-1} data. The expected limits at the ATLAS are slightly more stringent than the observed limits. It is because a slight excess is seen in data relative to the expectation. Moreover, much of the sensitivity to the aTGCs comes in the last bin of Z boson p_T . In the ATLAS, finally 11.5 events are expected and 13 events are observed in the last bin in Figure 5.3. On the other hand, the D0 experiment expected 2 ~ 3 events in the last bin and observed 0. That is why the D0 got stringent limits.

In this study, separate conservation of charge C and parity P on the general Lagrangian is required. As a result, the number of aTGC parameters is reduced to three, and this enables us to compare the result with the one of the Tevatron. There is no simulation currently available which includes aTGC parameters which are not conserve charge C and parity P separately for the WZ final state. However, non C and P conserving aTGC parameters should be also checked

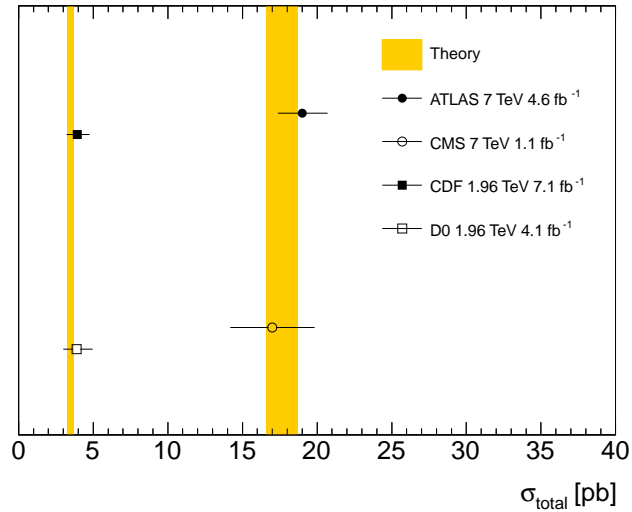


Figure 6.1: Comparison of the cross-section with other experiments results. The cross-section measured by the CDF is $3.9^{+0.6}_{-0.5}(\text{stat.})^{+0.6}_{-0.5}(\text{syst.})$ pb [3] and the one of the D0 is $3.9^{+1.1}_{-0.9}$ pb [4]. The prediction of the cross-section at 1.96 TeV is 3.5 ± 0.21 pb, which is quoted from [3]. The cross-section measured by the CMS is $17.0 \pm 2.4(\text{stat.}) \pm 1.1(\text{syst.}) \pm 1.0(\text{lumi.})$ pb [24]. The prediction of the cross-section at 7 TeV is $17.6^{+1.1}_{-1.0}$ pb.

in the future.

This measurement is a model-independent approach. In the current results at the ATLAS, there are no obvious signatures for physics beyond the Standard Model except the Higgs-like bosons [37]. In such situations, precise measurement of aTGC can provide a possibility to search beyond the Standard Model. The LHC has started the operation with the center of mass energy of 8 TeV since early 2012 and already accumulated 21.7 fb^{-1} data, which is four times more than the one of 2011. It is also expected to run at 13 ~ 14 TeV from 2015 with increased luminosity. Since the aTGC is sensitive to $\sqrt{\hat{s}}$, the four-momentum squared of the WZ system, aTGCs may be observed at these energy and therefore interesting. This study has confirmed that the WZ process is a good probe for the precise test of the SM and the search of the BSM.

Chapter 7

Conclusion

Measurements of the $W^\pm Z$ production in proton-proton collisions at the center of mass energy of 7 TeV have been presented using a data sample with an integrated luminosity of 4.6 fb^{-1} , which was collected with the ATLAS detector at the LHC. The candidate $W^\pm Z$ events were selected in the fully leptonic final states with electrons, muons, and large missing transverse momentum. In total, 317 candidates were observed with a background expectation of 68 ± 10 events. The total cross-section is determined to be

$$\sigma_{WZ}^{tot} = 19.0_{-1.3}^{+1.4}(\text{stat.}) \pm 0.9(\text{syst.}) \pm 0.4(\text{lumi.}) \text{ pb.}$$

This result is consistent with the SM prediction of $17.6_{-1.0}^{+1.1} \text{ pb}$.

Limits on anomalous triple gauge couplings have been derived based on the observed p_T^Z distribution. The 95 % confidence intervals are

$$\Delta g_1^Z \in [-0.057, 0.093]$$

$$\Delta \kappa_Z \in [-0.37, 0.57]$$

$$\lambda_Z \in [-0.046, 0.047]$$

without a form factor.

Both results are consistent with the SM prediction. The uncertainty is dominated by statistics. Therefore further test with data with higher statistics is desirable. A precise measurement of aTGC in WZ process is a good probe for the search of BSM. This study has confirmed them.

Acknowledgments

There are a number of people who supported my research life.

I express my sincere thankfulness to my supervisor, Prof. Hiroshi Sakatmoto. He taught me not only about researches but also about an attitude as an experimental scientist. His generous support helped me many times. It is my great fortune that I have been able to spend my Ph.D course as his student. I deeply appreciate Prof. Susumu Oda. He always offered valuable advises for issues of researches which I faced. I would not finish my study without them. He always engaged in research, and the enthusiasm for research influenced me a lot. I would also like to express my gratitude to Prof. Takashi Matsushita. He taught me the basics of a physics analysis. His sophisticated coding style has affected me.

Ms. Katarina Bendtz is the first Swedish good friend and my English teacher. She often made me laugh with her rich humor. I experienced a different culture through communication with her and it definitely expanded my world. I can look at Japan from a relative viewpoint. Mr. Keiuske Yoshihara is a good playmate and at the same time is a good colleague of researches. Parties which I joined with him were really enjoyable and they were refreshing changes of pace. I would like to express my gratitude to Prof. Toyoko Orimoto. She has kindly invited me to a party that she held. Thanks to that, I had a chance to meet many friends from different nations. Vegetarian foods at the party which she made were really delicious and I really loved them.

I would like to thank to members of the Sakamoto laboratory., Mr. Ikuo Otani, Mr. Yoichi Ninomiya and Mr. Chikuma Kato.

Mr. Yuya Azuma, Mr. Hiroshi Yamaguchi, Mr. Takeshi Domae, Mr. Satoshi Hasegawa, Mr. Takayuki Kanno, Mr. Minoru Hirose, Mr. Yu Suzuki, Dr. Takashi Hayakawa, Mr. Toyonobu Okuyama and Mr. Takuya Nobe made my every day more enjoyable. Spending life at the CERN with them was really fun for me. Many events which I spent with them are now valuable memories.

I would like to thank to spokespersons of the ATLAS Japan, Prof. Tomio Kobayashi and Prof. Katsuo Tokushuku for giving me a valuable opportunity as a member of the ATLAS Japan. I am also deeply grateful to members of the TGC (Thin Gap Chamber) group, Prof. Osamu Sasaki, Prof. Tatsuo Kawamoto, Prof. Masaya Ishino, Prof. Makoto Tomoto, Prof. Hisaya Kurashige, , Prof. Chikara Fukunaga , Prof. Hiroyuki Iwasaki , Prof. Hisaya Kurashige , Prof. Akimiasa Ishikawa , Dr. Masato Aoki , Dr. Yuta Takahashi , Dr. Yasuyuki Okumura , Mr. Jun Wakabayashi, and Mr. Tomoe Kishimoto. I studied the basis of experiment for particle physics through the various activities in this group. I am deeply grateful to WZ analysis group. I gained a precious experience through the study in the group.

I would also like to express my gratitude to ICEPP people, Prof. Sachio Komamiya , Prof. Tomoaki Nakamura , Mr. Ginga Akimoto, , Dr. Takashi Yamanaka, , Dr. Takayuki Yamazaki ,

Mr. Hideyuki Oide, Ms. Xue Bai. Special thanks go to ICEPP secretaries. They supported my research life.

I am profoundly grateful to the many friends and family who have supported me through both good and bad times. Finally, I would like to devote this thesis to my deceased grand father, Daisuke Nagatori.

Bibliography

- [1] J.Drees, *Review of final lep results or a tribute to lep*, 2001. <http://arxiv.org/abs/hep-ex/0110077>.
- [2] *New parton distributions for collider physics*, 2010. http://hep.pa.msu.edu/cteq/public/ct10_2010/figs/.
- [3] CDF Collaboration, *Measurement of the wz cross section and triple gauge couplings in $p\bar{p}$ collisions at $\sqrt{s} = 1.96$ tev* (2012). <http://arxiv.org/abs/1202.6629>.
- [4] D0 Collaboration, *Measurement of the $wz \rightarrow l\nu l$ cross section and limits on anomalous triple gauge couplings in $p\bar{p}$ collisions at $\sqrt{s} = 1.96$ tev*, Physics Letters B (2011). http://www.sprace.org.br/~lietti/artigos/PLB695_67-73_2011.pdf.
- [5] *European organization for nuclear research. the accelerator complex.*, 2008. <http://public.web.cern.ch/public/en/Research/AccelComplex-en.html>.
- [6] *Lhc dipole: Standard cross-section.* http://www.atlas.ch/photos/atlas_photos/selected-photos/lhc/9906025_01_dipmag_diagram.jpg.
- [7] G. Aad et al., *The atlas experiment at the cern large hadron collider - chapter 1: Overview of the atlas detector*, JINST (2008). <http://jinst.sissa.it/LHC/ATLAS/ch01.pdf>.
- [8] G. Aad et al., *The atlas experiment at the cern large hadron collider - chapter 4: Inner detector*, Jinst (2008). <http://jinst.sissa.it/LHC/ATLAS/ch04.pdf>.
- [9] G. Aad et al., *The atlas experiment at the cern large hadron collider - chapter 5: Calorimetry*, Jinst (2008). <http://jinst.sissa.it/LHC/ATLAS/ch05.pdf>.
- [10] *Muon reconstruction and identification performance in atlas: Studies with simulated monte carlo, fig1 the atlas muon spectrometer.* <https://twiki.cern.ch/twiki/pub/AtlasPublic/MuonPerformancePublicPlotsSimulation/ATLAS-muon-rz-tdr-mod2.eps>.
- [11] ATLAS Muon Collaboration, *Atlas muon spectrometer technical design report*, Technical Design Report ATLAS, Geneva, 1997.
- [12] The ATLAS Collaboration, *Muon reconstruction efficiency in reprocessed 2010 lhc proton-proton collision data recorded with the atlas detector* (2011).
- [13] G. Aad et al., *The atlas experiment at the cern large hadron collider - chapter 6: Muon spectrometer*, Jinst (2008). <http://jinst.sissa.it/LHC/ATLAS/ch06.pdf>.
- [14] G. Aad et al., *The atlas experiment at the cern large hadron collider - chapter 2: Magnet system and magnetic field*, JINST (2008). <http://jinst.sissa.it/LHC/ATLAS/ch02.pdf>.
- [15] G. Aad et al., *The atlas experiment at the cern large hadron collider - chapter 8: Magnet system and magnetic field*, Jinst (2008). <http://jinst.sissa.it/LHC/ATLAS/ch08.pdf>.
- [16] *Muon reconstruction and identification performance in atlas: Studies with simulated monte carlo, fig. 10: Schematic illustration of the tag and probe method.* https://twiki.cern.ch/twiki/pub/AtlasPublic/MuonPerformancePublicPlotsSimulation/Insitu_Fig10.eps.

- [17] The ATLAS Collaboration, *Performance of the atlas muon trigger in 2011*, CERN, 2012. <https://atlas.web.cern.ch/Atlas/GROUPS/PHYSICS/CONFNOTES/ATLAS-CONF-2012-099>.
- [18] The ATLAS Collaboration, *Performance of the atlas electron and photon trigger in p-p collisions at $\sqrt{s} = 7$ tev in 2011* (2012).
- [19] *Pile-up dependence of the atlas muon performance*, 2012. <https://atlas.web.cern.ch/Atlas/GROUPS/PHYSICS/MUON/PublicPlots/2011/Dec/ATL-COM-PHYS-2011-1640.pdf>.
- [20] *Electron identification efficiency dependence on pileup*.
- [21] The ATLAS Collaboration, *Performance of missing transverse momentum reconstruction in atlas with 2011 proton-proton collisions at $\sqrt{s} = 7$ TeV* (2012). <https://cds.cern.ch/record/1463915>.
- [22] *The atlas luminosity measurement taskforce*. <http://project-atlas-lucid.web.cern.ch/project-atlas-lucid/taskforce/main.html>.
- [23] T. Cornelissen, M. Elsing, A. Wildauer, N. van Eldik, E. Moyses, W. Liebig, N. Piacquadio, K. Prokofiev, and A. Salzburger, *Updates of the atlas tracking event data model* (2007). <https://cdsweb.cern.ch/record/1038095/files/soft-pub-2007-003.pdf>.
- [24] The CMS Collaboration, *Measurement of the ww , wz and zz cross sections at cms* (2011). <https://cds.cern.ch/record/1370067/files/EWK-11-010-pas.pdf>.
- [25] *Pdg summary table*, 2010. http://pdg.lbl.gov/2010/tables/contents_tables.html.
- [26] *Lhc design report*, CERN. <http://lhc.web.cern.ch/lhc/lhc-designreport.html>.
- [27] The ATLAS Collaboration, *Improved luminosity determination in pp collisions $\sqrt{s} = 7$ tev using the atlas detector at the lhc* (2012). <http://cdsweb.cern.ch/record/1460392/files/ATLAS-CONF-2012-080.pdf>.
- [28] C.N. Yang and R.L. Mills, *Conservation of isotopic spin and isotopic gauge invariance*, Physical Review (1954).
- [29] Steven Weinberg, *A model of leptons*, Physical Review Letters (1967).
- [30] Donald H. Perkins, *Introduction to high energy physics*, Addison wesley, 1987.
- [31] H. Aihara, *Physics of elementary particles*, 2006.
- [32] Y. Nagashima, *The standard model of the elemental particle physics and experimental foundation*, Asakura Publishing Co., Ltd, 1999.
- [33] K. HAGIWARA, R.D. PECCEI, and D. ZEPPENFELD, *Probing the weak boson sector in $e^+e^- \rightarrow w^+w^-$* , Nuclear Physics B282 (1987).
- [34] E. Nuss, *Di-boson production at hadron colliders with general triple gauge boson couplings. analytic expressions of helicity amplitudes and cross-sections*, Z. Phys. C 76 (1997).
- [35] The ATLAS Collaboration, *Measurement of the $w \rightarrow lv$ and $z/\gamma \rightarrow ll$ production cross sections in proton-proton collisions at $\sqrt{s} = 7$ tev with the atlas detector* (2010).
- [36] *Mcfm - monte carlo for femtobarn processes*. <http://mcfm.fnal.gov/>.
- [37] The ATLAS Collaboration, *Observation of a new particle in the search for the standard model higgs boson with the atlas detector at the lhc*, Physics Letters B (2012).
- [38] G. Altarelli, B. Mele, and M. Ruiz-Altaba, *Searching for new heavy vector bosons in \bar{p} colliders*, Phys. C (1989).
- [39] The ATLAS Collaboration, *Search for resonant wz production in the $wz \rightarrow lv\ell'$ channel in $\sqrt{s} = 7$ tev pp collisions with the atlas detector*, Phys. Rev. D (2012).
- [40] G. Aad et al, *Measurement of w^+z production in proton-proton collisions at $\sqrt{s} = 7$ tev with the atlas detector*, The European Physical Journal C (2012).

-
- [41] Lyndon Evans and Philip Bryant (editors), *The cern large hadron collider: Accelerator and experiments*, Jinst (2008). http://jinst.sissa.it/LHC/LHCmachine/2008_JINST_3_S08001.pdf.
- [42] The ATLAS Collaboration, *Alignment of the ATLAS Inner Detector Tracking System with 2010 LHC proton-proton collisions at $\sqrt{s} = 7$ TeV*, Technical Report ATLAS-CONF-2011-012, CERN, Geneva, 2011. <https://atlas.web.cern.ch/Atlas/GROUPS/PHYSICS/CONFNOTES/ATLAS-CONF-2011-012/>.
- [43] The ATLAS Collaboration, *Performance of the electron and photon trigger in p-p collisions at $\sqrt{s} = 900$ gev*, CERN, 2010. <https://atlas.web.cern.ch/Atlas/GROUPS/PHYSICS/CONFNOTES/ATLAS-CONF-2010-022/ATLAS-CONF-2010-022.pdf>.
- [44] The ATLAS Collaboration, *Performance of primary vertex reconstruction in proton-proton collisions at $\sqrt{s} = 7$ TeV in the ATLAS experiment*, Technical Report ATLAS-CONF-2010-069, CERN, Geneva, 2010. <https://atlas.web.cern.ch/Atlas/GROUPS/PHYSICS/CONFNOTES/ATLAS-CONF-2010-069/>.
- [45] *A muon identification and combined reconstruction procedure for the atlas detector at the lhc using the (muonboy, staco, mutag) reconstruction packages*, 2007.
- [46] Eric Lancon, *Muonboy status a guided tour*. <http://esmane.physics.lsa.umich.edu/wl/atlas/meetings/2005/rome/20050610-umwlap002-16-lancon/real/f001.htm>.
- [47] Bernardo RESENDE VAZ DE MELO XAVIER, *Muon identification algorithms in atlas*, 2009. <https://cdsweb.cern.ch/record/1209632/files/ATL-PHYS-PROC-2009-113.pdf>.
- [48] The ATLAS Collaboration, *Expected electron performance in the ATLAS experiment*, Technical Report ATLAS-PHYS-PUB-2011-006, CERN, Geneva, 2011. <https://atlas.web.cern.ch/Atlas/GROUPS/PHYSICS/PUBNOTES/ATL-PHYS-PUB-2011-006/>.
- [49] The ATLAS Collaboration, *Reconstruction and Calibration of Missing Transverse Energy and Performance in Z and W events in ATLAS Proton-Proton Collisions at $\sqrt{s} = 7$ TeV in the ATLAS experiment*, Technical Report ATLAS-CONF-2011-080, CERN, Geneva, 2011. <https://atlas.web.cern.ch/Atlas/GROUPS/PHYSICS/CONFNOTES/ATLAS-CONF-2011-080/>.
- [50] The ATLAS Collaboration, *Jet energy scale and its systematic uncertainty in proton-proton collisions at $\sqrt{s} = 7$ TeV with atlas 2010 data* (2011).
- [51] *The atlas beam conditions monitor*, JINST (2008). http://iopscience.iop.org/1748-0221/3/02/P02004/pdf/1748-0221_3_02_P02004.pdf.
- [52] T. Golling, H. S. Hayward, P. U. E. Onyisi, H. J. Stelzer, and P. Waller, *The atlas data quality defect database system*, The European Physical Journal C (2012). <http://link.springer.com/article/10.1140/epjc%2Fepjc%2Fs10052-012-1960-y>.
- [53] *Luminosity versus day - total integrated luminosity in 2011*. <https://twiki.cern.ch/twiki/bin/view/AtlasPublic/LuminosityPublicResults>.
- [54] S. Agostinelli et al., *Geant4-a simulation toolkit* (2003). <http://www.sciencedirect.com/science/article/pii/S0168900203013688>.
- [55] Stefano Frixione and Bryan R. Webber, *Matching NLO QCD computations and parton shower simulations*, JHEP **06** (2002), 029, available at [hep-ph/0204244](http://arxiv.org/abs/hep-ph/0204244).
- [56] *First tuning of herwig/jimmy to atlas data*. http://hepweb03.phys.sinica.edu.tw/eelog/Atlas_aTGC/Docu_ATLAS_MC/ATL-COM-PHYS-2010-858.pdf.
- [57] M.L. Mangano, M. Moretti, F. Piccinini, R. Pittau, and A. Polosa, *Alpgen, a generator for hard multiparton processes in hadronic collisions*, JHEP **0307:001** (2003). <http://arxiv.org/abs/hep-ph/0206293>.
- [58] S.P. Baranov and M. Smizanska, Phys. Rev. D **62** 014012 (2000).
- [59] G. Corcella et al., J. High Energy Phys. **0101**, 010 (2001).

- [60] Torbjorn Sjostrand, Patrik Eden, Christer Friberg, Leif Lonnblad, Gabriela Miu, Stephen Mrenna, and Emanuel Norrbin, *High-energy-physics event generation with pythia 6.1*, Comput.Phys.Commun.135:238-259,2001 (2000).
- [61] Johan Alwall, Pavel Demin, Simon de Visscher, Rikkert Frederix, Michel Herquet, Fabio Maltoni, Tilman Plehn, David L. Rainwater, and Tim Stelzer, *Madgraph/madevent v4: The new web generation*, High Energy Physics (2007).
- [62] *Sherpa*, 2012. <http://sherpa.hepforge.org/doc/SHERPA-MC-2.0.beta.html>.
- [63] P. Golonka and Z. Was, Eur. Phys. J. C 45, 97 (2006).
- [64] S. Jadach, Z. Was, R. Decker, and J. Kuhn, Comput. Phys. Commun. 76, 361 (1993).
- [65] The ATLAS collaboration, *Expected electron performance in the atlas experiment*, ATLAS NOTE (2011). <http://cdsweb.cern.ch/record/1345327/files/ATL-PHYS-PUB-2011-006.pdf>.
- [66] The ATLAS Collaboration, *Performance of the electron and photon trigger in p-p collisions at $\sqrt{s} = 7$ TeV with the atlas detector at the lhc* (2011).
- [67] The ATLAS Collaboration, *Determination of the muon reconstruction efficiency in atlas at the z resonance in proton-proton collisions at $\sqrt{s} = 7$ TeV* (2011). <https://atlas.web.cern.ch/Atlas/GROUPS/PHYSICS/CONFNOTES/ATLAS-CONF-2011-008/>.
- [68] The ATLAS Collaboration, *Atlas muon momentum resolution in the first pass reconstruction of the 2010 p-p collision data at $\sqrt{s} = 7$ TeV* (2011).
- [69] The ATLAS Collaboration, *Electron performance measurements with the atlas detector using the 2010 lhc proton-proton collision data*, Eur. Phys. J. C. (2012).
- [70] T.Melia, P.Nason, R.Rontsch, and G.Zanderghi, *ww, wz and zz production in the powhegbox*. arXiv: hep-ph/1107.5051.
- [71] A.D. Martin, W.J. Stirling, R.S. Thorne, and G. Watt, *Parton distributions for the lhc*, Eur.Phys.J.C63:189-285,2009 (2009). <http://arxiv.org/abs/0901.0002>.
- [72] G. Cowan, K. Cranmer, E. Gross, and O. Vitells, *Asymptotic formulae for likelihood-based tests of new physics* (2011).
- [73] Masahiro Morii and Michael Kagan, *Setting frequentist limits on anomalous tgcs*, 2012.